INELASTIC LIGHT SCATTERING SIGNATURES OF MAGNETIC ORDERING AND TOPOLOGICAL PROPERTIES IN STRONGLY-CORRELATED ELECTRON SYSTEMS

by

Michael E. Valentine

A dissertation submitted to The Johns Hopkins University in conformity with the requirements for the degree of Doctor of Philosophy.

Baltimore, Maryland

October, 2017

Abstract

We investigate strongly-correlated electron systems where magnetically frustrated and Kondo insulating states show significant sensitivity to disorder and defects. Inelastic light scattering provides an effective tool for probing magnetic and electronic structures of novel states that arise from correlations through their excitation spectra along with characterizing weak distortions and disorder within crystal lattices. We explore triangular-lattice Heisenberg antiferromagnets where ground-state properties are altered from an isotropic triangular-lattice model by weak disorder present in the compounds. In the anisotropic triangular-lattice Heisenberg antiferromagnet $SrCr_2O_4$, a coupling of the lattice to magnetic degrees of freedom is observed through a redistribution of phonon intensities that onsets with the formation of peaks within the magnetic spectrum. The triangular-lattice compound $NiGa_2S_4$ with competing interactions shows spin freezing where theoretical modeling suggests a magnetically ordered ground state. We demonstrate evidence for structural disorder within this compound that would modify the Heisenberg Hamiltonian through the loss of superexchange pathways and a breaking of crystal inversion symmetry. Heavy fermion systems combine localized magnetism with itinerant electron bands that can drive Kondo insulating behavior in certain materials. Renewed interest in Kondo insulator SmB_6 has arisen as a result of the proposal of a strongly-correlated topological insulating state in this material which is dependent on the formation of a hybridization gap at low temperatures. Inelastic scattering shows a 10 meV symmetry forbidden mode appearing in the spectrum in samples known to have off-stoichiometries assigned to scattering from acoustic modes away from the Brillouin zone center that results from crystal defects. The intensity of this band is used as a measure of Sm vacancies to identify their effect on the low temperature electronic properties of the system. A suppression of the bulk hybridization gap is found in samples with as little as 1% Sm vacancies demonstrating the sensitivity of the topological insulating state to weak structural disorder.

Primary Reader: Natalia Drichko

Secondary Reader: Collin Broholm

Acknowledgments

Though a single author is listed at the top of this thesis, it would be disingenuous to present this without acknowledging the efforts of so many others that made it possible. Had I not had the contributions and support from them, I certainly would not have been able to make it this far.

Natalia Drichko has seen me through this whole process from a rather raw recruit, new to the field of condensed matter systems, to a contributing physicist. She no doubt had her work cut out for her in this task. It has truly been invaluable to have an unwavering advocate over the years that I could unambiguously count on to provide selfless advice, even at times at her own expense. She accurately knew how to prod me along when things got tough and always sought to make herself available to the problems I faced. Her active engagement in my projects has lead to some great research, and without her guidance and passion for physics its hard to imagine how the past six years could have turned out.

It has been a pleasure working with Collin Broholm who I think embodies what a physicist should strive to be as both a great researcher and a dedicated educator.

Over the years I have benefited from many conversations with him that have opened up new perspectives on my work. Collaborating with Wes Fuhrman has elevated me as a physicist and broadened the scope of the projects we have worked on. Add to that he is probably the friendliest guy I have ever met. Having Martin Mourigal to work with when I was starting out was a true benefit as he helped to bring me up to speed in the field. I have been fortunate to have had great coworkers in this time, Nick Laurita, Chris Morris, LiDong Pan, J.T. Mlack, Nik Hartman, Kemp Plumb, Nora Hassan, Guy Marcus, Shan Wu, Jonas Kindervater, among many others. These guys made long hours in the basement, at times, enjoyable. Seyed Koohpayeh, Adam Phelan, and Tyrel McQueen always had a catalogue of new and exciting materials to study; few spectroscopists are so fortunate to work with crystal growers as talented as these guys.

A Ph.D. has its lows, but what kept me sane through it all was a number of great friends that let me forget about life on Zero. Friday happy hours, camping trips, intramurals, and traveling with these guys really made the past six years fun.

Most importantly I have spent the last 28 years with an exceptionally supportive family, in a special Valentine kind of way. I can always count on Allison, Lindsay, and Nathan to help keep things grounded, and they have been awesome siblings over the years. My mom first inspired my love of science and learning. She was unrelenting in support and dedication to my education and always made certain to see I was keeping myself active in my school work. It is truly regretable that she is not around to see

the culmination of her hard work and devotion. My dad was given the impossible task of raising four kids when she died. I cannot grasp the magnitude of this challenge he faced but can only say that exceptionally falls short of the degree to which he met this undertaking. He showed the same drive in seeing that all of my siblings and I never settled in our work and has guided me through so many challenges I have faced in life.

Dedication

This thesis is dedicated to Mom and Dad.

Contents

List of Tables

List of Figures

Chapter 1

Introduction

1.1 Electronic correlations

Much of the work in solid state physics in the twentieth century sought to model the behavior of condensed matter systems by ignoring the effects of electron-electron interactions to simplify the problem, instead treating electrons collectively under a broad crystal potential. Electronic band theory evolved out of this approach to successfully model the insulating, semiconducting, and metallic properties of a wide range of materials due to these behaviors arising primarily from quantum-mechanical limitations on the electronic wavefunctions from the crystal potential. This thesis explores two realms where this simplified band theory approach breaks down due to strong electron-electron interactions, frustrated magnetism and Kondo insulators, and details the sensitivity of strongly-correlated states on crystal structures.

A central characteristic of the materials studied is an otherwise metallic band structure, where the Fermi energy lies within a band, that is altered by a Coulombic repulsion of electrons. Materials with a partially filled orbital under a simplified band theory model would be expected to have itinerant electrons and conductivity. We can consider a lattice of ions with two electronic states per site and has one electron per site. In the absence of interactions between electrons, such a material would be conductive. If the double occupancy energy, known as the Hubbard U, that results from an electrostatic repulsion of electrons is sufficiently large by comparison to the kinetic energy of the electrons, conduction will be suppressed and the electrons will remain localized at individual ionic sites. A material displaying this behavior is called a Mott insulator.

As mentioned, these localized electrons result in orbitals that are partially filled, and thus there will be a magnetic moment that results from the spins of the unpaired electrons. This gives us the basis for studies of the collective magnetic behavior that results from a lattice of interacting localized magnetic moments. At low temperatures such materials will seek to minimize their the energy of the interaction between moments which will typically lead to ordering. Depending on the manner in which interaction energies are effected by other lattice sites and their geometry, under certain conditions no orientation of the moments will simultaneously minimize all interactions which leads to novel magnetic behavior. In Chapters 3 and 4

Another case where strong electron correlations modify a simple band theory model occurs in heavy fermion systems where, as with Mott insulators, on site Coulomb repulsion of electrons leads to localized moments. In a system with both d and f electrons near the Fermi energy, the f electrons will typically have a sufficiently large Hubbard double occupancy energy U to form localized magnetic states while the d electrons remain itinerant. At high temperatures the d electrons will have sufficient kinetic energy to traverse the crystal lattice, but as the temperature is lowered magnetic scattering between the itinerant d electrons and the localized f electrons suppresses conduction and leads to insulating behavior via the Kondo effect.

1.2 Localized magnetic behavior

1.2.1 Heisenberg model

As unpaired electrons form localized magnetic moments on a crystal lattice, the interaction of these dipoles can lead to novel behavior. The Heisenberg model represents a simplified model of magnetic dipoles on a crystal lattice where the energy associated with the orientations moments on sites that interact is taken as $J\hat{\mathbf{S}}_1 \cdot \hat{\mathbf{S}}_2$ with some exchange interaction constant J depending on the spatial relationship of the two sites. Chapter 3 on $SrCr_2O_4$ and Chapter 4 on $NiGa_2S_4$ detail work on these magnetic materials that are best described using this framework. The magnetic state within $SrCr_2O_4$[1,3] and its sister compound [6,7] are well modeled by only considering interactions between nearest neighbor spins on a nearly triangular lattice.

In $NiGa_2S_4$, we see the competing interactions between nearest neighbor and third nearest neighbor spins as integral in suppressing low temperature magnetic ordering.

There are two chief groups of behaviors exhibited by localized magnetic moments in materials that can be distinguished by their microscopic and macroscopic properties. A ferromagnetically ordered state comes about when the lowest energy state involves spins that are aligned parallel to each other leading to a macroscopic magnetic moment. In other systems it is energetically favorable for neighboring local moments to align antiparallel, known as antiferromagnetism, where in the ordered state macroscopic magnetism will be canceled out by the averaging of oppositely aligned spins.

An understanding of the mechanism for the interaction between spins is necessary for an accurate modeling of the behavior in magnetic systems. The primary means for this interaction, referred to as the exchange interaction, results from a Coulombic repulsion of neighboring magnetic states rather than a direct magnetic dipole-dipole interaction. The energy associated with a two magnetic dipoles spaced a distance $\mathbf{r}$ apart is given by

$$E = \frac{\mu_0}{4\pi r^3}\left[\boldsymbol{\mu}_1 \cdot \boldsymbol{\mu}_2 - 3(\boldsymbol{\mu}_1 \cdot \hat{\mathbf{r}})(\boldsymbol{\mu}_2 \cdot \hat{\mathbf{r}})\right] \tag{1.1}$$

where $\boldsymbol{\mu}_1$ and $\boldsymbol{\mu}_2$ are the two dipole moments. For moments situated on neighboring lattice sites this would give an interaction energy on the order of about 0.1 meV whereas the actual interaction energies for localized moments on a crystal lattice are often 1 to 2 orders of magnitude greater than that.[1,2]

The exchange interaction instead arises from an electrostatic repulsion of the overlapping wavefunctions of electrons. In considering that the joint wavefunction of two interacting electrons must be antisymmetric and in the absence of spin-orbit coupling, we can write the combined wavefunction as the product of a spatial component ψ and a spin component χ. The spin Hamiltonian

$$\hat{H} = \mathbf{S}_i \cdot \mathbf{S}_j \tag{1.2}$$

has eigenstates of a triplet state with combined $s = 1$, aligned spins, and a singlet state with $s = 0$, oppositely aligned spins. The triplet spin state is symmetric under exchange of electrons and the singlet state is antisymmetric. Since the overall wavefunction must be antisymmetric under exchange, this requires that the triplet state has an antisymmetric spatial component and the singlet state has a symmetric spatial component. The difference in the energies associated with the spatial components of these two states can be taken as an interaction energy between spins with overlapping wavefunctions where electron-electron Coulomb interactions become important.

$$J_{\mu\nu} = E_S - E_T = \int \psi^*_\mu(\mathbf{r}_1)\psi^*_\nu(\mathbf{r}_2)\hat{H}\psi^*_\mu(\mathbf{r}_2)\psi^*_\nu(\mathbf{r}_1)\mathrm{d}\mathbf{r}_1\mathrm{d}\mathbf{r}_2 \tag{1.3}$$

When the energy of the singlet state is lower than the energy of the triplet state, the compound will display antiferromagnetic behavior and where antiparallel spins are preferred. If the triplet state has lower energy the interaction will instead by ferromagnetic. This result gives us the Heisenberg Hamiltonian that is the basis for the study of localized spin systems.

$$\hat{H} = -J \sum_{\langle \mu\nu \rangle} \hat{\mathbf{S}}_\mu \cdot \hat{\mathbf{S}}_\nu - g\beta B_O \sum_{\mu} \hat{S}^z_\mu \tag{1.4}$$

where the first term gives the sum of all interactions and the second term gives the effect of an external magnetic field B_0. Because the Coulomb repulsion of the Hamiltonian in Eqn. 1.3 will drop off like $1/r$ and thus generally speaking only the shortest interaction distances will be significant. This method of interaction that requires an overlap of wavefunctions of electrons on magnetic sites is called direct exchange and generally speaking will be most significant for $3d$ moments on transition metal compounds that spatially extend relative to the bond length. As a contrast moments from $4f$ states are highly localized and will generally not have any significant overlap.

The primary mechanism for the exchange interaction in many compounds, called superexchange, involves a similar overlap of wavefunctions but mediated by nonmagnetic intermediate ions. The nearest neighbors to transition metal cations that form the magnetic lattice will be an anion that maintains the structure of the lattice, and as a result there will a greater overlap in the electronic wavefunctions between cation-anion rather than cation-cation. This overlap leads to preferred orientations of the electronic wavefunctions that affect the energies of another neighboring cation which gives an energy associated with the coupling of two magnetic moments via a cation-anion-cation connection. Such a term allows for interaction between moments that are much more spread out than would occur with direct exchange alone. Because as an example the *p* states of O^{2-} have a preferred axial direction the overlap of wavefunctions will have a strong dependence on the cation-anion-cation bond angle and the overlap will be nearly zero for a 90° bond angle and very large for a 180° angle.

The means by which Raman spectroscopy probes magnetic order is through quasiparticle excitations of the magnetic state called magnons. In the Heisenberg Hamiltonian of Equation 1.4, the spin operators can be decomposed into quantized plane wave solutions.

$$\hat{S}_{\mu}^{-} = \hat{S}\mu^{x} - i\hat{S}\mu^{y} = \sqrt{\frac{2S}{N}} \sum_{\mathbf{q}} e^{-i\mathbf{q}\cdot\mathbf{r}_{\mu}} \hat{b}_{\mathbf{q}}^{\dagger} \tag{1.5}$$

This simplifies the Hamiltonian as a number operator of these particles.

$$\hat{H} = \sum_{\mathbf{q}} \hbar\omega_{\mathbf{q}} \hat{b}_{\mathbf{q}}^{\dagger} \hat{b}_{\mathbf{q}} \tag{1.6}$$

Details about the means by which light scattering interacts with these quasiparticles are in Section 2.5.

1.2.2 Geometric frustration

The geometry of the crystal lattice on which the magnetic moments are positioned plays a key role in the spin dynamics of the system where the number and positioning of interacting spins can affect the ability for all interaction energies to be simultaneously minimized in the system's ground states. Whereas a purely ferromagnetic compound can always have its interaction energy minimized by a parallel alignment of all spins independent of lattice geometry, in certain types of antiferromagnetic compounds this minimization is prevented by the lattice.

Figure 1.1(a) shows an antiferromagnetic square lattice where all spins are aligned antiparallel with their nearest neighbors, and the further complication that arises in a triangular lattice where interactions from competing neighbors prevents a simple alignment, Figure 1.1. Common examples of these lattices would be triangular, kagome, and pyrochlore lattices where a multitude of nearly degenerate low energy magnetic states occur from the competing interactions. In particular Figure 1.1 shows how in an Ising model of a triangular lattice will lead to degenerate states, and thus even at zero temperature gapless magnetic excitations will still exist.

Due to its simplicity, the triangle lattice remains one of the most studied frustrated systems in various forms from both a theoretical and experimental perspective.[3, 8–12] Though the Ising model of a triangular lattice has degenerate ground states, a more complete Heisenberg model leads to 120° ordering of spins at zero temperature. This has been shown theoretically for all spin values from the classical limit $S = \infty$ to the

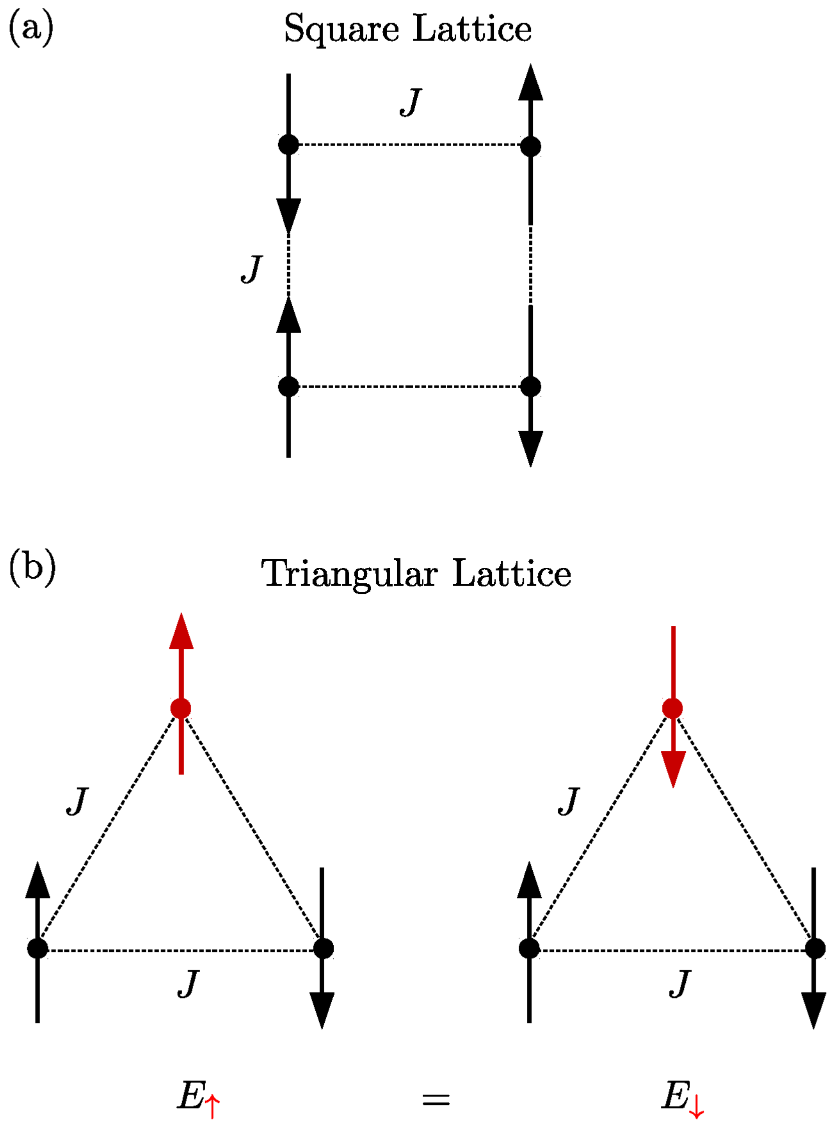

Figure 1.1: (a) Antiferromagnetic square lattice with all nearest neighbors aligned antiparallel. (b) Triangular lattice where degenerate ground states exist.

quantum limit $S = 1/2$[8,9]

Even though from a theoretical standpoint the idealized nearest-neighbor triangular lattice system is well understood, replicating these results experimentally proves difficult given the sensitivity of frustrated systems to imperfections. This work looks into characterizing the effects of minor deviations from an idealized nearest neighbor triangular lattice and the manner in which they can alter magnetic properties. In Chapter 3, we examine magneto-elastic coupling and Raman active magnetic excitations in the $S = 3/2$ anisotropic triangular lattice system $SrCr_2O_4$. Though the anisotropy of the lattice is quite small this leads to a large variation in the nearest neighbor exchange interactions that drive the system into an incommensurate helical ordering.[1,3] Understanding the coupling of the lattice to the ordered magnetic state can further elucidate the cause of the multiferroic behavior seen in this compound and at low temperatures.[13] In Chapter 4, we approach the problem of spin freezing in triangular lattice compound $NiGa_2S_4$.[10] Here competing ferromagnetic nearest neighbor and antiferromagnetic third nearest neighbor interactions lead to a spin disordered state below 10K whereas theoretical models predict an ordered ground state.[14] Through a comprehensive spectroscopic study of the compound, we find evidence for structural disorder that would lead to anisotropy within the exchange interactions that may drive the low temperature spin freezing. Along with this, by considering the crystal symmetry requirements that arise in the selection rules for Raman scattering and IR absorption we find evidence for a low temperature crystallographic inversion symmetry breaking that would allow for a Dzyaloshinskii-Moriya exchange interaction that has not been considered in modeling the ground state of this spin system.

1.3 Topological Kondo insulators

Heavy fermion materials are an active field of study in strongly-correlated physics for the modification of conductivity by the electron-electron interaction. This work explores this behavior within the compound SmB_6 which is a heavy fermion material that has been that has been studied extensively for over 50 years for a range of interesting phenomena including mixed Sm valence, Kondo insulating, low temperature resistivity plateauing, and most recently for the possibility of topologically protected surface states.

In materials with partially filled f states the Coulomb repulsion of a doubly occupied site is often significantly greater than the kinetic energy of the system at room temperature. If itinerant d bands also overlap with the Fermi energy, we will still observe metallic behavior at high temperatures where the interaction between the f and d electrons is weak by comparison to the kinetic energy scale of the material. However, at lower temperatures scattering of the itinerant d electrons by the localized magnetic moments leads to a suppression of conductivity. Below the Kondo temperature threshold, this scattering will be significant enough where the d electrons form

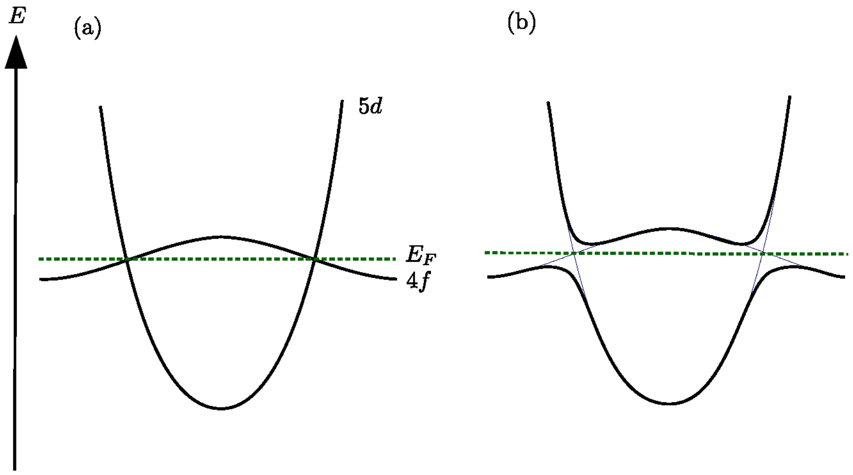

Figure 1.2: (a) Band structure of a $4f$ heavy fermion material in a noninteracting model. (b) Hybridization of d and f bands as a result of interactions between localized f electrons and itinerant d electrons which forms a band gap. If the Fermi energy lies within the hybridization gap the material will be a Kondo insulator.

spin singlets with the magnetic moments and an insulating state is formed.

The above phenomenon clearly relies on electron-electron interactions and would thus be inconsistent with a conventional band theory picture. Nonetheless, a convenient means for modelling these systems is to treat the strong electron-electron interactions as a renormalization of the d and f bands into a set of hybridized $d - f$ bands of a conventional noninteracting band insulator where a band gap forms as a result. When the Fermi energy lies within this band gap the material will display a transition from metallic to insulating behavior as it is cooled, called a Kondo insulator. As the ground state of these materials involves the formation of spin singlets that prevent the motion of the itinerant electrons, this band gap represents the energy to break one of these singlet states and occupy another lattice site.

During the mid-2000s an experimental realization of topologically protected surface states in 3D materials was achieved.[15,16] This represented a revolutionary new state of matter that was insulating in the bulk with a quantum mechanical twist in the bulk wavefunction as a consequence of the system's topology that leads to robust surface states. In these materials an inversion of bands of opposite parity brought about by spin-orbit coupling prevents an adiabatic transformation of the system from its bulk to the trivial insulator vacuum that surrounds the crystal without closing the insulating gap. These topologically distinct states are characterized by a Z_2 index which has a value of $+1$ for a conventional insulator and -1 for a topological insulator. The Z_2 index can be calculated for systems with inversion symmetry as the product of the band parities at the high symmetry points in the Brillouin zone. The gapless Dirac surface states exhibit spin-momentum locking.

The first examples of topological insulators were all conventional band insulators where the band inversion was brought about by strong spin-orbit coupling. In 2010, Dzero et al.[17] made a theoretical proposal for a topological insulator where the insulating behavior was brought about by electron-electron interactions instead. SmB_6 was proposed as a strong candidate for this type of system based on a number of experimental peculiarities. SmB_6 has long been studied for its mixed-valence of the Sm ions and as the first observed Kondo insulator with a 20 meV gap that opens at temperatures below 70K. A saturation in the resistivity that occurs in transport measurements below 5 K has been suggested to result from topologically protected surface states.

Key for the creation of topological nontriviality, the $4f$ bands in SmB_6 are odd parity and $5d$ bands even parity. The hybridization that results from the strong electron-electron interactions leads to mixed parity states at all points in the Brillouin zone except for the high symmetry points where the states and parities remain distinct. SmB_6 displays strong spin-orbit coupling and critically at the X-point the $5d$ dips below the $4f$ band leading to a Z_2 index of -1 and topological nontriviality.

Even with the strong theoretical and experimental backing for topological nontriviality in SmB_6, many questions remain with regards to evidence for bulk conductivity at low temperatures and the effect that disorder may have on these samples. In Chapter 5, we explore variations in samples with differing growth techniques and sample qualities to further understand how these factors might effect the bulk band structure and lead to conflicting experimental pictures. Raman spectroscopy proves to be a valuable technique for determining sample quality through symmetry-forbidden scattering as well as for probing the bulk band structure Additionally, we find evidence for how the low lying electronic excitations of the system are effected by the opening of the hybridization gap in different samples.

Chapter 2

Inelastic Light Scattering

2.1 Basics

Inelastic light scattering, or Raman scattering, is a phenomenon by which incident photons in the visible energy range (1.8 - 3.1 eV) excite electrons within a material which then relax back into another state by emitting a photon of a different energy, as shown in Figure 2.1. Raman spectroscopy in a general sense serves to analyze any single or multiple crystal excitations that can result from a second order light matter interaction. For the means of studying strongly-correlated electron systems of this work, we will focus on vibrational, magnetic, and electronic excitations which will be detailed further in this chapter. Figure 2.2 and 2.3 give two examples of inelastic spectra of materials that will be discussed later in this work and show the different types of excitations we study. These figures plot intensity of scattered light

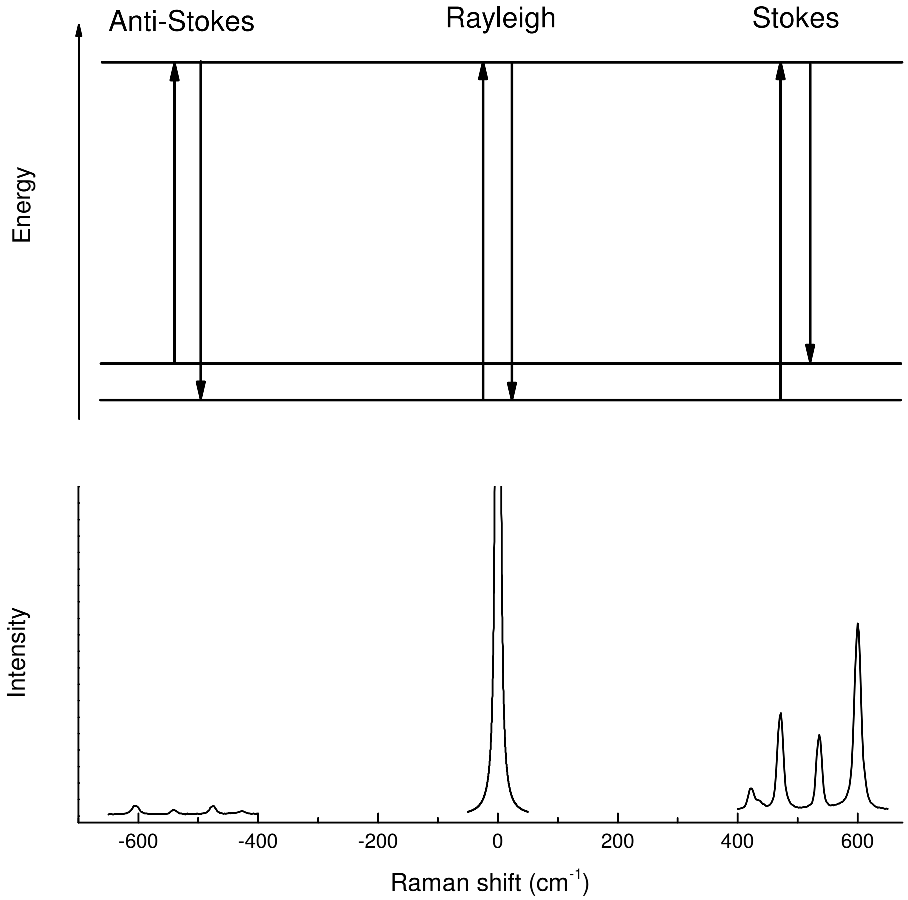

Figure 2.1: Schematic of elastic Rayleigh scattering and inelastic Raman scattering with examples of Raman spectra for the Stokes and anti-Stokes components at 300 K.

as a function of the frequency shift between the incident and scattered photons, often called Raman shift, which corresponds to the energy of the crystal excitation. For photons the relationship between energy and frequency is proportional by $E = \hbar\omega$, and throughout this work both meV and cm^{-1} will be used as units of Raman shift. The conversion factor is 1 meV = 8.065 cm^{-1}.

In Figure 2.2, we show the Raman spectrum of $SrCr_2O_4$ at 45 K near to the magnetic ordering temperature. Vibrational scattering can be seen as the narrow and

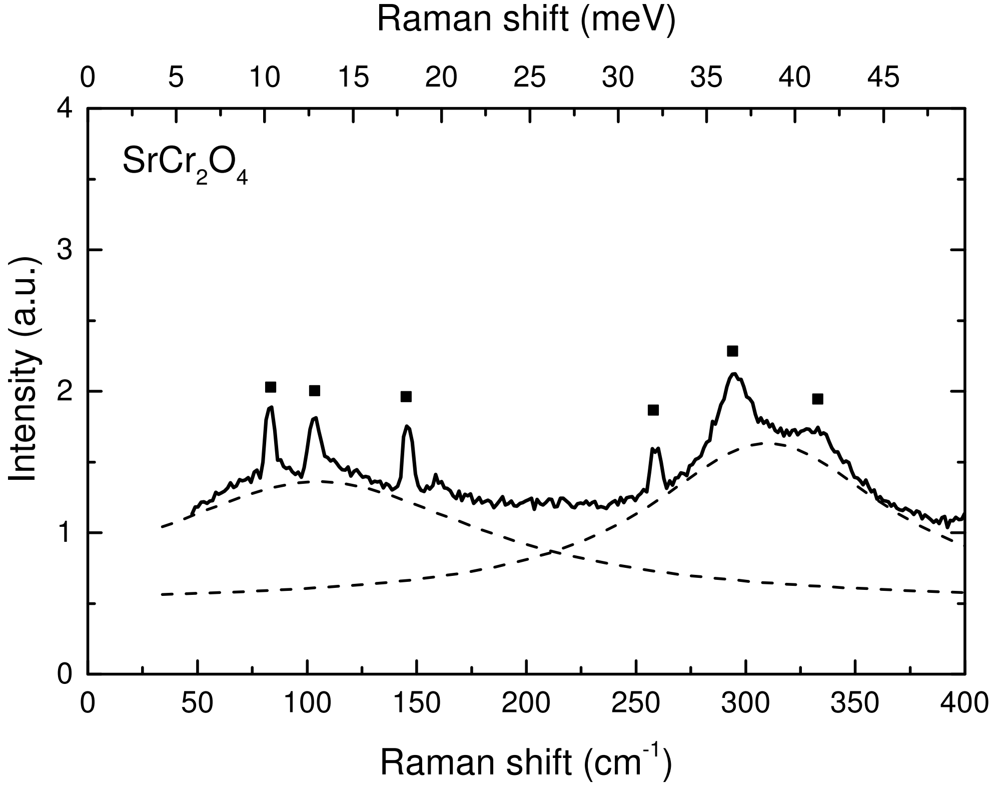

Figure 2.2: Raman spectrum of $SrCr_2O_4$ at 45 K, near to its magnetic ordering temperature, showing narrow phonon modes (black squares), and a magnetic background that forms two broad peaks at low temperatures (dashed lines).

intense peaks, for example at 81 and 102 cm^{-1} among others, that are superimposed on a magnetic continuum background that results from two-magnon scattering with much more broad bumps at 100 and 300 cm^{-1}. The Raman spectrum in Figure 2.3 is displaces the electronic excitations within SmB_6 at 15 K. Unbound electronic states appear as a continuum background and bound exciton states are seen as narrow features at 16 meV.

The inelastic scattering process can either involve a final crystal state with greater energy than its initial state, called Stokes scattering, or lower energy, called anti-

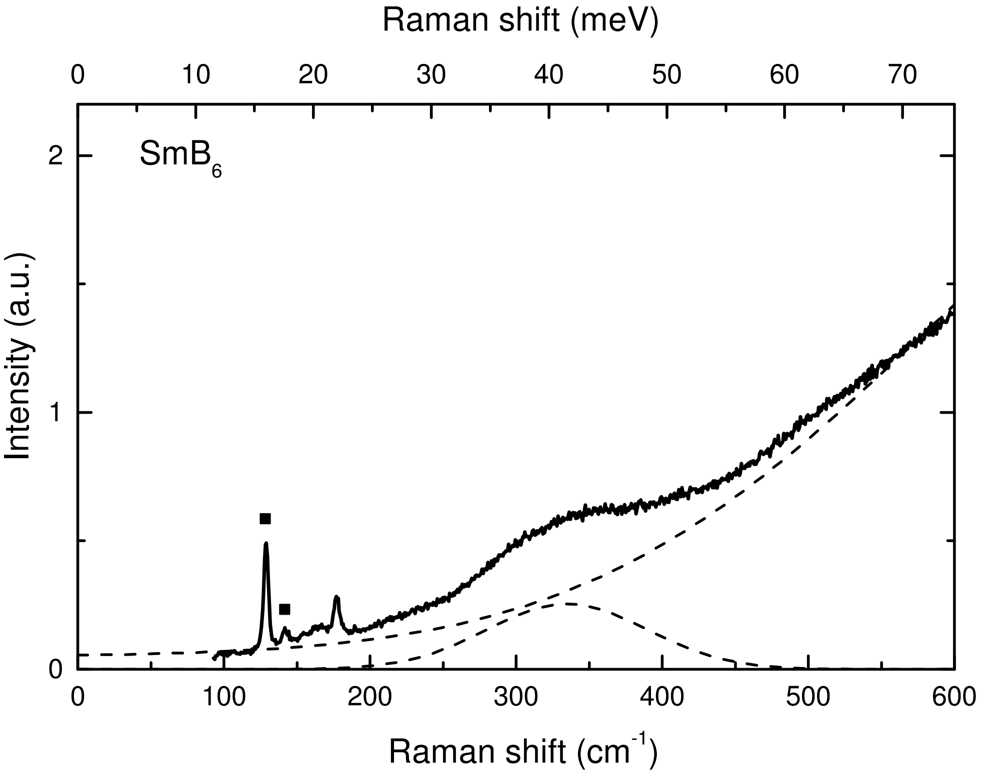

Figure 2.3: Raman spectrum of SmB_6 at 15 K showing two kinds of electronic excitations: bound excitons (black squares) at low temperatures which appear as narrow peaks due to their long lifetime and an electronic continuum (dashed lines) from excitations of conduction electrons.

Stokes scattering. Figure 2.1 gives a schematic of the three types of scattering process where an incident photon interacts with an electron to excite it to an intermediate virtual state, and then a scattered photon is released as the system relaxes. The ratio of intensities between Stokes and anti-Stokes scattering depends upon the thermal population of the excited states. In the case of the intermediate virtual state being close to a real electronic state, the scattering process will undergo a resonance with a significant enhancement of the cross section, called resonance Raman.

Unlike other common scattering techniques used in solid state physics such as x-ray and neutron scattering, visible light scattering involves photons with comparatively small momentum relative to the momentum scales brought about by the periodicity of the crystal. The typical unit cell for the materials studied is of the order 1 to 10 Å which gives reciprocal lattice vectors of about 0.6 to 6 Å^{-1}. Visible light has wavelengths from 400 to 700 nm corresponding to momenta 1.6×10^{-3} to 9.0×10^{-4} Å^{-1}, or about 3 orders of magnitude smaller than the typical Brillouin zone.

Varying the geometry of a scattering experiment has the effect of taking particular cuts through momentum space. By conservation of momentum the greatest difference in crystal momentum that can be achieved is between forward (0°) and back (180°) scattering geometries which is a difference of twice the photon momentum. This means that the portion of the Brillouin zone that can be accessed by varying the scattering geometry is relatively small compared to the zone and as a result is taken to be effectively zero momentum transfer or Γ-point excitations. This breaks down for modes which are highly dispersive around Γ such as acoustic phonons where a measurement of this dispersion can be made using different scattering geometries. The inelastic light scattering from acoustic phonons is called Brillouin scattering and typically requires the use of interferometers to measure these peaks sufficiently close to the elastic scattering line.

2.2 General theory of light scattering by matter

A semi-classical understanding of the scattered spectrum of light by matter involves considering the induced polarization P that results from incident light with electric field E_I,

$$P^i = \epsilon_0 \chi^{ij} E_I^j. \tag{2.1}$$

Here i, j are indices that refer to spatial coordinates and χ is the electric susceptibility of the material. We assume here a homogeneous material where χ has no spatial variation within the material. The incident electromagnetic wave will be monochromatic, and will thus have an electric field of the general form

$$E_I^j(\mathbf{r}, t) = E_I^j e^{i(\mathbf{k}_I \cdot \mathbf{r} - \omega_I t)} + E_I^j{}^* e^{-i(\mathbf{k}_I \cdot \mathbf{r} - \omega_I t)}. \tag{2.2}$$

with E_I^j as the complex amplitude of the wave which includes phase information, $\mathbf{k}_I$ is the wavevector, and ω_I the frequency. Next we will consider a small perturbation of susceptibility that comes about through a variation of some general coordinate $U(\mathbf{r}, t)$.

$$\chi^{ij}(U) \approx \chi_0^{ij} + \frac{\partial \chi^{ij}}{\partial U} U(\mathbf{r}, t) + ... \tag{2.3}$$

χ_0 is the value of the susceptibility when $U = 0$. We will keep only terms to first order in U as the zeroth order term produces elastic scattering, and perturbations of χ for typical crystal excitations studied in Raman are generally small relative χ_0. The cause of this deviation of the susceptibility is arbitrary at this point and as a result $U(\mathbf{r}, t)$ can be used describe any type of excitation that will be Raman-active. To simplify, the derivation we we will consider a single Fourier component of $U(\mathbf{r}, t)$ that varies spatially with wavevector q and has frequency ω. More complex motion of course be built up as a series of these components.

$$U(\mathbf{r}, t) = U e^{i(\mathbf{q}\cdot\mathbf{r} - \omega t)} + U^* e^{-i(\mathbf{q}\cdot\mathbf{r} - \omega t)}. \tag{2.4}$$

Combining Equations 2.1, 2.2, 2.3, and 2.4 gives us an induced polarization with six terms.

$$\begin{aligned} P^i(\mathbf{r},t) = {} & \epsilon_0\chi_0^{ij}(E_I^j e^{i(\mathbf{k}_I\cdot\mathbf{r}-\omega_I t)} + E_I^j{*}e^{-i(\mathbf{k}_I\cdot\mathbf{r}-\omega_I t)}) \\ & + \epsilon_0\frac{\partial\chi^{ij}}{\partial U}UE_I^j e^{i[(\mathbf{k}_I+\mathbf{q})\cdot\mathbf{r}-(\omega_I+\omega)t]} \\ & + \epsilon_0\frac{\partial\chi^{ij}}{\partial U}U^*E_I^j{*}e^{-i[(\mathbf{k}_I+\mathbf{q})\cdot\mathbf{r}-(\omega_I+\omega)t]} \\ & + \epsilon_0\frac{\partial\chi^{ij}}{\partial U}U^*E_I^j e^{i[(\mathbf{k}_I-\mathbf{q})\cdot\mathbf{r}-(\omega_I-\omega)t]} \\ & + \epsilon_0\frac{\partial\chi^{ij}}{\partial U}UE_I^j{*}e^{-i[(\mathbf{k}_I-\mathbf{q})\cdot\mathbf{r}-(\omega_I-\omega)t]} \end{aligned} \tag{2.5}$$

A great deal of information about the light scattering process can be understood from this equation. First off, we see that the spatial and time dependence of P only appears as complex exponentials meaning it will be composed of a sum of plane wave solutions. An oscillating polarization at frequency ω produces an electromagnetic wave at that same frequency which is where we get our scattered light. The first two terms involving χ_0 involve waves at frequency ω_I with wavevectors $\pm\mathbf{k}_I$. This is elastic or Rayleigh scattered light.

The second two terms give a polarization oscillating at frequency $\omega_I + \omega$ with wavevectors $\pm(\mathbf{k}_I + \mathbf{q})$. Here the scattered photon will have a greater frequency or energy than the incident photon meaning it has absorbed energy from the sample, and represents an anti-Stokes scattering process. Finally, the last two terms involve a polarization oscillating at frequency $\omega_I - \omega$ with wavevectors $\pm(\mathbf{k}_I - \mathbf{q})$ where now the scattered photon is less energetic than the incident photon meaning energy has been deposited into the sample. This is a Stokes process as described above.

A more proper understanding of inelastic light scattering considers the quantum mechanical process of photon creation and annihilation via Fermi's golden rule which gives the transition rate $\frac{1}{\tau}$ from initial state $|\alpha\rangle$ into final states $|\beta\rangle$ under the influence of some perturbative Hamiltonian. For light scattering, we consider the perturbation of an electric-dipole interaction Hamiltonian $\hat{H}_{ED}$ from the incident and scattered photons on the system. The first two terms of the golden rule will be,

$$\frac{1}{\tau} = \frac{2\pi}{\hbar^2} \sum_{\beta} \left| \langle\beta| \hat{H}_{ED} |\alpha\rangle + \frac{1}{\hbar} \sum_{\gamma} \frac{\langle\beta| \hat{H}_{ED} |\gamma\rangle \langle\gamma| \hat{H}_{ED} |\alpha\rangle}{\omega_\alpha - \omega_\gamma} \right|^2 \delta(\omega_\alpha - \omega_\beta). \tag{2.6}$$

The first term here is the more familiar first-order term that involves direct transitions from the initial to final state that are induced by the perturbative electric-dipole Hamiltonian $\hat{H}_{ED}$. Because $\hat{H}_{ED}$ appears only once, there is a single photon creation or annihilation in this matrix element. This term is responsible for single photon processes such as absorption and emission, which is the basis for many other optical techniques like infrared and visible spectroscopy. The delta function serves to conserve energy between the initial and final states, selecting only those in which the final energy $\hbar\omega_\beta$ is equal to $\hbar\omega_\alpha$. As such there may be multiple final states where energy is conserved, and thus the summation over states β. Note here that in the case of inelastic processes, energy of the whole system is conserved including any photons involved and hence the initial and final states $|\alpha\rangle$ and $|\beta\rangle$ refer to the combined system.

Light scattering of course involves both an incident and scattered photon and as a result must involve an intermediate virtual state $|\gamma\rangle$. The second term in Equation 2.6 encompasses the matrix elements that would be relevant for a two photon process. Again we have energy conservation between the initial and final states from the delta function, but since the intermediate state $|\gamma\rangle$ exists only as an intermediary state in between the annihilation and creation of the incident and scattered photons, neither dipole transition needs to strictly conserve energy.

In principle higher order terms involving three or more photons can contribute to the scattering rate, however these processes are increasingly unlikely and only make a very small contribution. In understanding the scattering process, the first-order term will be ignored. Nonetheless, it is important to recognize that the one photon luminescence process can lead to artifacts in the Raman data which can be identified by varying the incident photon energy.

Inserting the electric-dipole interaction Hamiltonian into the second-order term in Fermi's golden rule is a somewhat complicated process that is developed in Chapter 8 of Reference 18. The end result is the Kramers-Heisenberg formula, Equation 2.7, that gives the differential cross section for light scattering. Rarely are actual cross sections calculated for Raman scattering due in part to both difficulties in the theoretical calculations and experimental measurements of absolute intensities, but many qualitative features of the Raman scattering process can be understood from this formula.

$$\frac{d\sigma}{d\Omega} = \frac{e^4\omega_I\omega_S^3\eta(\omega_S)}{(4\pi\epsilon_0)^2\hbar^2c^4\eta(\omega_I)}\left|\sum_g\left(\frac{\langle f|\,\boldsymbol{\varepsilon}_S\cdot\mathbf{D}\,|g\rangle\,\langle g|\,\boldsymbol{\varepsilon}_I\cdot\mathbf{D}\,|i\rangle}{(\omega_i+\omega_I)-\omega_g}+\frac{\langle f|\,\boldsymbol{\varepsilon}_I\cdot\mathbf{D}\,|g\rangle\,\langle g|\,\boldsymbol{\varepsilon}_S\cdot\mathbf{D}\,|i\rangle}{\omega_i-(\omega_S+\omega_g)}\right)\right|^2 \tag{2.7}$$

Here we have the differential cross section $\frac{d\sigma}{d\Omega}$ for the scattering of a photon that causes an electronic transition from the initial electronic state $|i\rangle$ to the final electronic state $|f\rangle$ through a series of all possible intermediate states $|g\rangle$. Here e is the electric charge, $\hbar\omega_I$ and $\hbar\omega_S$ are the incident and scattered photon energies, $\hbar\omega_i$, $\hbar\omega_g$, and $\hbar\omega_f$ are the energies of the three electronic states, and $\eta(\omega)$ is the index of refraction for light at frequency ω. $\boldsymbol{\varepsilon}_I$ and $\boldsymbol{\varepsilon}_S$ define the orientation of the polarization of the incident and scattered photons such only the elements of the dipole operator parallel to the light polarization are involved in the transfer element.

Figure 2.4 gives a schematic for the two types of transfer matrices given in Equation 2.7. In the first term, Figure 2.4 left, we consider the process where the incident photon induces a transition from $|i\rangle$ to $|g\rangle$, and then the scattered photon is created in the relaxation to the electron's final state $|f\rangle$. However, we must also consider the process by which the scattered photon is first created in the transition from $|i\rangle$ to $|g\rangle$, and the incident photon is annihilated in the transition from $|g\rangle$ to $|f\rangle$, as shown in Figure 2.4 right.

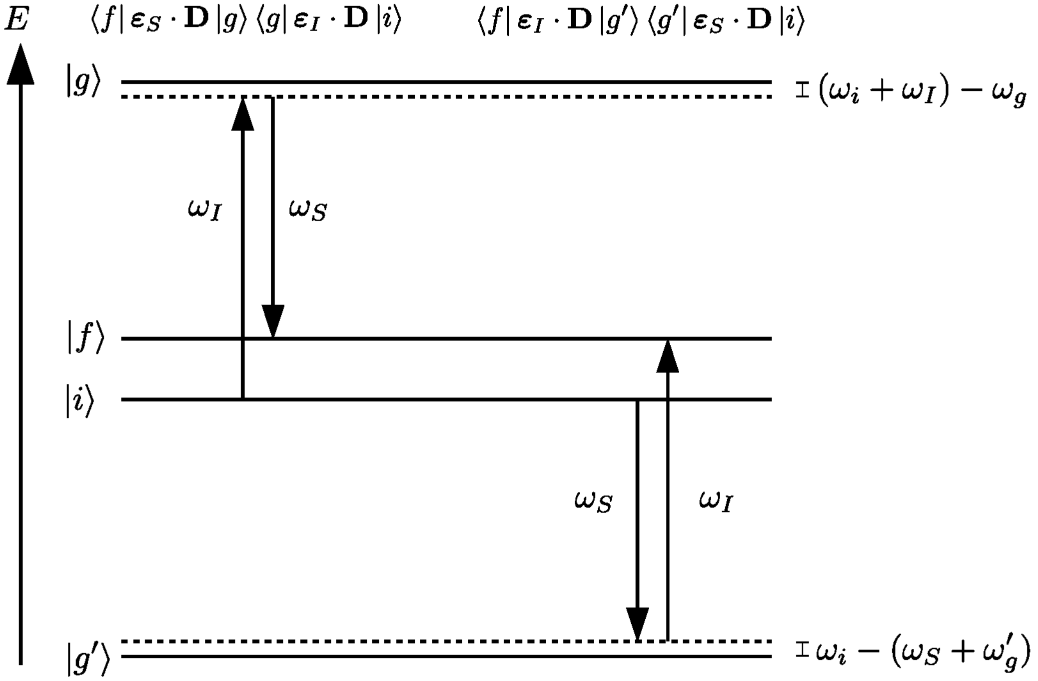

Figure 2.4: Schematic of the two types of terms in the Kramers-Heisenberg formula, Equation 2.7.

Note that the summation runs over all electronic states of the atom however the likelihood of a transition through any particular state $|g\rangle$ is normalized by how close the initial combined energy of the electron and photon, $E_0 = \hbar(\omega_i + \omega_I)$, is to the energy in the intermediate state, $E_g = \hbar\omega_g$. The fact that typical interband electronic transitions have energy scales on the order of 1 eV is the reason inelastic scattering of visible light proves to be a valuable tool. Additionally, the $\omega_I \omega_S^3$ prefactor favors scattering involving photons of higher energy and hence scattering will be strongest when the energy transfer is much smaller than the incident energy.

From the Kramers-Heisenberg formula we can begin to see the important effect in light scattering that depending on the polarizations $\boldsymbol{\varepsilon}_I$ and $\boldsymbol{\varepsilon}_S$ not all intermediate state will contribute to scattering. This comes about due to the selection rules for electric-dipole transitions that arise as a consequence of the photon's spin $S = 1$ and conservation of angular momentum in the interaction. A group theoretical approach to understanding the symmetry consequences of the scattering process is discussed further in Section 2.3.

The Kramers-Heisenberg formula holds for both elastic and inelastic two-photon scattering, and for elastic scattering we will have the simplification that $\omega_I = \omega_S$.

2.3 Symmetry requirements for scattering

Perhaps the most important aspect of inelastic light scattering is polarization selection rules that come about as group theoretical consequences of the symmetries of the scattering process. The experimentalist has the ability to select out particular polarizations of the incident and scattered photons and in doing so can measure particular elements of the susceptibility tensor χ^{ij}. The scattering process is then limited to only showing excitations of particular allowed symmetries that contribute to those terms in χ^{ij} based on the scattering geometry.

We can simplify our model of the Raman process in order to understand the implications of the symmetries of the scattering process. Consider the overall transition matrix that maps the electron from its initial state $|i\rangle$ to final state $|f\rangle$ through a perturbation on its Hamilton due to the presence of an external electric field from the incident and scattered photons. The spatial depenence of the cross section will be encompassed by the term

$$\frac{d\sigma}{d\Omega} \sim \left| \langle f| \hat{H}_{Raman} |i\rangle \right|^2 \tag{2.8}$$

$$\hat{H}_{Raman} = E_S^i \frac{\partial \chi^{ij}}{\partial U} E_I^j \tag{2.9}$$

We can note here that this matrix element gives an integral over space with the three elements $|f\rangle$, $\hat{H}_{Raman}$, and $|i\rangle$. Because this integral is over all of space, only certain symmetries of these individual elements will lead to a nonzero final integration in the same manner that a one dimensional integral of an odd function over all space is always zero whereas an integration of an even function can be nonzero. For the integral in Equation 2.8, the overall symmetry will be the product of the symmetries of the individual elements $\Gamma_f \times \Gamma_{Raman} \times \Gamma_i$. The three space matrix element of Equation 2.8 will only be nonzero when this direct product contains the fully symmetric irreducible representation as representations that are antisymmetric for any symmetry operation will cancel out when integrated over all space.

The symmetry of a crystal is given by its space group which is defined by all of the symmetry operations that leave the crystal invariant. Since Raman scattering involves negligible momentum transfer in comparison to the Brillouin zone of crystals, we can consider only net Γ-point excitations. Here translational symmetries can be ignored, and the point group of the crystal gives its relevant symmetry. The character table for a given point group contains most of the relevant information for determining allowed scattering.

As an example, Table 2.1 gives the character table for the D_{2h} point group which has orthorhombic symmetry, relevant to $SrCr_2O_4$ discussed in Chapter 3. Across the top are given the eight classes of symmetry operations for this group which map the crystal back onto itself. The left column gives the irreducible representations of the

D_{2h} point group. These are the different means by which a basis function can be effected by each of the symmetry operations of the group. The center of the table gives the character of the basis function for a given irreducible representation after undergoing each of the symmetry operations where the character gives the trace of matrix M in Equation 2.10.

$$\hat{O}\mathbf{f}(x, y, z) = M\mathbf{f}(x, y, z) \tag{2.10}$$

Because D_{2h} has only 1D representations, the characters can only be 1 or -1 depending on whether the function is even or odd under each of the symmetry operations. As mentioned the Raman scattering Hamiltonian has the spatial dependence of the 2D susceptibility derivatives, meaning the Raman active representations will be those that match the quadratic functions in the character table. A more detailed explanation of the group theoretical background for character tables and the implications for light interactions with matter can be found in Appendix A.

We can also take into account that sometimes in a scattering effect two quasiparticles will be excited. In these cases momentum conservation no longer requires that scattering arise only from zone center excitations. However, if we look at the overarching scattering process, the selection rules will come about in a similar manner where now the final state of the electron has the symmetry of the direct product of the two excitations.

Table 2.1: Character table for the D_{2h} point group which has orthorhombic symmetry

D_{2h} point group

Irr.	Symmetry operations								Functions		
Reps.	E	C_2^z	C_2^y	C_2^x	i	σ^{xy}	σ^{xz}	σ^{yz}	Lin.	Quad.	Cubic
A_g	1	1	1	1	1	1	1	1		x^2, y^2, z^2	
B_{1g}	1	1	-1	-1	1	1	-1	-1	R^z	xy	
B_{2g}	1	-1	1	-1	1	-1	1	-1	R^y	xz	
B_{3g}	1	-1	-1	1	1	-1	-1	1	R^x	yz	
A_u	1	1	1	1	-1	-1	-1	1			xyz
B_{1u}	1	1	-1	-1	-1	-1	1	1	z		z^3, $z(x^2-y^2)$
B_{2u}	1	-1	1	-1	-1	1	-1	1	y		yz^2, $y(3x^2-y^2)$
B_{3u}	1	-1	-1	1	-1	1	1	-1	x		xz^2, $x(x^2-3y^2)$

2.4 Vibrational scattering

2.4.1 First-order scattering

Vibrational scattering quantum mechanically involves the creation of collective excitations called phonons. As a consequence of momentum conservation in the scattering process first-order vibrational scattering probes only phonons near the Γ-point where displacements of ions in neighboring cells are in-phase with each other. This process effectively takes a cut of phonon energies through the Brillouin zone at zero momentum transfer with the measured scattering linewidths giving information about the phonon lifetime.

A minor point of clarification should be made here about the usage of the terms first-order and second-order. As discussed in Section 2.2, Raman scattering is a second-order effect in the interaction of light with matter because it involves the creation or annihilation of two photons, contrasting absorption which is referred to as first-order because it involves only a single photon. In discussing types of Raman-active excitations, first and second order will also be used to refer to the number of quasiparticles created within a particular scattering process. For example, first-order vibration scattering refers to the process where a single phonon is created in the inelastic scattering of light, but the scattering process itself is still a second-order process in the interaction of photons with matter.

As shown in Section 2.2, light scattering results from modulations of the electric susceptibility, or polarizability, as a result of a particular excitation whereas absorption instead comes about from excitations that directly involve an oscillating dipole moment. Here is where we develop the concept of Raman and IR activity that depending on the symmetry of the crystal may be mutually exclusive.

This can be illustrated quite clearly with a linear molecule with inversion symmetry such as CO_2, Figure 2.5, which has $3N-5=4$ vibrational modes. Molecular vibrations involve no net momentum and thus are similar probed in spectroscopy like Γ-point phonons. An example of an IR active mode would be the asymmetric stretching mode where the C atom moves out of phase with the O atoms. Since the O is more electronegative than the C this motion has the effect of inducing a dipole moment along the z, axial, direction that allows for IR activity. To contrast, if we consider the change in the susceptibility as the atoms are displaced in one direction we see that the susceptibility will be altered in exactly the same way if the atoms

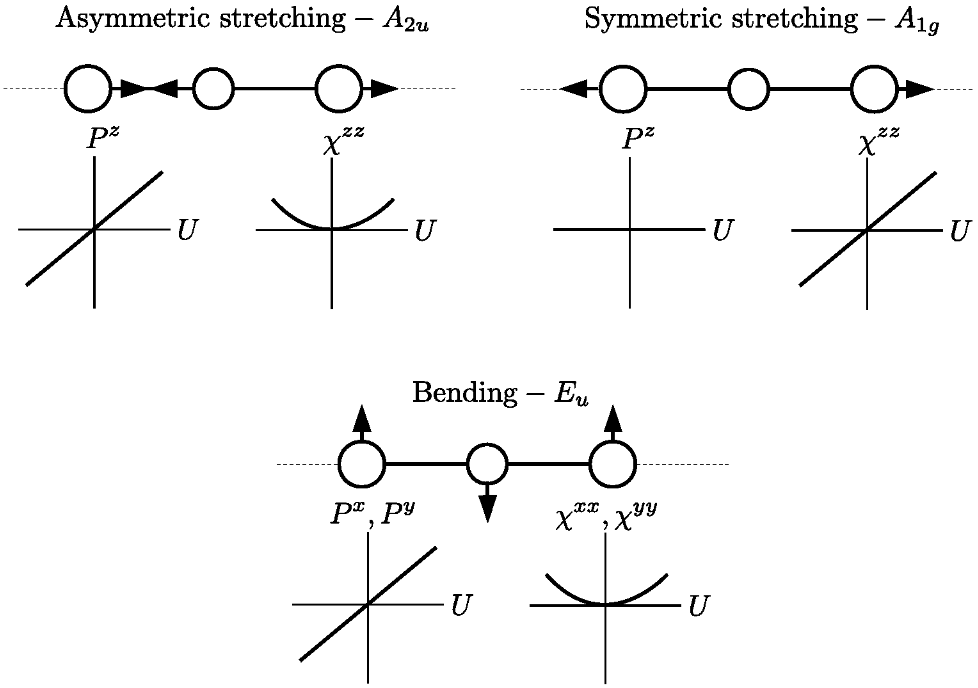

Figure 2.5: Vibrational modes of CO_2 and their Raman and IR activity.

are displaced in the opposite direction. Since the Stokes and anti-Stokes terms of Equation. 2.5 necessary for inelastic scattering depend on there being a nonzero $\frac{\partial\chi}{\partial U}$ term when expanded about $U = 0$, we can see that this oscillation will be forbidden from causing Raman scattering. The two bending modes exhibit the same properties with regards to dipoles and susceptibility and are similarly IR active and Raman forbidden.

The symmetric stretching mode on the other hand involves no oscillating dipole moment as the negatively charged O atoms move back and forth equally canceling each other's effect. At a simple level we can expect the susceptibility to change where when the molecule is stretched the electrons will have more potential to move along the z direction to create a dipole moment as the result of an electric field, and when it is compressed they will be more limited in this spatial mobility. As a result $\frac{\partial \chi}{\partial U} \neq 0$ when $U = 0$ and the mode will be Raman, but not IR active.

If the inversion symmetry in CO_2 were to be broken both the oscillating dipole and the susceptibility derivative would be nonzero for all modes, and thus all modes would be both Raman and infrared active. We demonstrate the usefulness in the complementary usage of Raman and IR spectroscopy at detecting symmetry changes in Ch. 4.

The basic ideas here with respect to molecular vibrations can be applied very directly to phonons excited on a crystal lattice. In probing only Γ-point excitations vibrational spectroscopy in crystals has the same restriction for molecular vibrations where the overall momentum is zero throughout the vibration. For a crystal this means that neighboring unit cells will display identical motion and be in phase with each other. Without taking into account degeneracies, number of phonon branches will be $3N$ with N atoms in the unit cell. Of these branches, three will be acoustic modes for each of the three spatial coordinates. Though the underlying concepts of scattering for Brillouin spectroscopy which studies these acoustic modes are identical to Raman spectroscopy the technical consequences of the low energy of the acoustic modes near the Γ makes these spectroscopies quite distinct experimental methods.

This work will only discuss Raman spectroscopy which probes the remaining $3N - 3$ optical modes in crystals where there are more than two atoms per unit cell. These modes tend to be flat near the zone center meaning that the small but finite photon momentum can be ignored. As with molecular vibrations, not all modes will be Raman or infrared active depending on whether they involve a modulation of the susceptibility or a dipole moment, respectively.

2.4.2 Second-order scattering

Second-order vibrational scattering results when two photons are excited in the scattering process. Momentum conservation holds that

$$\mathbf{k}_I - \mathbf{k}_S = \mathbf{q} + \mathbf{q}' \approx 0 \tag{2.11}$$

$$\omega_I - \omega_S = \omega_{\sigma\mathbf{q}} + \omega_{\sigma'\mathbf{q}} \tag{2.12}$$

where it is already taken $\mathbf{q} = -\mathbf{q}'$ and that $\omega(\mathbf{q}) = \omega(-\mathbf{q})$. ω and ω' refer to the phonon branches. Scattering intensity will be strongest at the energies of Van-Hove singularities that are defined by

$$\nabla_{\mathbf{q}}(\omega_{\sigma\mathbf{q}} + \omega_{\sigma'\mathbf{q}}) = 0. \tag{2.13}$$

At a general point in the Brillouin zone that does not lie along one of the high symmetry directions, there will be no symmetry operations for the crystal, which will be represented by the trivial C_1 point group. For trivial symmetry, no absolute selection rules emerge for light scattering measurements, and thus scattering will be allowed in all polarizations. Since the sharp features that occur in the two magnon spectrum tend to be brought about by flat dispersions near high symmetry points, which do have selection rules, the polarization geometry can be used to suppress scattering from different locations within the Brillouin zone.

2.4.3 Defect scattering

To this point we have considered only perfect crystals which have well defined selection rules based on the crystal point group. In practical applications many crystals have defects in their crystal structure that can serve to relax these symmetry requirements. A single point defect completely breaks the discrete translational symmetry of the crystal that holds that all scattering must involve no net change in crystal momentum, and thus allows scattering from all points within the Brillouin zone. For randomly ordered defects, rather than discrete finite momentum cuts in the Brillouin zone, we will instead see a weighted one-phonon density of states, where peaks occur at locations of Van Hove singularities (Equation 2.14). Unless the defects are ordered, a crystal will lose its symmetries, and in particular because of the loss of inversion symmetry, we can generally expect Raman and infrared selection rules to be relaxed.

$$\nabla_{\mathbf{q}}\omega_{\sigma\mathbf{q}} = 0 \tag{2.14}$$

2.5 Magnetic scattering

The primary means through which light interacts with matter is by electric dipole transitions. In order for a magnon to be excited in this process it is therefore necessary for there to be some coupling between the electron spin in the material and its orbital angular momentum, which is effected by a dipole transition, at the magnetic ion. In the first-order inelastic magnetic scattering process strong spin-orbit is required where the intermediate states do not have well defined spin and orbital angular momentum and thus a transition matrix element can involve a transfer of angular momentum from the photon to the electron spin[19]

A peculiarity was found in the experimental magnetic inelastic spectra of many antiferromagnetic materials (Refs at CL pg 8) that second-order magnetic scattering is often equal to or greater in intensity than first-order magnetic scattering. Rather than a spin-orbit mediated process, a completely different scattering mechanism called exchange scattering is responsible for the two-magnon scattering scattering seen in many antiferromagnetic compounds. Exchange scattering involves the interchange of electrons oriented antiparallel without manipulation of either spin.

Figure 2.6 shows a schematic of the exchange scattering mechanism. Here we consider electrons on two neighboring lattice sites μ and ν of a 1D antiferromagnetic spin chain such that the spin for the electron at μ is up and ν is down in their ground states. The lowest energy orbital assumed to be $L = 0$, s, here will again be split by the values of the electron spin due to the exchange field. There will also exist some higher energy orbitals labeled here as p. The first step of this process will be for the incident photon to invoke an electric dipole transition on the μ site electron to excite it into the p_μ state with its spin unaltered. Next an exchange of lattice sites occurs that is mediated by the mutual Coulomb repulsion where now the electron that was initially on the ν site is in an excited s_μ state by maintaining its spin down state. The final step is for the spin up electron in the p_ν state to via an electric-dipole relax down to the s_ν state maintaining its spin up S^z component. The final state is such that the two electrons traded lattice locations which results in two spin flips though because this occurs on neighboring sites, magnon-magnon interactions have a particular importance. This process happens without a change in either electron's spin and thus does not have a need for spin-orbit coupling to be brought about by an interaction with light.

The transfer matrix elements can be written as,

$$\left| \langle s_{\nu\uparrow}(\mathbf{r}_1)|\, e\hat{\mathbf{E}}_S \cdot \mathbf{r}_1 \,|p_{\nu\uparrow}(\mathbf{r}_1)\rangle \, \langle p_{\nu\uparrow}(\mathbf{r}_1) s_{\mu\downarrow}(\mathbf{r}_2)|\, \frac{e^2}{4\pi\epsilon_0|\mathbf{r}_1 - \mathbf{r}_2|} \,|s_{\nu\downarrow}(\mathbf{r}_2) p_{\mu\uparrow}(\mathbf{r}_1)\rangle \, \langle p_{\mu\uparrow}(\mathbf{r}_1)|\, e\hat{\mathbf{E}}_I \cdot \mathbf{r}_1 \,|s_{\mu\uparrow}(\mathbf{r}_1)\rangle \right|^2 \tag{2.15}$$

where $\mathbf{r}_1$ and $\mathbf{r}_2$ are the positions of the two electrons. The first and last elements describe the absorption and reemission of the incident photon while the electron is excited and relaxed. The middle element is the Coulomb interaction responsible for the electron exchange. The overlap of these orbitals determines which polarization

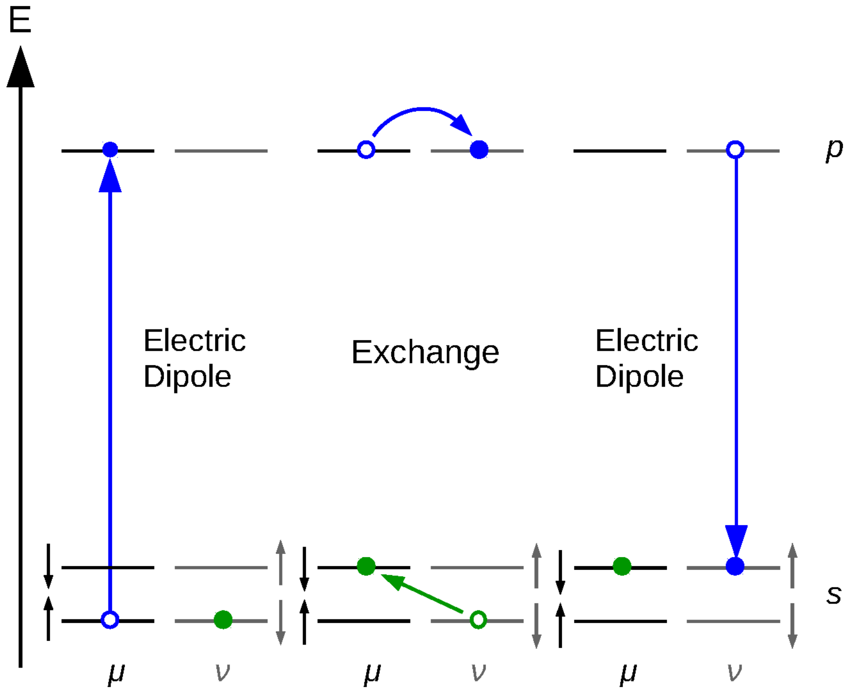

Figure 2.6: Second-order magnetic inelastic scattering

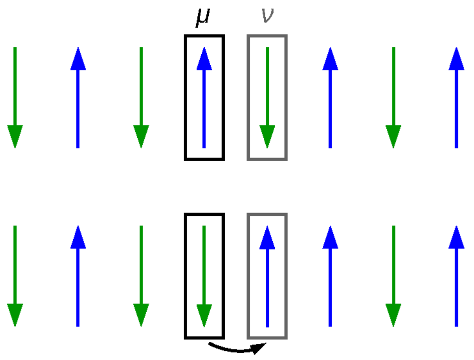

Figure 2.7: Electron exchange resulting in the excitation of two magnons at neighboring sites.

vectors in the dipole transitions will be able to cause exchange scattering.

Assuming the compound has only one magnetic site per primitive cell on the magnetic lattice, there will only be one magnon branch, and thus conservation of momentum, in the absence of disorder, holds that a two-magnon process must involve identical magnons with opposite momentum. As a consequence the two-magnon density of states will be identical to the one-magnon density of states with the energy scale doubled, and the Van Hove singularities that result in peaks in the Raman spectrum will occur at double the energy of the Van Hove singularities in the one-magnon density of states.

$$\mathbf{k}_I - \mathbf{k}_S = \mathbf{q}_1 + \mathbf{q}_2 \approx 0 \tag{2.16}$$

$$\omega_I - \omega_S = \omega_{\mathbf{k}} + \omega_{\textbf{-k}} = 2\omega_{\mathbf{k}} \tag{2.17}$$

However, the magnetic Raman spectrum does not identically match the two-magnon density of states. First because of the polarization of the incident and scattered light, only certain elements of the susceptibility tensor will be probed, and excitations will be limited to only those for which transitions are allowed. This has the effect of causing the Raman response to be a weighted average of the two-magnon density of states across the Brillouin zone.

Secondly, as stated previously, because the Coulomb potential that mediates the exchange scattering falls off with distance, the scattering will primarily involve exchange of neighboring electrons. As a result, the spectral weight will be shifted to lower energies by magnon-magnon interactions. As an example, in a collinear antiferromagnetic ground state the excitation of two non-interacting spin flips would normally require an energy transfer of $4JzS$ where z is the number of nearest neighbors, $2J$ is the interaction energy, and S is the spin. However, because these spin flips occur on neighboring sites the interaction between them will remain in its energetically favorable state, and thus the energy cost of the exchange will be lowered by J giving $2J(2zS - 1)$.

Such an analysis assumes a collinear antiferromagnetic ground state. Much of this work focuses on geometrically frustrated systems where even in an ordered state all spins cannot align antiparallel and as a result the two-magnon spectral weight occurs well below this $J(2JzS - 1)$, and a more specific theoretical analysis is necessary to predict the relevant energies.

2.6 Electronic scattering

Electronic scattering involves electric-dipole interactions with the incident and scattered photons like the previous mechanisms discussed, but with the net effect of leaving the electron in an excited state after the scattered photon has been created.

Interband and intraband electronic transitions are often considered to create two particles: an electron with some momentum $\mathbf{k}_e$ and a positively charged hole with momentum $\mathbf{k}_h$ that the electron initially had before it was excited. This makes momentum conservation be

$$\mathbf{k}_I - \mathbf{k}_S = \mathbf{k}_e + \mathbf{k}_h \tag{2.18}$$

The above relation holds that light scattering can only probe excitations where the momenta of the electron and hole are the same, or the electron's momentum remains unchanged, direct transitions. However, momentum conservation places no restrictions on which electrons within the Brillouin zone can be excited. The measured spectrum in this case will represent the joint density of states weighted by a factor allowing for scattering selection rules and geometry. The symmetry requirements on the transition matrix of the scattering process from Section 2.3 hold, but with the limitation that in general the electronic wavefunctions only have high symmetry at certain points within the Brillouin zone. These symmetry requirements will suppress certain transitions at these high symmetry points, and thus by varying the incident and scattered polarizations, Raman spectroscopy can identify excitations that result primarily from particular points within the Brillouin zone.

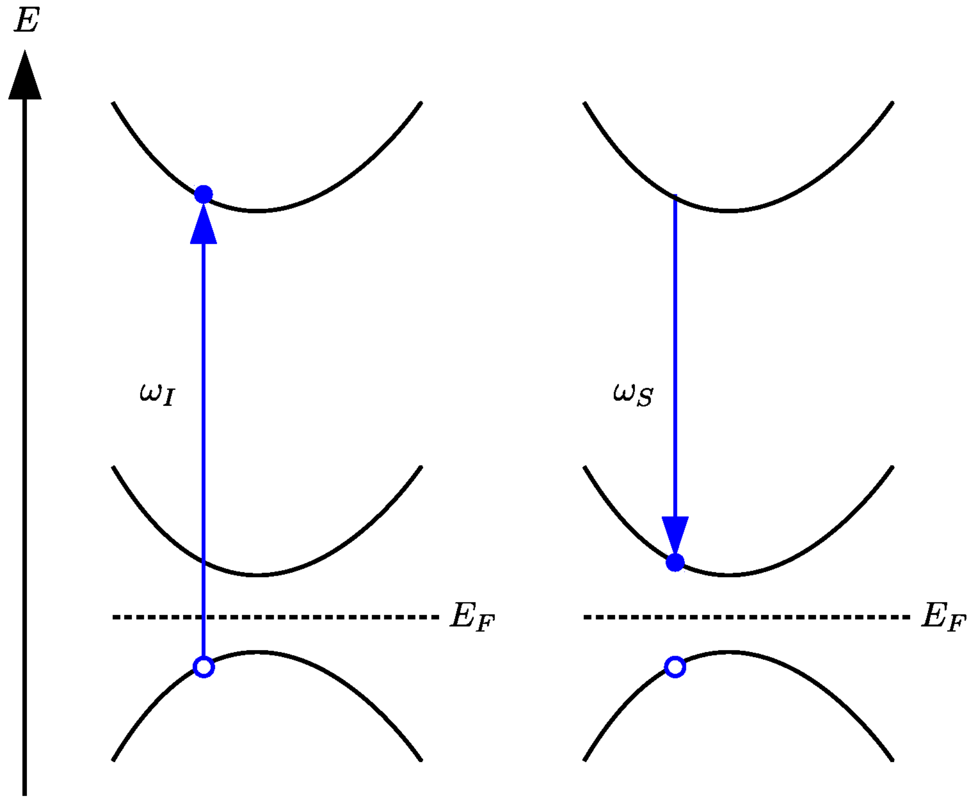

Figure 2.8: The photon annihilation and creation steps involved in an electronic scattering process mediated by an intermediate electronic state. The net result involves an electronic in one of the excited bands and the creation of a hole.

2.7 Experiment

In analyzing the materials of this work, three Raman setups were used. The geometry of the macro-Raman setups allowed for better laser light rejection and low frequency measurements and were used in making sensitive measurements of the background continuum in particular in $SrCr_2O_4$ and SmB_6. The micro-Raman setup has a much finer beam size to identify spatial variations in samples down to 2 μm and was used primarily for sample characterizations at 300 K but also low temperature measurements in $NiGa_2S_4$.

The experimental setup for measuring a Raman scattering spectrum can be broken down into the production of incident photons, the sample environment, and the measurement of scattered photons. A simple schematic showing the important components of a Raman system is given in Figure 2.9.

An ion laser is used to create the incident photons due to its narrow linewidth and well calibrated frequency which are necessary for measurements down to small Raman shifts of about 5 cm^{-1}. Several Coherent, Inc. and Spectra Physics Ar^+ gas and $Ar^+ - Kr^+$ mixed gas lasers were used in the course of this work. By varying the energy of the incident photons, one-photon effects such as luminescence, which appearing as artifacts in the spectrum and be distinguished from the two-photon scattering process being measured. The most intense lines of Ar gas, 514.5 and 488.0 nm, were primarily used for measurements. When using the Kr gas laser, the 647 cm^{-1} line was also used.

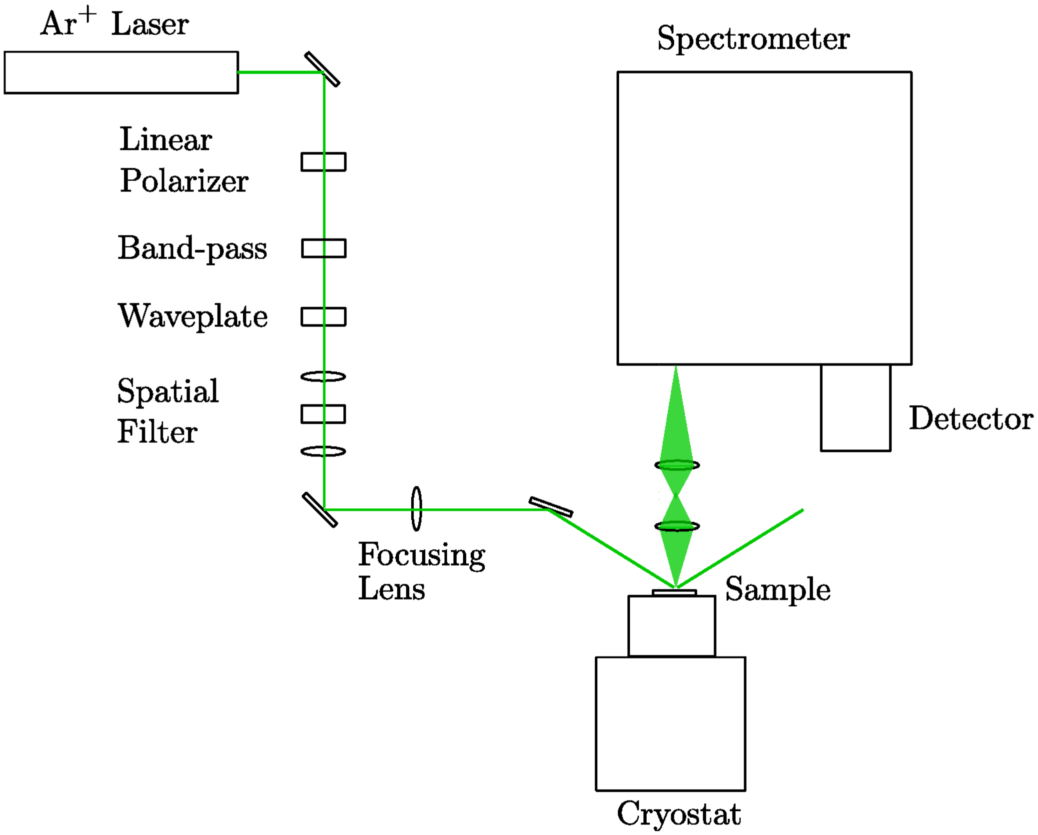

Figure 2.9: Schematic of major components of experimental Raman scattering setup.

The laser emits polarized photons with energies centered around laser line. A band-pass filter centered on the emission line typically with a pass-band of about 1 nm removes all other emission lines from the spectrum. A polarizer is used to verify the photons' polarization is oriented with the rest of the system. Waveplates are used to either rotate the orientation of the polarization, by a $\lambda/2$ waveplate, or create left or right circular polarization, by a $\lambda/4$ waveplate. A spatial filter composed of a focusing lens, pinhole, and a lens to make the beam parallel again removes any resonant modes other TEM_{00} spatially symmetric mode as well as any spatial artifacts that result from the optical elements before the filter. Finally, the laser beam is focused on the sample to maximize the intensity at the location of the measurement.

Macro-Raman and micro-Raman setups were used which are primarily defined by their differences in focus size of the laser beam on the sample, $\sim 50\mu$m for macro and $\sim 2\mu$m for micro, and their intended applications.

The scattering geometry show in Figure 2.9 is used for macro-Raman referred as pseudo-Brewster's angle scattering because the scattering angle is approximately 60° which is near to the typical Brewster's angle for the Mott-insulating crystals studied in this work. The key advantage of this type of geometry is the reflected light from the sample surface is directed away from the collection optics, and thus there is significantly less elastic light that needs to be filtered out of the spectrum. The comparatively low intensity of the elastic line means that low energy inelastic features in the spectrum can be measured. The macro-Raman spectrometers were used to measure energies as low as 5 cm^{-1}or 0.62 meV. The nearness of the scattering angle to the Brewster's angle means that within the bulk of the sample the light will be predominantly plane polarized regardless of the polarization of the incident light.

The micro-Raman setup involved a backscattering geometry where the incident photons are instead parallel to the sample surface. The 2 μm beam size allows for spatial dependences of sample surfaces. However, in this setup the incident beam is reflected directly back along the optical pathway to the spectrometer and thus is more difficult to filter out for low energy measurements. This setup also has the drawback of adding additional optical elements which can introduce artifacts to the measured spectrum, such as a broad increase in background scattering, and therefore measurements on the macro-Raman setup are generally preferred when possible.

The photons scattered perpendicular to the sample surface are pass through a collecting lens and a lens that focuses the beam spot on the entrance slit of the spectrometer. Two spectrometers used for measurements, a Jobin-Yvon U1000 double monochromator spectrometer with a photomultiplier tube (PMT) detector and a Horiba Jobin-Yvon T64000 triple monochromator spectrometer with a charge-coupled device (CCD) detector.

The simpler setup involves the T64000 in single monochromator mode where the scattered photons are redirected to bypass the first two monochromators and instead enter an entrance slit at the final monochromator before the detector. Here a 600 or 1800 gr/mm diffraction grating disperses the light in the vertical direction. The CCD

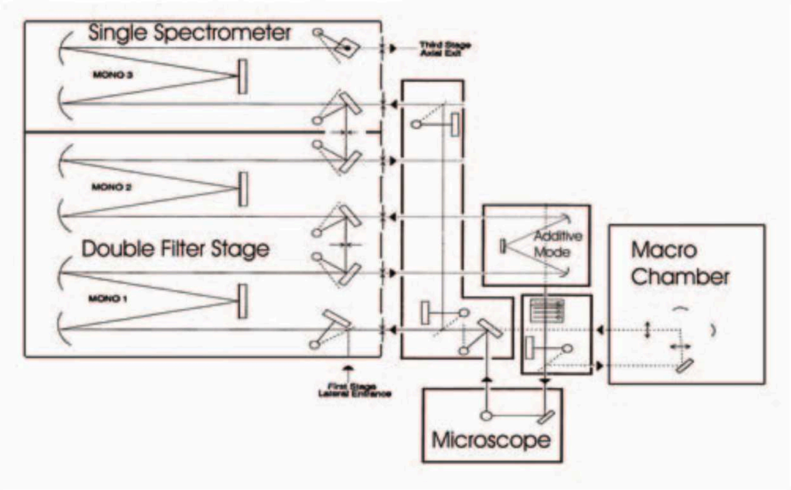

Figure 2.10: Schematic of the T64000 triple monochromator spectrometer provided by Horiba Jobin Yvon. Seen here is the single spectrometer that measures the photon energy within a particular range, and the double monochromator that can be used as a band pass filter in subtractive mode or to increase resolution in additive mode.

detector is then positioned such that it only intercepts the photons from a particular energy range. Because a CCD is an area detector the spatial location of the photon on the detector across its vertical axis gives information about its energy. An integration of photons across a particular range of the horizontal axis can be chosen to minimize the background resulting from dark current. The entrance slit was typically chosen to be 100 μm for this setup which gave a resolution of about 2 cm^{-1}.

The elastic line is filter by a high pass dielectric optical filter to separate elastic scattering from the Raman scattering, which is several orders of magnitude weaker. This filter however prevents the measurement of very small Raman shifts of less than about 70 cm^{-1} but has larger throughput than the triple monochromator options.

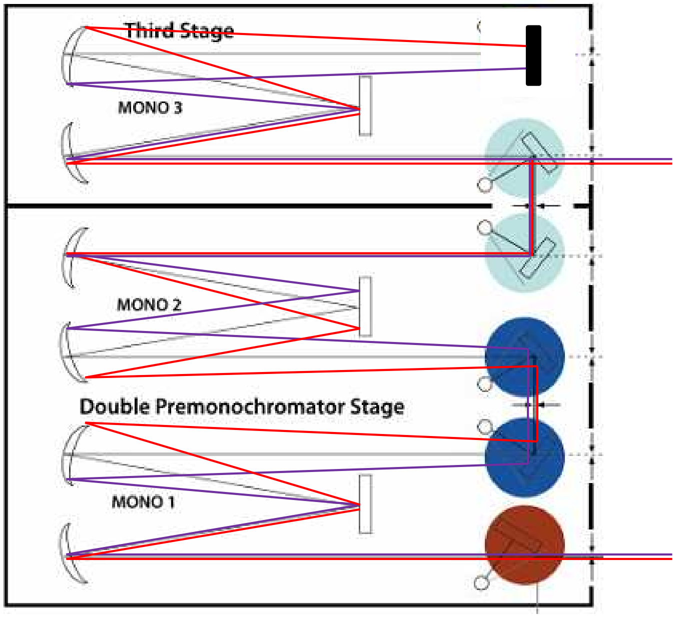

Figure 2.11: Schematic of subtractive triple monochromator mode for the T64000 spectrometer. The first two stages of the triple monochromator act as a band pass filter allowing low frequency measurements. Figure adapted from schematic provided by Horiba Jobin Yvon.

The T64000 can also be configured in a subtractive triple monochromator setup where the first two monochromators act as a band pass filter which allows low frequency measurements, Figure 2.11. In this configuration the scattered light is passes through the first monochromator and is dispersed by an 1800 gr/mm grating. The light is then focused on a slit that removes light outside the desired frequency range. The second monochromator is positioned such that the light is dispersed in the opposite direction resulting in a beam of light that has no spatial dependence on frequency. Finally, this light is sent through the last monochromator described in the single monochromator setup which measures the frequency. The net effect is a band-pass filter before the final monochromator which allows low energy measurements down to as low as 5 cm^{-1}. Because the first two monochromators act only as a filter, the resolution and intensities are comparable to the single monochromator mode.

The U1000 is a double monochromator spectrometer with a PMT point detector, Figure 2.12. The two monochromators for this spectrometer are situated such that the gratings act constructively to further disperse the light, referred to as an additive configuration. This allows for a more limited range of photon frequencies to pass through and thus for a given grating, slit width, and spectrometer length will give higher resolution. The PMT detector has no spatial detection so all photons that pass through the final slit are measured for a given energy, then the diffraction grating positions are incremented to measure a range of energies.

Along with the additive versus subtractive grating setups, the key difference be-

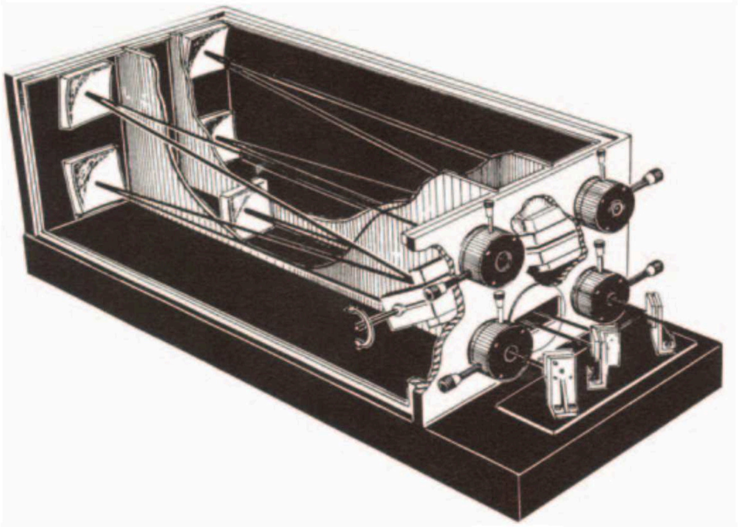

Figure 2.12: Schematic of the U1000 double monochromator spectrometer provided by Horiba Jobin Yvon. Spectrometer is always setup in an additive mode to only allow a narrow range of energies through to the PMT point detector at the exit slit.

tween the T64000 and U1000 setups is the area versus the point detector. The area detector has the advantage of the CCD area detector in the T64000 is that because different photon frequencies are dispersed across the detector a range of frequencies can be measured at once. However, the finite size of the detector pixel, places a limit on the resolution that can be achieved to about 2 $\mathrm{cm}^{-1}$for the single and triple-subtractive modes with an 1800 gr/mm grating. For the spectra studied in this work features were broader than this resolution meaning the T64000 setup was generally preferable for its additional counting time. Nonetheless, for measurements were a higher resolution would be needed the resolution of the U1000 is limited only by precision in the size of the slits and the loss of intensity with closing the slits.

Materials in this work are studied at or below room temperature meaning for majority of the energy range of typical excitations studied by inelastic light scattering (10 - 2500 cm^{-1}), the system will primarily be in its ground state. As a result, Stokes scattering which involves exciting the system from its ground state and is governed by a thermal factor $n(\omega)+1$ will be significantly more intense even at room temperature than anti-Stokes scattering which requires populated excited states and is governed by a $n(\omega)$ thermal factor. Here $n(\omega)$ is the Bose-Einstein thermal factor given as

$$n(\omega) = \frac{1}{e^{-\frac{\hbar\omega}{k_B T}} - 1}. \tag{2.19}$$

As a result, the ratio of the intensities for Stokes and anti-Stokes scattering is given by

$$\frac{I_{AS}}{I_S} = \frac{n(\omega)}{n(\omega)+1}. \tag{2.20}$$

At room temperature, the anti-Stokes scattering cross section measured across a typical range of 100 to 600 cm^{-1} for measuring phonons will vary from 79% down to 6% of the Stokes scattering cross section, Figure 2.1. The anti-Stokes side will decrease in intensity for the low temperatures relevant for the study of many strongly-correlated materials.

The anti-Stokes scattering however proves valuable in measuring the local temperature of the sample. Because the Raman process is relatively weak large laser intensities of up to 10 mW for a beam spot of about 50 μm in diameter are necessary.

This leads to significant laser heating of the sample that needs to be accounted for, in particular at temperatures between 4 and 50 K. Measuring the ratio of Stokes to anti-Stokes scattering and inversing Equation 2.20, one can determine the temperature of the sample at the location of the scattering. This laser heating can vary from sample to sample depending on their thermal properties, but typically ranges from 10 to 20 K at low temperatures for the samples studied and the laser intensities used.

Chapter 3

Magnetic excitations and magneto-elastic coupling in α-SrCr$_2$O$_4$

3.1 Introduction

The triangular-lattice Heisenberg antiferromagnet is a central model in frustrated magnetism. The theoretically established ground state has long-range magnetic order for any spin (including $S = 1/2$), with moments ordered in a coplanar 120° structure.[8,9,20] For sufficiently large S, the magnetic excitation spectrum is well captured by spin-wave theory with strong magnon interactions due to the non-collinear character of the magnetic order.[21–24] We investigate the sensitivity of triangular-lattice systems to deviations in structure through the anisotropic triangular-lattice Heisenberg antiferromagnet α-SrCr$_2$O$_4$.

While numerous quasi-two-dimensional triangular-lattice materials are known, their ground-state properties and magnetic excitations are often profoundly modified by exchange anisotropies and interactions beyond the nearest-neighbor Heisenberg model. Examples include the distorted triangular geometry in Cs_2CuCl_4,[11] spin-space anisotropy in $Ba_3CoSb_2O_9$,[25,26] further neighbor exchange interactions in $CuCrO_2$[27] and $LuMnO_3$,[28,29] and delocalized spins in κ-(BEDT-TTF)$_2$Cu$_2$(CN)$_3$[30] and $LiZn_2Mo_3O_8$.[12,31]

α-CaCr$_2$O$_4$ and α-SrCr$_2$O$_4$ belong to yet another family of triangular-lattice Heisenberg antiferromagnets with a distorted lattice. Their low-temperature properties attracted attention due to the development of an incommensurate helical magnetic order below $T_{\mathrm{N}} \approx 43$ K,[2,3,6] multiferroic behavior,[13,32] and unconventional spin dynamics.[7,33,34] In α-SrCr$_2$O$_4$, non-monotonic changes in lattice parameters were observed around $T \approx 100$ K by synchrotron X-ray powder diffraction,[3] and a small electric polarization ($P \leq 0.4\ \mu\mathrm{Cm}^{-2}$) was detected below T_{N} under a poling electric field.[13] Symmetry analysis for the currently accepted nuclear and spin structures indicates linear magneto-electric effects are forbidden while quadratic terms are allowed.[6,32] The lattice and spin dynamics of α-SrCr$_2$O$_4$ is thus of particular interest to search for possible magneto-vibrational effects and lattice distortions beyond the reported paramagnetic $Pmmn$ space group.

CHAPTER 3. MAGNETIC EXCITATIONS AND MAGNETO-ELASTIC COUPLING IN α-SrCr$_2$O$_4$

Originating from almost structurally perfect triangular layers of $S = 3/2$ ions, the collective magnetism of α-SrCr$_2$O$_4$ is particularly interesting. A Curie-Weiss fit to the magnetic susceptibility for temperatures above T=150 K indicates overall strong antiferromagnetic interactions between Cr^{3+} spins with a Weiss constant $\Theta_{\mathrm{W}} \approx -596$ K.[3] Below $T_{\mathrm{N}} \approx 43$ K, the onset of long-range magnetic order is indicated by sharp λ-anomaly in the specific-heat[3,13,35] and the concomitant appearance of an incommensurate magnetic Bragg peak in neutron diffraction indexed by the propagation vector $\boldsymbol{k} = (0, 0.322, 0)$.[3] The magnetic structure is an incommensurate *spin helix* with spins in the *ac* plane. This is distinct from the 120° ground-state of the nearest-neighbor triangular-lattice Heisenberg antiferromagnet.

In this chapter, we present comprehensive Raman scattering results from α-SrCr$_2$O$_4$ single crystals and address the interplay between lattice dynamics and magnetism. Raman scattering is a valuable tool in studies of frustrated magnetism due to its sensitivity to local structure and symmetry and to magnetic exchange interactions through optical phonons and two-magnon scattering,[19] respectively. In some cases, Raman scattering has proven more sensitive to lattice distortions than synchrotron X-ray diffraction measurements,[36] and thus it is well suited to reveal the effects of weak magneto-elastic coupling.

To interpret our results, comparisons were made to density functional theory (DFT) calculations made by our collaborators Turan Birol, Hena Das, and Craig J. Fennie that provide theoretical values for the phonon frequencies and their corresponding eigenvectors and for the magnetic exchange interactions. This comparison allows assignment of spectral features to specific phonons and identification of small lattice distortions that precede magnetic ordering by following the temperature dependence of the Raman spectra. Furthermore, using the magnetic exchange interactions obtained *ab-initio*, we compared the observed magnetic excitation spectrum with theoretical predictions for the magnetic Raman response of distorted triangular-lattice antiferromagnets.[37–39]

Section 3.2 contains technical details associated with our single-crystal synthesis, Raman scattering measurements, and DFT calculations. Section 3.3 discusses the lattice dynamics of α-$SrCr_2O_4$ and contains a comparison of the observed phonon Raman spectra with DFT results. Section 3.4 presents our magnetic Raman scattering results along with *ab-initio* calculations of the nearest-neighbor magnetic exchange interactions in α-$SrCr_2O_4$.

In Chapter 4, we consider another triangular lattice system where deviations from an ideal Heisenberg nearest neighbor model through competing interactions on a triangular lattice lead instead to a suppression of magnetic ordering at low temperatures.

3.2 Experimental methods

Crystals were prepared by Seyed Koohpayeh in collaboration with Tyrel M. McQueen, Siân E. Dutton, and Robert J. Cava using an optical floating zone growth technique. X-ray Laue back reflection was used to orient several of the grown single crystals for Raman scattering measurements. The first set of oriented crystals were cut using a diamond saw and cleaved to obtain flat *bc* plane surfaces (triangular-lattice) of high optical quality. Note that the orthorhombic structure of α-$SrCr_2O_4$ stems from the Sr^{2+} positions and the resulting small displacement of the first Cr^{3+} site away from the higher symmetry position which corresponds to an undistorted triangular-lattice. As a consequence, the *bc* cut contains three distinct orthorhombic domains for which the $\boldsymbol{b}$ and $\boldsymbol{c}$ axes are rotated by ±60° with respect to that of a reference domain which means it was not possible to distinguish $\boldsymbol{b}$ from $\boldsymbol{c}$ during crystal alignment. A second set of oriented crystals were cut to obtain flat *ab* plane and *ac* plane surfaces. Due to the macroscopically indistinguishable $\boldsymbol{b}$ and $\boldsymbol{c}$ axes, these cuts correspond to a mixture of *ab* and *ac* orientations designated by $ab + ac$ in the following.

Raman scattering spectra were measured in micro-Raman and macro-Raman configurations using the Jobin-Yvon T64000 triple monochromator Raman spectrometer discussed in Section 2.7. Micro-Raman spectra of α-$SrCr_2O_4$ were measured for the spectral range from 100 cm^{-1} (12 meV) to 650 cm^{-1} (81 meV) with a resolution of 2 cm^{-1} (0.25 meV). For macro-Raman scattering measurements in the 50 cm^{-1} (2.5 meV) to 650 cm^{-1} (81 meV) spectral range, we used collecting optics coupled with the macro-chamber of the same spectrometer with the diameter of the probe about 50 μm. The 514.5 nm line of a Spectra-Physics Ar^{+}-Kr^{+} laser was used for excitation light.

For low temperature Raman measurements, the crystals were mounted on the sample holder of a Janis ST-300 ^{4}He flow cryostat using silver paint. The temperature of the sample was estimated by comparing intensities of Stokes and anti-Stokes Raman spectra at 300 and 250 K. For micro-Raman measurements 1.0 mW of laser power was used which led to heating of the sample by approximately 20 K. This power was reduced to reach lower temperatures. Macro-Raman measurements used 10 mW of laser power resulting in approximately 10 K of heating. All Raman spectra were corrected for Bose-Einstein temperature effects.

Micro-Raman measurements were done in a backscattering geometry with the electric field vector of the incident light $\boldsymbol{e}_i$ and the electric field vector of the scattered light $\boldsymbol{e}_s$ laying in the bc plane (xx and xy polarizations) for temperatures ranging from 300 to 14 K and with $\boldsymbol{e}_i$ and $\boldsymbol{e}_s$ in the $ab + ac$ plane (zz and $xz + yz$ polarizations) at room temperature. While the bc crystal surface was very high quality, the $ab + ac$ surface was not ideal which reduced the intensity of the corresponding spectra and lead to leakage between the zz and $xz + yz$ polarizations. With the size of structural domains within the bc plane of approximately 25-50 μm in each direction, the micro-Raman measurements with a probe of 2 μm diameter allowed measurements to be performed for a single domain in the bc plane.

To expand on the understanding of the spectroscopic data taken on this compound, comparisons were made to DFT calculations performed by Turan Birol, Hena Das,

Table 3.1: Wyckoff positions and Raman active vibrations for α-SrCr$_2$O$_4$.

Element	Wyckoff Pos.	Raman Representation
Sr1	$2b$	$A_g + B_{2g} + B_{3g}$
Sr2	$2a$	$A_g + B_{2g} + B_{3g}$
Cr1	$4f$	$2A_g + 1B_{1g} + 2B_{2g} + 1B_{3g}$
Cr2	$4c$	Inactive
O1	$4f$	$2A_g + 1B_{1g} + 2B_{2g} + 1B_{3g}$
O2	$4f$	$2A_g + 1B_{1g} + 2B_{2g} + 1B_{3g}$
O3	$8g$	$3A_g + 3B_{1g} + 3B_{2g} + 3B_{3g}$

and Craig J. Fennie using Kohn-Sham DFT implemented in the Vienna Ab-initio Simulation Package. Technical details of their work can be found in Section II. C. of Reference 1.

3.3 Phonon spectrum

3.3.1 Raman active phonons

The orthorhombic structure of α-SrCr$_2$O$_4$ comprises edge-sharing CrO$_6$ octahedra organized in the bc plane of the $Pmmn$ space-group. Magnetic Cr^{3+} ($S = 3/2$) ions form distorted triangular layers (see Figure 3.4) stacked along $\boldsymbol{a}$ and separated by parallel lines of Sr^{2+} cations. A Rietveld refinement of the $T = 100$ K neutron powder diffraction pattern yields two distinct Cr^{3+} sites per unit cell with fractional coordinates $\boldsymbol{r}_1$ (Cr1) and $\boldsymbol{r}_2$ (Cr2) and Wyckoff positions $4c$ and $4f$, respectively.[3] The lattice symmetry appears preserved for temperatures below $T_{\mathrm{N}} \approx 43$ K with $\boldsymbol{r}_1 = (0.5049, 0.25, 0.4975)$ and $\boldsymbol{r}_2 = (0.5, 0.5, 0)$ at $T = 12$ K. The low-temperature structure thus displays four distinct nearest-neighbor Cr–Cr distances varying by less than $\leq 0.5\%$ around the average distance $\bar{d}=2.94$ Å.

Symmetry analysis for the space-group and atomic positions of α-SrCr$_2$O$_4$ yields 36 Raman active modes, given in Table 3.1. Details of the of the polarization selection rules for D_{2h} are given in Appendix A.1, and the Raman tensors are

$$A_g = \begin{pmatrix} a & 0 & 0 \\ 0 & b & 0 \\ 0 & 0 & c \end{pmatrix}, \tag{3.1}$$

$$B_{1g} = \begin{pmatrix} 0 & 0 & 0 \\ 0 & 0 & d \\ 0 & d & 0 \end{pmatrix}, B_{2g} = \begin{pmatrix} 0 & 0 & e \\ 0 & 0 & 0 \\ e & 0 & 0 \end{pmatrix}, B_{3g} = \begin{pmatrix} 0 & f & 0 \\ f & 0 & 0 \\ 0 & 0 & 0 \end{pmatrix}.$$

The room-temperature polarized Raman spectra of α-SrCr$_2$O$_4$ are presented in Figure 3.1. As is typical for transition-metal oxides, modes below 300 cm^{-1} are primarily associated with vibrations of the metal atoms. Phonons in the range from 400 to 650 cm^{-1} involve oxygen vibrations of the CrO$_6$ octahedra. In the measurements done on $ab+ac$ surface we could not separate yz and xz polarizations (B_{1g} and B_{2g} modes).

In Table 3.2, we compare the experimentally observed phonon frequencies with those obtained by DFT calculations. Out of the 36 calculated Raman active modes,

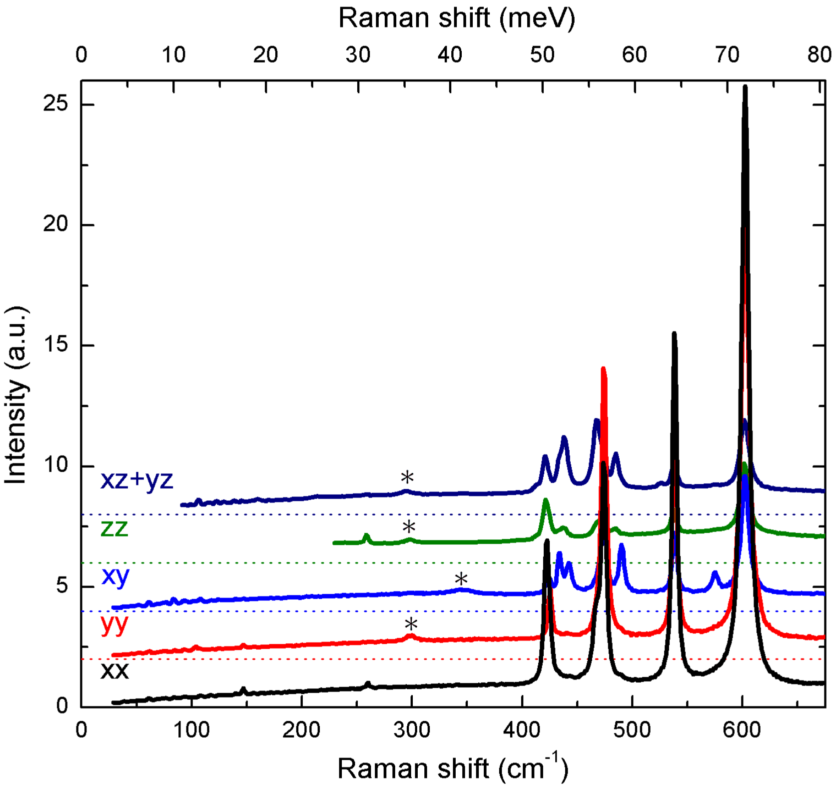

Figure 3.1: Room temperature micro-Raman spectra of α-SrCr$_2$O$_4$ in xx, yy, xy, zz and $xz + yz$ polarizations. Phonons showing strong spin-phonon coupling are indicated by an asterisk ($*$).

28 are experimentally observed. The majority of the missing modes have B_{1g} and B_{2g} symmetry which is explained by the low signal from the $ab+ac$ surface of the crystal. Other discrepancies are likely due to overlap of weak peaks with stronger modes. In particular, many of the oxygen vibrations are close in frequency so there is ambiguity in their assignment. Overall, the calculated phonon frequencies agree remarkably well with the experimentally obtained values. This demonstrates that DFT calculations provide a good description of the lattice dynamics of α-SrCr$_2$O$_4$.

To elucidate potential magneto-elastic coupling, phonon calculations were performed imposing different collinear ferromagnetic and antiferromagnetic spin structures, and the resulting variations in phonon frequencies between these different states was assessed. Our calculations reveal that out of the 36 Raman active modes, four display a frequency shift associated with spin-phonon coupling of 15 cm^{-1} or more, they are marked by $*$ in Tab. 3.2. In our experiments, we observe three of these modes: 295 cm^{-1} B_{2g} (calc. 308 cm^{-1}), 298 cm^{-1} A_g (calc. 310 cm^{-1}), and 346 cm^{-1} B_{3g}. Indeed, these modes are the only modes that show significant changes in frequency and width approaching T_{N}. As discussed in the next section, bands associated with these phonons show full-width at half-maximum (FWHM) of >10 cm^{-1} at 300 K, significantly wider than the thermal-broadening limited FWHM of 4 cm^{-1} found for non-coupled phonons.

Table 3.2: Comparison of measured Raman-active modes with corresponding DFT calculations.[1] The major contributions to the atomic motions are listed in the last column of the table. Calculated modes designated by $*$ showed significant spin-phonon coupling. The temperature dependence of the modes marked with ■, ▼, and ▲ is presented in Figure 3.3.

Experiment			Theory		
ω (cm^{-1})	Pol.	Int.	ω (cm^{-1})	Sym.	Atomic Motions
81	xy	●○○	83	B_{3g}	Sr1(y) + Sr2(y)
102	yy	●○○	100	A_g	Sr1(x) + Sr2(x)
144	xx, yy	●○○	145	A_g	Sr1(x) + Sr2(x)
144	xy	●○○	145	B_{3g}	Sr1(y) + Sr2(y)
163	$xz + yz$	●○○	146	B_{2g}	Sr1(z) + Sr2(z) + Cr1(z)
			221	B_{2g}	Sr1(z) + Sr2(z)
259	xx, zz	●●○	249	A_g	Cr1(z) + O2(z) + O3(y)
			263	B_{2g}	Cr1(z) + O2(xz) + O3(y)
295	$xz + yz$	●○○	$\ast$308	B_{2g}	Cr1(x) + O1(x) + O2(x)
298	yy, zz	●○○	$\ast$310	A_g	Cr1(x) + O1(x) + O2(x)
			$\ast$372	B_{1g}	Cr1(y) + O3(z)
346	xy	●○○	$\ast$373	B_{3g}	Cr1(y) + O3(xz)
413	$xz + yz$	●○○	409	B_{2g}	O1(z) + O3(xz)
421	$xz + yz$	●○○	424	B_{1g}	O3(yz)
422	xx, zz	●●●	413	A_g	O1(z) + O3(xyz)
			426	B_{2g}	O2(xz) + O3(y)
433	xy	●●○	426	B_{3g}	O3(yz)
425	yy	●●●	428	A_g	O2(z) + O3(y)
434	$xz + yz$	●○○	440	B_{1g}	O1(y) + O2(y)
438	$xz + yz$	●●○	453	B_{2g}	O1(x) + O3(xy)
442	xy	●●○	442	B_{3g}	O1(y) + O2(y)
■ 467	xx	●●○	454	A_g	O1(x) + O3(xy)
			462	B_{1g}	O2(y) + O3(x)
			462	B_{3g}	O3(x)
468	$xz + yz$	●●●	463	B_{2g}	O1(z) + O2(xz) + O3(x)
▼ 474	xx, yy	●●●	469	A_g	O1(xz) + O2(xz) + O3(x)
485	$xz + yz$	●●○	473	B_{1g}	O3(xyz)
490	xy	●●○	476	B_{3g}	O3(yz)
527	$xz + yz$	●○○	515	B_{2g}	O1(x) + O2(x) + O3(yz)
▲ 538	xx, yy	●●●	528	A_g	O1(z) + O2(x) + O3(yz)
			569	B_{1g}	O1(y) + O2(y)
575	xy	●○○	571	B_{3g}	O1(y) + O2(y)
			580	A_g	O1(xz) + O2(z) + O3(z)
			583	B_{2g}	O1(xz) + O2(x) + O3(xz)
			592	B_{2g}	O1(z) + O2(xz) + O3(yz)
602	xx, yy	●●●	600	A_g	O1(x) + O2(xz) + O3(x)

3.3.2 Temperature-dependent changes in phonons

An absence of major changes in phonon spectrum of α-SrCr$_2$O$_4$ on cooling down to 15 K is in agreement with the observation of $Pmmn$ space group in the whole studied temperature range by X-ray and neutron powder diffraction.[3] In Figure 3.2, we report the temperature dependence of the α-SrCr$_2$O$_4$ unpolarized Raman spectrum upon cooling from 290 to 15 K. The largest changes with temperature, especially around T_{N}, are expected from the phonons which show magneto-elastic coupling. According to the fits shown in Figure 3.2(c), the 298 cm^{-1} A_g and 346 cm^{-1} B_{3g} phonons show broadening on approaching T_{N}, and the 346 cm^{-1} mode shows a decrease in frequency. Both of the phonons can only be distinguished in the spectra at temperatures above T_{N} while below it they mix with the two-magnon feature centered at 320 cm^{-1}, discussed in further detail in Section 3.4.2.

Along with the changes in the behavior of the phonons coupled to the spin system, we observe changes for some of the phonons which do not show substantial magneto-elastic coupling in the calculations. A dramatic increase in intensity of the 82 cm^{-1} B_{3g} Sr phonon is observed for temperatures below T_N (Figure 3.2 (b)). In addition, some changes are observed for oxygen phonons (see Figure 3.3). A spectral weight redistribution occurs between the 467 and 474 cm^{-1} A_g modes, and a weak change in intensity is also observed for the 538 cm^{-1} A_g phonon. In Figure 3.3(b), we show the temperature dependence of their integral intensities normalized by the 602 cm^{-1} phonon. For temperatures below approximately 90 K, the 467 cm^{-1} peak doubles

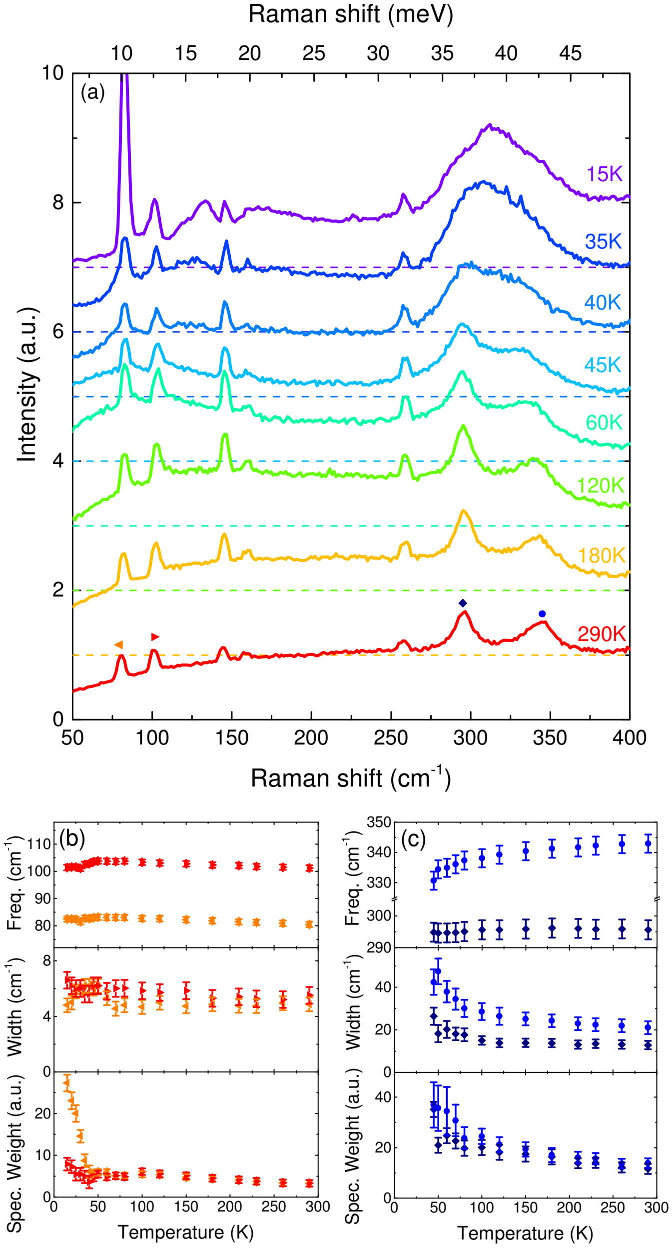

Figure 3.2: (a) Unpolarized Raman spectra of α-SrCr$_2$O$_4$ at selected temperatures between 290 and 15 K below 400 cm^{-1}. Spectra are shifted along y axis for clarity. $y = 0$ is shown for each spectrum by a dashed line. On cooling down from 290 K, the magnetic background starts to increase and forms two wide features which become narrower and shift to higher frequencies below T_{N}. (b) Temperature dependence of the frequency, width, and intensity for the 81 cm^{-1} B_{3g} and 102 cm^{-1} A_g phonons associated with Sr movement; (c) Temperature dependence of phonon frequency, width, and intensity for the 298 cm^{-1} A_g and 346 cm^{-1} B_{3g} phonons which show considerable coupling to the spin system according to the DFT calculations.

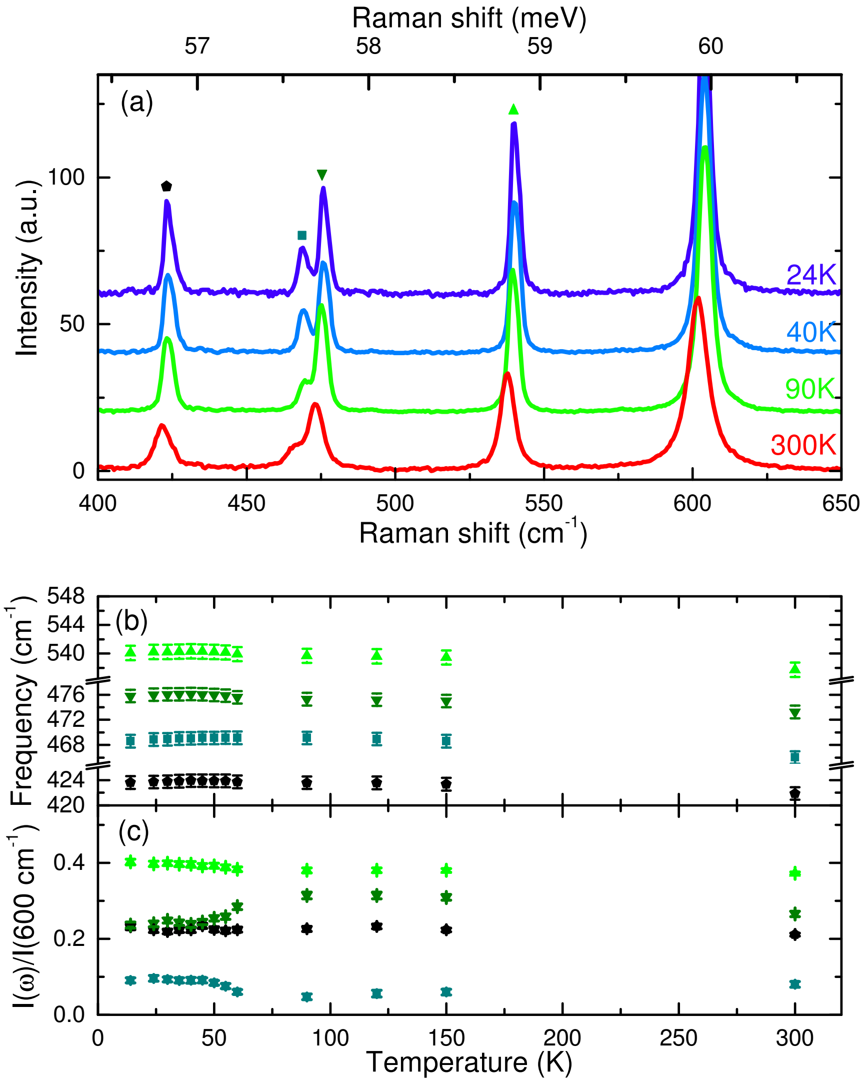

Figure 3.3: (a) Temperature dependence of the Raman spectra of α-SrCr$_2$O$_4$ in xx polarization at frequencies between 400 and 650 cm^{-1}, where oxygen-related phonons are observed. The spectra are shifted along y axis for clarity. (b) Frequencies of selected oxygen-related phonons, see the marking symbols in (a) panel. (c) Integrated intensities of these phonons normalized by the intensity of the 602 cm^{-1} phonon. A redistribution of intensities occurs in the temperature range between 90 and $T_{\mathrm{N}} \approx$ 43 K.

in intensity relative to the 474 cm^{-1} peak with the trend continuing until roughly $T_N \approx 43$ K, below which the relative intensities remain constant. This behavior contrasts with an absence of changes observed for the 422 cm^{-1} phonon, which is plotted for reference in Figure 3.3(b).

The changes in the phonons which are not coupled to the magnetic system could be due to weak variation in the structural parameters with temperature. Indeed, the inter-plane lattice spacing a decreases upon cooling from 300 K before increasing weakly for temperatures below 100 K, and an inflection point is observed in the temperature dependence of all three lattice parameters at the magnetic ordering temperature $T_N \approx 43$ K.[3] Additionally, the weak electrical polarization observed below T_N[13] can influence the phonon intensities.

3.4 Magnetic excitations

3.4.1 Magnetic interactions

To understand the microscopic origin of the magnetic properties of this system, collaborators Turan Birol, Hena Das, and Craig Fennie calculated the magnetic exchange interactions of α-$SrCr_2O_4$ using DFT. Details of their process are given in Reference 1, and results of the exchange interaction energies are given in Table 3.3 with experimental results for α-$CaCr_2O_4$ in Table 3.4.

Although the Cr^{3+} ions form an almost perfect triangular-lattice in terms of their

Table 3.3: Comparison of the experimental and calculated Cr–Cr distances, Cr–O–Cr bond angles, and resulting nearest-neighbor magnetic exchange interactions J_i for α-$SrCr_2O_4$. Theoretical magnetic exchange interactions are from *ab-initio* calculations.[1] Definitions of the J_i's are given in Figure 3.4.

			α-$SrCr_2O_4$				
			Experiment[3] $T = 12$ K		Theory[1]		
	Direct exchange	Super-exchange	Distance (Å)	Bond Angle (°)	Distance (Å)	Bond Angle (°)	J (meV)
J_1	Cr2–Cr2	O1	2.936	94.7	2.936	95.5	4.22
		O2		95.1		96.3	
J_2	Cr1–Cr1	O3	2.938	93.5	2.940	94.2	7.15
		O3		93.5		94.2	
J_3	Cr1–Cr2	O3	2.932	92.4	2.927	92.7	5.70
		O1		95.4		96.0	
J_4	Cr1–Cr2	O3	2.954	94.7	2.959	95.3	3.02
		O2		96.6		97.0	

Table 3.4: Experimental Cr–Cr distances, Cr–O–Cr bond angles, and resulting nearest-neighbor magnetic exchange interactions J_i for α-$SrCr_2O_4$. Bond angles for α-$CaCr_2O_4$ were determined from Reference 2 using neutron powder diffraction measurements for atomic positions and synchrotron X-ray diffraction measurements for lattice parameters.

			α-$CaCr_2O_4$		
			Experiment[2,7] $T \leq 5$ K		
	Direct exchange	Super-exchange	Distance (Å)	Bond Angle (°)	J (meV)
J_1	Cr2–Cr2	O1	2.907	94.5	8.6
		O2		94.7	
J_2	Cr1–Cr1	O3	2.911	92.7	9.1
		O3		92.7	
J_3	Cr1–Cr2	O3	2.889	91.1	11.8
		O1		94.1	
J_4	Cr1–Cr2	O3	2.939	94.1	5.8
		O2		95.9	

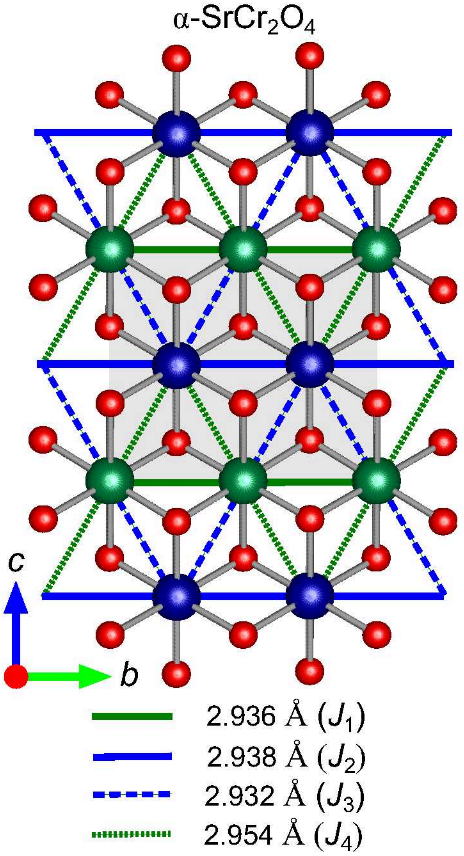

Figure 3.4: The *bc* plane of α-$SrCr_2O_4$ which consists of Cr^{3+} and O^{2-} ions. Blue and green spheres denote the two different Cr^{3+} sites and red spheres denote O^{2-} anions. There are four inequivalent Cr–Cr nearest neighbor distances, leading to the differing magnetic exchange constants J_i marked in the figure. The values shown for the Cr–Cr distances were determined by neutron powder diffraction measurements at 12 K.[3]

spacings, the two inequivalent Cr^{3+} sites lead to four different magnetic exchange interactions, labeled J_1 to J_4 in Figure 3.4. The DFT results indicate very strong variations in the exchange constants, with $\Delta J_i/\bar{J} \geq 25\%$, even though corresponding Cr–Cr distances, vary by less than 0.5%. Both direct cation-cation exchange interactions and superexchange through oxygen contribute to these exchange interactions. It appears that the different Cr–Cr distances cannot alone explain the large differences in exchange constants, and this suggests contributions from Cr–O–Cr superexchange play a role. For example, the value of J_2 is the largest where the Cr–Cr distance is second largest. The corresponding angles in the Cr–O–Cr superexchange paths are close to 90° where superexchange interactions are very sensitive to bond angles. Interestingly, the same tendency of the large differences between J's for a nearly triangular-lattice is observed in α-$CaCr_2O_4$, see the experimental values in the Table 3.4.

3.4.2 Magnetic Raman scattering

In addition to phonons, below 400 cm^{-1} in the low-temperature spectra of α-$SrCr_2O_4$ measured in the *bc* plane (see Figure 3.2) we observe two broad features. At temperatures below T_N, these two broad peaks are centered at ≈ 20 meV (160 cm^{-1}) and ≈ 40 meV (320 cm^{-1}). The 40 meV peak is relatively narrow and asymmetrically skewed towards higher frequencies, while the 20 meV peak is broader and weaker. On increasing the temperature above T_N, both features broaden and shift to lower energies of approximately 12 meV (100 cm^{-1}) and 38 mW (310 cm^{-1}), respectively. These features are shown in greater detail in Figure 3.5 in the spectra with the major phonon features extracted for temperatures below (T=15 K) and above (T=80 K) $T_{\mathrm{N}} \approx 43$ K. The broad and asymmetric lineshape, energy, and temperature dependence of these two bands suggest they originate from two-magnon Raman scattering.

Our experimental results can be compared with theoretical predictions for Raman excitations of triangular-lattice antiferromagnets based on the exchange scattering process[19] which is generally described by the operator $\hat{R} = \boldsymbol{S}_i J_{ij} \boldsymbol{S}_j (\boldsymbol{e}_I \cdot \boldsymbol{\delta}_{ij})(\boldsymbol{e}_S \cdot \boldsymbol{\delta}_{ij})$ where $\boldsymbol{\delta}_{ij}$ is the vector connecting neighboring sites i and j from different magnetic sublattices, $\boldsymbol{e}_i$ and $\boldsymbol{e}_s$ are the electric field vectors of the incident and scattered radiation, $\boldsymbol{S}_i$ and $\boldsymbol{S}_j$ are spin operators for the two different sites, and J_{ij} is the magnetic exchange interaction. A crude estimation of the position of a two-magnon excitation in a collinear antiferromagnet is given by $J(2Sz-1)$, where S is the spin value and z is the coordination number,[40] which yields $17J$ for a $S=3/2$ triangular-lattice. Using the calculated $J_{\mathrm{av}}=5.0$ meV value for α-SrCr$_2$O$_4$, the position of the observed magnetic excitations corresponds to $\approx 4.0J$ and $\approx 8.0J$, much lower than the prediction for a collinear antiferromagnet.

The above discrepancy can be attributed to the non-collinear character of the magnetic order in α-SrCr$_2$O$_4$. Calculations of the Raman response for a triangular-lattice antiferromagnet[37,38] predict a softening of the two-magnon excitations compared to the collinear square-lattice case. These models discuss a simple case of one magnetic

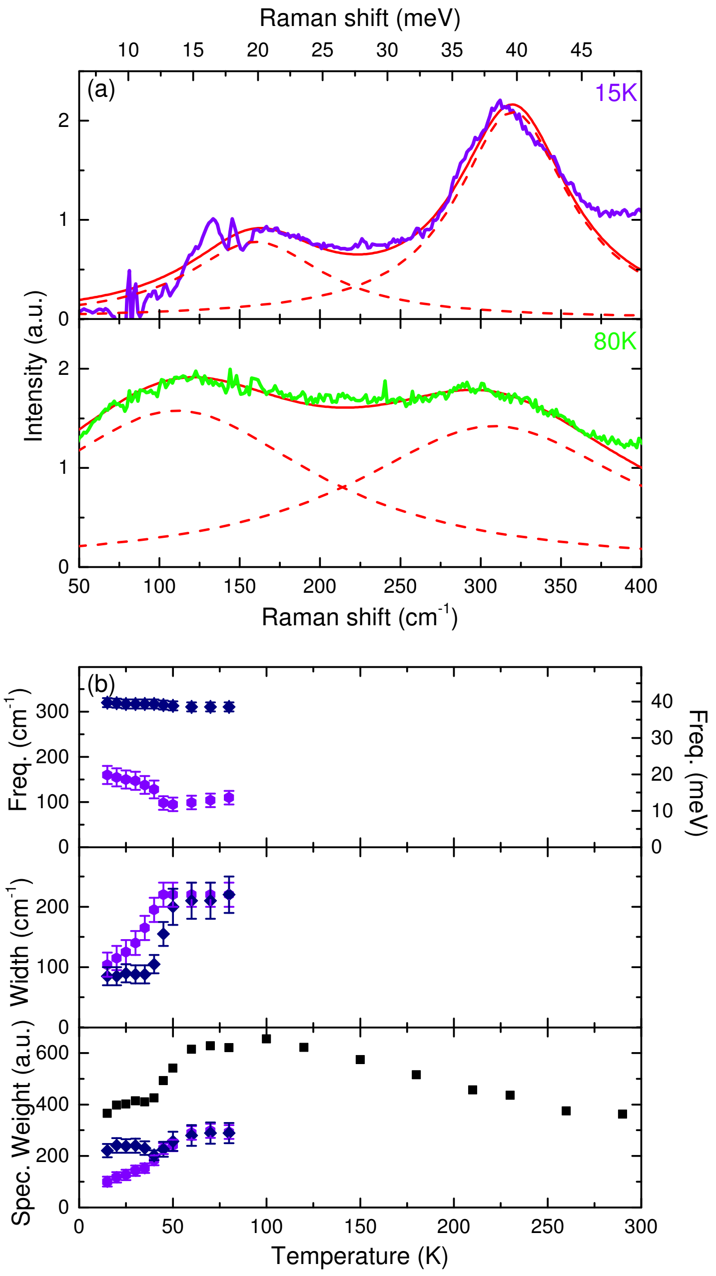

Figure 3.5: (a) Unpolarized Raman spectra of α-SrCr$_2$O$_4$ below T_{N} (15 K, upper panel) and above T_{N} (80K, lower panel) with phonons extracted. Fit of the two-magnon features by Lorentzians (dashed lines) and the resulting fitting curve are shown. (b) Temperature dependence of the positions (upper panel), widths (middle panel), and spectral weights (lower panel) of the maxima of two-magnon excitations received from the fit of the spectra. The parameters are shown by diamonds (40 meW feature) and circles (20 meV feature). In the lower panel (Spectral weight), black squares present the integrated intensity $\int_{50}^{400} I(\omega)d\omega$ of the total magnetic background over the frequency range from 50 and 400 cm^{-1}.

lattice site per unit cell while α-$SrCr_2O_4$ shows two different Cr^{3+} atoms per unit cell. Nevertheless, we consider it suitable to compare our results to these simpler models since the magnetic order observed in α-$SrCr_2O_4$ is non-collinear and incommensurate with the lattice. Two prominent features are expected in the Raman spectra originating from singularities in the two-magnon density of states. Reference 38 calculates how magnetic excitations move to lower frequencies on increasing frustration through a transformation from square to triangular lattice. In the case of a slightly distorted triangular lattice and after rescaling to $S = 3/2$, this results in features centered around $4.5J$ and $6.0J$. In Reference 37, the positions of the magnetic excitations in the isotropic triangular lattice case are $4.5J$ and $7.2J$.

Our experimental results show that in agreement to the theoretical predictions two peaks associated with two-magnon excitations are observed for a triangular antiferromagnet. The experimentally observed energies of the features, approximately 20 meV and 40 meV, or $4.0J_{\mathrm{av}}$ and $8.0J_{\mathrm{av}}$ are close to but do not exactly coincide with the theoretically predicted values. This disagreement can be explained by a simplicity of the theoretical model compared to the structure of α-$SrCr_2O_4$. To the best of our knowledge, magnetic Raman scattering spectra for the particular distortion of the triangular-lattice relevant for α-$SrCr_2O_4$ has not been calculated, and there may be additional effects associated with the anisotropy. In particular, the calculations of Raman spectra for an isotropic triangular lattice in Reference 37 predict that the lower energy feature should have a greater spectral weight. Our results in the ordered state below T_N contrast with that prediction as the high-energy 40 meV excitation is more intense and shows a distinct line shape compared to the weaker and broader 20 meV feature. Contrary to the square-lattice case where magnetic excitations are predicted to only occur in the B_{1g} and B_{2g} polarizations,[41] excitations for a perfect triangular-lattice are predicted to be equally intense in the A_{1g} and B_{1g} channels.[37,38] Unfortunately, the presence of different orthorhombic domains in α-SrCr$_2$O$_4$ prevents us from analyzing the polarization of the magnetic Raman spectra.

We follow the temperature dependence of the magnetic Raman scattering in α-SrCr$_2$O$_4$. To the best of our knowledge, at this point there is no published theoretical description of two-magnon scattering for triangular antiferromagnet at finite temperatures. While the real shape of the Raman spectra is defined by the two-magnon density of states,[37,40] we fit both observed maxima by Lorentzian band shapes to estimate their positions, widths, and intensities (see Figure 3.5 (b)). Even though the positions of the two-magnon excitations in α-SrCr$_2$O$_4$ are much lower than in non-frustrated antiferromagnets, the temperature dependence of the features across T_N is similar to the observations for non-frustrated 3D and 2D materials.[40–44] For both features associated with two-magnon excitations, the line width increases with increasing temperature above T_N, and the features shift to lower frequencies. The spectral weight of the magnetic excitations increases above T_N, also following the tendency observed for collinear non-frustrated 3D antiferromagnets.[40,45] We can follow the two bands as separate features up to $T \approx 100$ K (Figure 3.5(b)). Above

$T \approx 100$ K, the spectral weight of magnetic excitations starts to decrease, and the two basic features widen to form a magnetic background which decreases further on temperature increase, but is present up to room temperature. To illustrate that we plot the spectral weight of the whole magnetic background $\int_{50}^{400} I(\omega)d\omega$ as a function of temperature in Figure 3.5 (b), lower panel (black squares), together with the spectral weight of the two-magnon features received from the fit. The presence of magnetic excitations in 3D collinear antiferromagnets was observed in Raman scattering up to about $4T_{\mathrm{N}}$.[40] For α-SrCr$_2$O$_4$, the persistent 2D magnetic correlations above T_{N} are expected given the estimated $\Theta_{\mathrm{W}} = -596$ K which differs significantly from $T_{\mathrm{N}} \approx 43$ K due to frustration effects.

It is interesting to compare our magnetic Raman scattering results for α-SrCr$_2$O$_4$ to those for α-CaCr$_2$O$_4$.[33] In the latter compound, broad peaks at 5.5, 20, and 32 meV were observed and interpreted as two-magnon excitations. For both compounds the magnetic background increases on cooling the samples from room temperature, however the α-CaCr$_2$O$_4$ compound does not show narrower bands and a decrease of the spectral weight of the magnetic background below T_{N}. The shape of the spectra below T_{N} is different from our results on α-SrCr$_2$O$_4$, while being similar at temperatures above T_{N}. At 10 K in RL polarization the data of Reference 33 shows a broad higher-frequency 33 meV feature with a lower intensity than the low-frequency 5.5 meV peak, in agreement with calculations for the isotropic triangular lattice.[37] As a whole, the energy and line shape of the low-frequency magnetic excitations in α-SrCr$_2$O$_4$ differ more from the theoretical predictions of References 37, 38 than those of α-CaCr$_2$O$_4$. This could be an indication of a more pronounced variation of nearest-neighbor magnetic interactions in α-SrCr$_2$O$_4$, as suggested by Tables 3.3 and 3.4.

3.5 Conclusions

We presented an experimental Raman study of lattice and magnetic excitations in the anisotropic triangular antiferromagnet α-SrCr$_2$O$_4$ and compared them with DFT calculations for the phonon spectra and magnetic exchange constants. The experimental results show agree ment with the calculations and allow us to assign all of the observed modes.

We detected two peaks in the magnetic Raman spectrum at approximately 20 and 40 meV which are resultant from two-magnon excitations. An observation of two peaks is close to that predicted for two-magnon Raman scattering from triangular-lattice Heisenberg antiferromagnets, while their position at approximately $4.0J_{\mathrm{av}}$ and $8.0J_{\mathrm{av}}$ is near the expected theoretical energies. We observe a narrowing and high-frequency shift of the excitation below $T_{\mathrm{N}} \approx 43$ K, and both features are distinguishable up to $\approx$ 80 K. Coupling between magnetic and structural degrees of freedom in α-SrCr$_2$O$_4$ is indicated by a change in the phonons close to the frequencies of the two-magnon feature at 40 meV.

Chapter 4

Effects of disorder in triangular lattice antiferromagnet $NiGa_2S_4$

4.1 Introduction

The antiferromagnetic triangular lattice compound $NiGa_2S_4$ provides another example of a triangular lattice system where deviations from the simple Heisenberg nearest neighbor antiferromagnetic model lead to novel magnetic behavior. We investigate the disorder present in this material that may drive spin freezing or a spin nematic state.

Ni^{2+} atoms are arranged on a 2D isotropic triangular lattice ($S = 1$) with negligibly small magnetic interactions between Ni planes. $NiGa_2S_4$ shows a suppression of long range magnetic order far beyond $\Theta_W = 80$ K[10] down to 0.35 K. Instead the systems develops spin freezing that onsets at 10 K with a correlation length of 26 Å and an incommensurate propagation vector that is approximately $q = (\frac{1}{6}, \frac{1}{6}, 0)$. Heat capacity measurements show two broad features at 10 K and 80 K when the lattice contributions are removed, the lower of which is associated with an onset of spin freezing.[10,14] Reference 14 suggests that magnetic properties of $NiGa_2S_4$ are defined by a competition between ferromagnetic nearest-neighbor superexchange J_1 and antiferromagnetic third nearest-neighbor superexchange J_3, with J_3 being approximately 3 times as strong as J_1.

The near 90° Ni-S-Ni bond angle brings about a weak ferromagnetic nearest neighbor interaction which allows a dominant third nearest neighbor and contributions from a biquadratic term mediated by a coupling of the magnetic interactions with phonons that vary this bond angle. Instead the dominant interaction involves a superexchange through two S atoms to the third nearest neighbor with each bond angle $\sim 120°$.

A simple first and third nearest-neighbor Heisenberg interaction model fails to predict the spin freezing in $NiGa_2S_4$ which has lead to investigations of other effects including biquadratic exchange and disorder on the presence of possible quadrupolar (spin-nematic) ordering.[14,46,47] $NiGa_2S_4$ is proposed to lie near a quantum critical point between antiferromagnetic and quadrupolar ordered ground states sustained by a ferrobiquadratic term in the exchange interaction. Here disorder is found to break long range spiral ordering and introduce a domain structure with a finite correlation length. In an antiferromagnetic quadrupolar ordered ground state an interaction between impurity magnetic moments brought about by the introduction of S vacancies in the superexchange pathways suppresses long range ordering in favor of spin freezing.[46,47]

In this chapter we present the results of our Raman and IR spectroscopy study of $NiGa_2S_4$ single crystals and DFT calculations of phonon modes. Section 4.2 details technical information about the $NiGa_2S_4$ crystals, IR and Raman spectroscopy, and DFT calculations. Section 4.3 shows the experimental spectra that give evidence for disorder. In Section 4.4 we discuss the observed disorder in relation to the unusual magnetic properties of $NiGa_2S_4$.

4.2 Experiment and theoretical methods

The single crystals of $NiGa_2S_4$ were grown by Tomoya Higo and Satoru Nakatsuji using the method outlined in Reference 48. The resulting crystals are thin plates with the most developed surface parallel to ab plane measuring up to 3 by 3 mm and the thickness 10 μm.

A Bruker Fourier transform infrared (FTIR) spectrometer with a bolometer detector was used to obtain the reflection infrared spectrum across an energy range of 150 to 600 $\text{cm}^{-1}$with a resolution of 2 cm^{-1}. Spectra were measured in polarizations with polarization of light $E \parallel (ab)$, where only modes with E_u symmetry are observed. The absolute reflectance values were received by referencing the sample spectra to that of a sample with a gold film evaporated on its surface. Absorbance spectra were received from reflectance using Kramers-Kronig transformation, with a constant high-frequency extrapolation. For measurements from 4 to 300 K a Janis cold finger cryostat was used.

The macro and micro Raman setups discussed in Section 2.7 were used for inelastic light scattering measurements. Macro-Raman scattering measurements were performed over a frequency range of 10 to 600 cm^{-1} with resolution 5 cm^{-1} using a Jobin-Yvon U1000 spectrometer in a pseudo-Brewster's angle scattering geometry. The 488 nm and 514 nm lines of an Ar^+ laser were used as excitation light with a beamsize on the sample of $\sim 50 \times 100$ μm. Micro-Raman measurements over a frequency range of 70 to 600 cm^{-1} with resolution 2 cm^{-1} used a Jobin-Yvon T64000 Raman spectrometer in a backscattering geometry.

The crystals are thin plates. Thus we were able to use both micro and macro setups for measuring spectra in the ab plane, while spectra in zz polarization are only available from micro setup.

The $NiGa_2S_4$ structure trigonal $P\bar{3}m1$ space group corresponds to the D_{3d} point group symmetry with the following Raman tensors:

$$A_{1g} = \begin{pmatrix} a & 0 & 0 \\ 0 & a & 0 \\ 0 & 0 & b \end{pmatrix}$$

$$E_g = \begin{pmatrix} c & 0 & 0 \\ 0 & c & d \\ 0 & d & 0 \end{pmatrix}, \begin{pmatrix} 0 & -c & -d \\ -c & 0 & 0 \\ -d & 0 & 0 \end{pmatrix}.$$

Based on these Raman tensors, the intensities for the different measured polarizations can be decomposed as

$$\begin{aligned} I_{xx} &= |a|^2 + |c|^2 \\ I_{xy} &= |c|^2 \\ I_{RR} &= 2|c|^2 \\ I_{RL} &= |a|^2 \\ I_{zz} &= |b|^2 \end{aligned}$$

Where z polarized light is along the out of plane c axis and R and L polarizations correspond to right $(x - iy)$ and left $(x + iy)$ circularly polarized light, respectively. Discrepancies between the theoretical and the observed polarization dependence can be attributed to the depolarization that occurs at the crystal surface in all non-backscattering geometries. The pseudo-Brewster's angle scattering geometry used for the macro-Raman measurements results in a partially linearly polarized incident light in the RR and RL with intensity $I_{xR}, I_{xL} = \frac{|a|^2}{2} + |c|^2$, as well as a small contribution from z polarized incident light.

Density functional theory calculations of phonon modes were carried out using Quantum Espresso with the PHonon package[49] based on x-ray diffraction measurements.[48] A generalized gradient approximation was used for the exchange-correlation in the energy functional.

4.3 Results

4.3.1 Room temperature phonons

$NiGa_2S_4$ belongs to the trigonal $P\bar{3}m1$ space group with D_{3d} point group symmetry. A triangular lattice of Ni^{2+} ($S = 1$) magnetic ions is formed in the ab plane from edge-sharing NiS_6 octahedra (Figure 4.1). Additional layers of corner sharing GaS_4 tetrahedra in another non-magnetic triangular lattice are positioned above and below the Ni lattice giving rise to two unique S positions: S2 neighboring both Ni and Ga and S1 just neighboring Ga.[50] These $NiGa_2S_4$ sheets are stacked along the c direction with only van der Waals interactions between layers giving a highly two-dimensional structure.

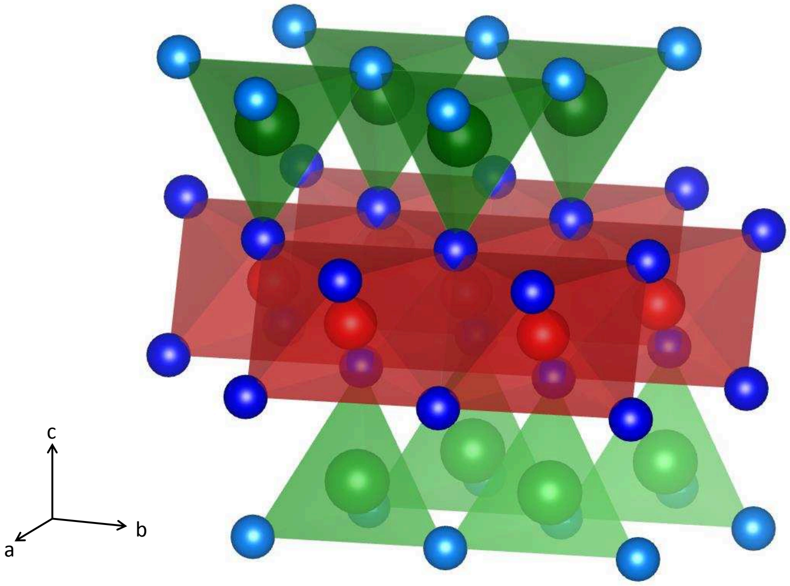

Figure 4.1: $NiGa_2S_4$ structure showing the red edge sharing NiS_6 octahedra which make a triangular lattice of Ni^{2+} surrounded above and below by green GaS_4 tetrahedra layers. Successive sheets are stacked along the c direction with only van der Waals forces.

Table 4.1: Wyckoff positions and Γ-point representations for $NiGa_2S_4$.

Element	Wyckoff position	Γ representation
Ni	1b	$A_{2u} + E_u$
Ga	2d	$A_{1g} + E_g + A_{2u} + E_u$
S1	2d	$A_{1g} + E_g + A_{2u} + E_u$
S2	2d	$A_{1g} + E_g + A_{2u} + E_u$

The four unique atomic positions in the unit cell give rise to 6 Raman and 6 IR-active optical modes with representations given in Table 4.1 which also accounts for the $A_{2u} + E_u$ acoustic modes. The Ni ions lie at centers of inversion symmetry and are thus Raman inactive, otherwise all other ions contribute in part to all modes. Table 4.2 lists the frequencies and widths of all of the first-order Raman active phonons and frequencies predicted by DFT calculations, which coincide well with experimental results.

Nuclear quadrupole resonance measurements give evidence for two Ga sites[51] though the perfect crystal structure seen in diffraction should have only a single position. An electron diffraction study[48] confirmed the Ni^{2+} layer to be an undistorted triangular lattice. Transmission electron microscopy images show that instead the two Ga sites likely result from stacking faults that are observed along the c direction. Doping of nonmagnetic Zn^{2+} ions at the Ni^{2+} sites increases the spin freezing temperature contrary to the behavior of other spin-glass materials.[52]

Figure 4.2 shows the 300 K Raman spectrum of $NiGa_2S_4$ over a frequency range of 10 to 550 cm^{-1} for all polarizations within the ab plane and 70 to 550 cm^{-1} for the cc (or zz) polarization. The 5 narrow features observed in these spectra correspond to

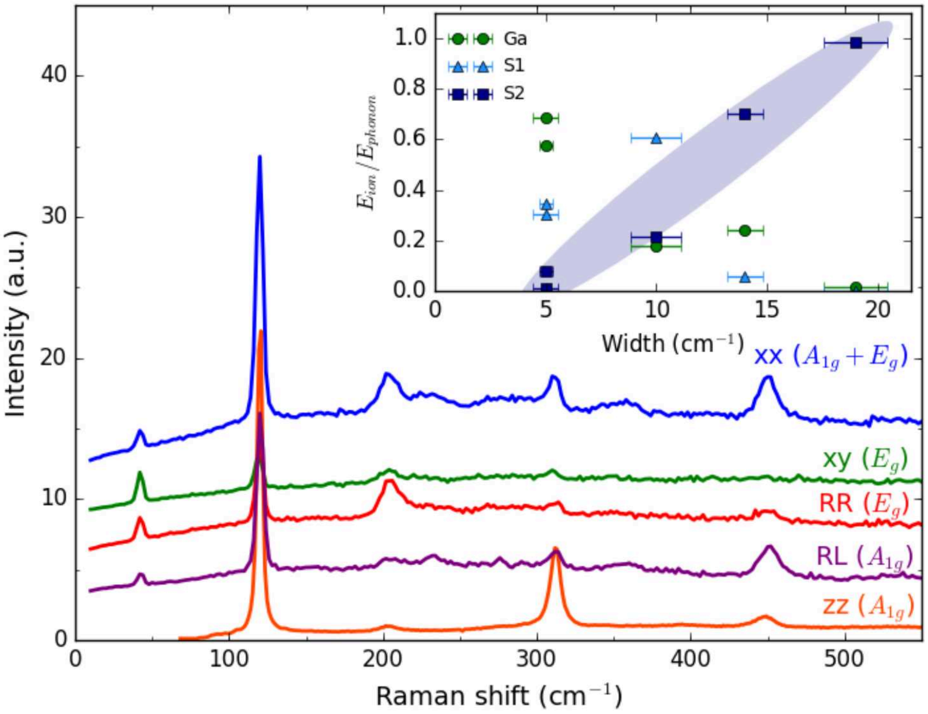

Figure 4.2: Room temperature Raman spectra $NiGa_2S_4$. Polarizations within the ab plane measured using macro-Raman. zz polarization measured using micro-Raman setup. Inset shows energy contributions of each Raman-active atomic site compared to experimental phonon widths. Energy contributions are estimated as a percentage of the total energy which has proportionality $E \sim mx^2\omega^2$ where displacements are taken from DFT phonon eigenvectors. A correlation between the S2 energy and the phonon width is seen. Figure 4.1 for atomic positions.

first-order Raman active phonons. The frequencies and symmetry assignment based on polarization dependence are presented in Table 4.2, with eigenvectors shown in Figure 4.4. Another E_g mode expected according to DFT calculations at 285 cm^{-1} is not observed which likely results from the fact that the χ_{xz}, χ_{yz} (d in the above Raman tensors) was not measured. The widths of the phonons vary in the range from 5 cm^{-1} which is a typical value for the phonons in a crystal to 20 cm^{-1}. The phonons at 204 and 450 cm^{-1} show the largest width (see Table 4.2).

In addition to the clearly observed, symmetry-allowed phonons a number of weak and broad bands appear in the background spectrum centered at approximately 233, 276, and 357 $cm^{-1}$and occuring in both xx and xy polarizations. Their broad shapes suggest they may result from defect-induced scattering of phonons which reflects a weighted density of states of the phonon dispersions.

Of three IR-active E_u modes expected in the reflectance and absorption measured with polarization of the incident light E lying in ab plane, we observe two at 271 and 298 cm^{-1} (Figure 4.3 (b)) in agreement with previous infrared measurements on powder.[50] The third mode is estimated from DFT calculations to have an energy of 62 cm^{-1}, below the lower energy threshold for this experiment.

In addition to these two prominent bands, there are several minor peaks in the spectrum at 316, 334, and 356 cm^{-1}. The band at 271 cm^{-1} shows a lower-frequency wing which also can evidence for an additional band. Previous infrared measurements on powder $NiGa_2S_4$ samples[50] show these two features at 273 and 301 cm^{-1} with a

Table 4.2: Measured frequencies ω and widths γ for the Raman and IR active modes and the polarizations in which they appear. These frequencies are compared with those determined from calculations, and the relative displacements of each of the unique atomic positions is shown.

	Raman			IR		DFT				
Sym	ω	γ	Pol.	ω	Pol.	ω	Ni	Ga	S1	S2
A_{2u}						9	0.38	0.38	0.38	0.38
E_u						18	0.38	0.38	0.38	0.38
E_g	42	5	xx, xy, RR			40	0.00	0.50	0.49	0.10
E_u						62	0.54	0.30	0.28	0.44
A_{1g}	120	5	xx, RL			118	0.00	0.44	0.50	0.24
A_{2u}						123	0.86	0.19	0.30	0.07
E_g	204	19	xx, RR			198	0.00	0.06	0.00	0.70
E_u				271	x, y	261	0.54	0.11	0.16	0.56
A_{2u}						280	0.12	0.08	0.52	0.46
E_g						284	0.00	0.28	0.65	0.05
E_u				298	x, y	284	0.14	0.27	0.62	0.17
A_{1g}	313	10	xx, RL			316	0.00	0.21	0.57	0.34
A_{2u}				*427*[50]	unpol.	354	0.03	0.37	0.33	0.50
A_{1g}	450	14	xx, RL			408	0.00	0.25	0.18	0.63

weaker but still clearly distinct feature also occurring at 427 cm^{-1}. The absence of the 427 cm^{-1} peak in the ab-plane oriented single crystal spectrum of the current study indicates that it must correspond to an A_{2u} (z polarized light) mode which would be observed in a powder averaged sample.

The presence of these additional modes are possibly further indication of disorder resulting in off Γ-point defect scattering.

4.3.2 Low temperature Spectra

On cooling the samples to 5 K, the bands in IR spectra show thermal narrowing and shift to the high frequencies. The "extra" features become more distinct, especially the band at 264 cm^{-1}.

In the Raman spectra from 300 to 15 K additional features with widths of approximately 20 cm^{-1} appear at 264, 296, 346, and 427 cm^{-1} (see Figure 4.3). The appearance of these features onsets at temperatures around 300 K and continue to develop with a near linear increase in intensity down to 40 K. These peaks arise from phonon scattering which is consistent with the widths of 20 cm^{-1}, similar to other Raman allowed disordered phonons.

Figure 4.3 compares the 40 K Raman spectra with the 4 K IR absorbance suggests the likely origin of these peaks as IR-active phonons which become Raman-active due to local symmetry breaking. Here the four additional features that appear in the Raman spectrum (271, 298, 346, and 427 cm^{-1}) are marked in with red dashed lines. The 271, 298, and 427 cm^{-1} modes clearly correlate with features seen in the IR spectrum. The fourth peak that appears in the Raman spectrum at 346 cm^{-1} does not correspond as clearly to distinct features in the IR spectrum though there are small features at 335 and 356 cm^{-1} in IR spectra.

The reverse process of Raman modes becoming IR active would also be expected. However, of the modes found in the measured in IR frequency range, the 313 cm^{-1} mode could be hidden by the very strong absorption at 299 cm^{-1} and the mode at

450 cm^{-1} is in a region with significant interference.

4.4 Discussion

A comparison of the Raman phonon spectra and DFT calculations can provide a more detailed understanding of disorder found in the samples. The energy contribution that each atom with mass m makes to the total energy of a vibration of frequency ω is $E \sim mx^2\omega^2$, where x is the displacement of this atom. This means that a disorder located at a particular atomic site can be expected to have a much greater impact on phonons that involve significant displacement of that site. The eigenvectors which give the relative displacements have been calculated using DFT.

Figure 4.2 shows a comparison of the experimentally measured Raman phonon widths with the contributions to the total energy by each of the crystallographically independent atoms displayed as a percentage of the total energy of the phonon. The modes with a greater contribution of S2 energy found at 204 cm^{-1} E_g and 450 cm^{-1} A_{1g} (denoted by ▲) (see Figure 4.4 and Table 4.2) show a large width of the experimentally observed phonons. Conversely, modes that involve significant motion of the Ga and S1 sites are comparatively narrow.

We conclude from the correlation between the energy associated with S2 motion and the experimental width of the phonon that the disorder arises primarily from S2 sites, which make up the NiS_6 octahedra of the triangular lattice. This is especially

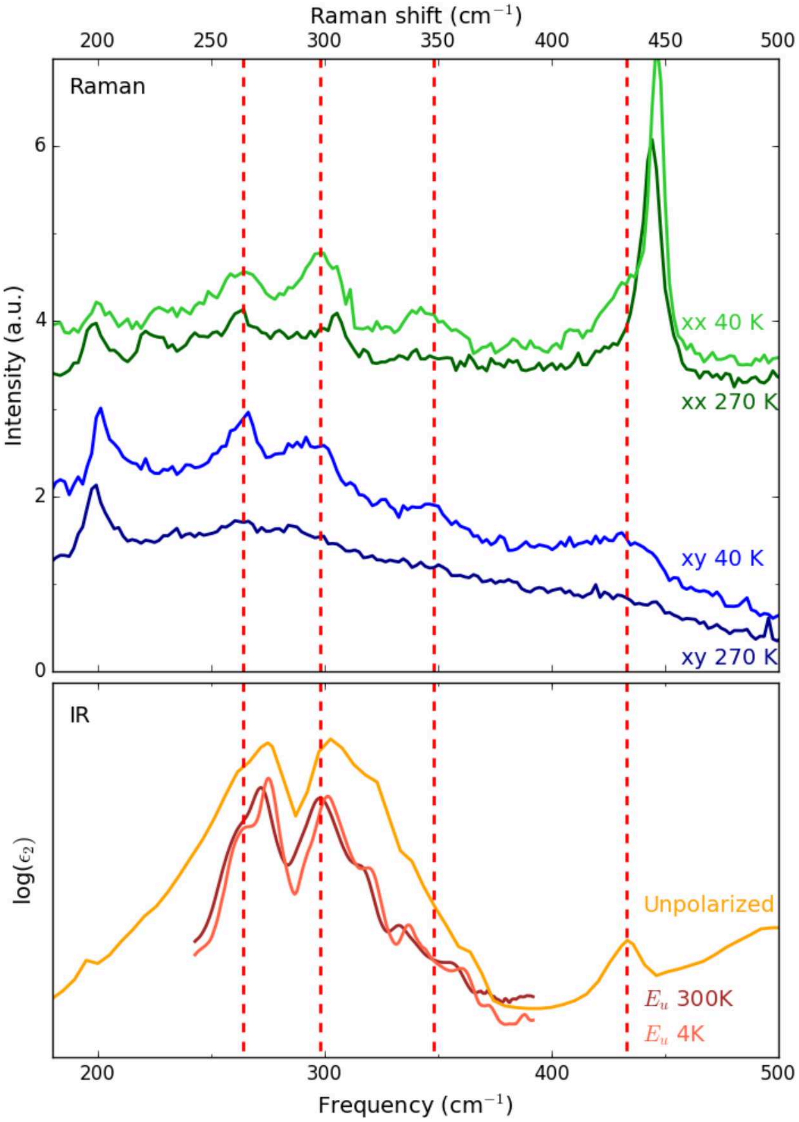

Figure 4.3: Comparison of (a) 40 K and 270 K Raman spectra with (b) 4 K IR spectra. The Raman spectra show 4 additional peaks that appear on cooling both xx and xy polarizations. Frequencies of these new peaks coincide with those present in IR spectra.

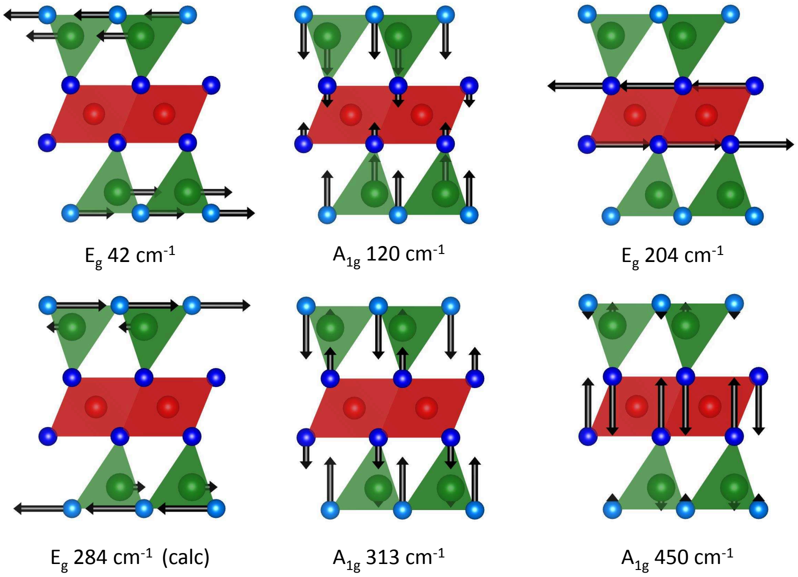

E_g 42 cm^{-1} A_{1g} 120 cm^{-1} E_g 204 cm^{-1}

E_g 284 cm^{-1} (calc) A_{1g} 313 cm^{-1} A_{1g} 450 cm^{-1}

Figure 4.4: Displacement of atoms for Raman-active vibrations of $NiGa_2S_4$ calculated by DFT.

relevant to the low temperature spin freezing in $NiGa_2S_4$ due to the importance of superexchange through the S2 site for the exchange interactions. Fits of neutron scattering data and magnetization measurements suggest an AFM third-nearest-neighbor interaction $J_3 = 2.8$ meV and a FM nearest-neighbor interaction $J_1 = 1.0$ meV.[10, 14] The appearance of a significantly stronger J_3 is indication of the importance of superexchange in defining the interactions. A weak FM is expected for interactions between ions with nearly a 90° bond angle.

The presence of disorder at S2 sites which make up the octahedra surrounding the magnetic ions can thus be expected to have a significant effect on the interaction between third nearest neighbor sites which are responsible for the geometric frustration. Anisotropy in the magnetic exchange constants has been shown to lead to a spin disordered state.[47,53]

The Raman-active phonons show a typical narrowing and hardening on cooling except for the 204 cm^{-1} E_g mode which develops an asymmetric Fano lineshape given by the function

$$F(\omega, \omega_F, \Gamma_F, q) = \frac{1}{\Gamma_F q^2} \frac{(q + \alpha(\omega))^2}{1 + \alpha(\omega)^2} \tag{4.1}$$

$$\alpha(\omega) = \frac{\omega - \omega_F}{\Gamma_F} \tag{4.2}$$

The modes involving significant motion of the S2 sulfur position are of particular importance for their effect on the interaction Hamiltonian, and the frequencies and widths for these phonons are given in Figure 4.5(a) and (b). The 204 cm^{-1} involves inplane motion of the S2 positions, the 450 cm^{-1} involves out of plane motion. The 450 cm^{-1} phonon width is well fit by the temperature dependence of mode thermally broadened by the decay into two phonon modes with half the energy, given by

$$\Gamma(T, \omega) = \Gamma_0 + A\left[2n\left(\omega/2\right) + 1\right] \tag{4.3}$$

Γ is the linewidth with Γ_0 is defined by disorder in this system. A is treated as a constant that gives the transition matrix element of the decay from the initial one phonon state into a two phonon state. $n(\omega/2)$ is the Bose-Einstein thermal factor for

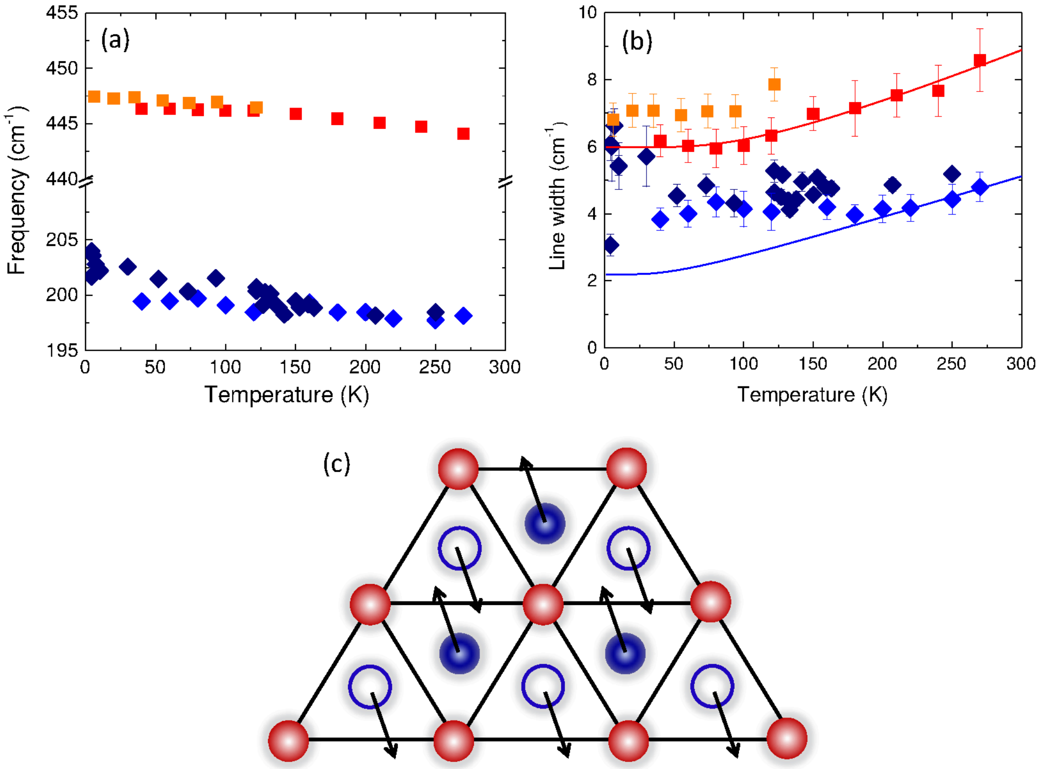

Figure 4.5: (a) Temperature dependence of (a) frequencies and (b) widths of phonons which involve significant S2 movement. 450 cm^{-1} A_{1g} phonon fit parameters are marked in black and 204 cm^{-1} E_g in red. Fit curves give the temperature dependence expected for thermal broadening of a mode by nonradiative decay. (c) Eigenvector of the inplane motion of the E_g mode which shows coupling with possible nematic order.

half the energy of the phonon. The 204 cm^{-1} mode by contrast deviates from this behavior at temperatures below 150 K.

The Fano lineshape of the 204 cm^{-1} demonstrates an interaction between this phonon and a background continuum. Since this mode alters the nearest neighbor Ni-S-Ni superexchange bond angle it may cause a modulation that leads to a biquadratic exchange in the Hamiltonian driving a spin nematic state.

The inversion symmetry of the D_{3d} crystal point group restricts the appearance of the vibrational modes to only the Raman or IR spectrum. An appearance of IR modes in the Raman spectrum is indication of a breaking of this inversion symmetry. No structural phase transition has been observed previously in low temperature diffraction measurements[10] thus this distortion is likely caused by local symmetry breaking from defects. It should be noted that as the crystal symmetry changes to allow IR modes in the Raman spectrum there is no group theoretical restriction on the relative intensities of the modes, and thus weak IR modes may become intense in particular polarizations of the Raman spectrum.

4.5 Conclusion

In this chapter we have demonstrated new evidence for disorder in $NiGa_2S_4$ present both at 300 K and further enhanced as a breaking of symmetry on cooling. By analyzing the phonon eigenvectors we have found the 300 K Raman phonon width to be roughly proportional to the energy associated with the S2 sulfur position, part of the NiS_6 octahedra, which indicates the sulfur vacancies appear primarily at these locations. These ions are responsible for the superexchange pathways of the Ni-Ni magnetic interactions and likely provide the necessary disorder to suppress a long range quadrupolar ordered state. Along with this signature for S2 vacancies, broken inversion symmetry which may arise from a local ordering of sulfur vacancies appears at temperatures below 300 K. The loss of inversion symmetry may be critical to an understanding of the spin dynamics of $NiGa_2S_4$ by allowing for a DM term in the exchange interaction.

Chapter 5

Breakdown of the Kondo insulating state in samarium hexaboride by introducing Samarium vacancies

5.1 Introduction

In this chapter, we detail work on probing the Kondo insulating state in SmB_6 and understanding the effects that sample quality can have on its electronic properties. By assigning a mode in the Raman spectrum to scattering from crystal defects, we identify a sensitive means for quantifying Sm vacancies and track the closing of the bulk hybridization gap with as few as 1% vacancies.

Much recent research is aimed at experimental realization of the topological insulator (TI) state of matter where topologically protected metallic surface states appear due to a surface crossing of inverted bands of opposite parity in the bulk. While the TI state has already been observed in band insulators, it is proposed that the strong electronic interactions in Kondo insulators could also be a source of topologically invariant surface states.[17, 54, 55] SmB_6, which has been studied extensively for its mixed valence and Kondo insulating properties,[56, 57] is the prime candidate for the first topological Kondo insulator (TKI). A plateau in the DC resistivity of SmB_6 below 5 K results primarily from a presence of metallic surface states as indicated by geometry dependent transport studies.[58–60] Interpretation of these metallic surface states varies from topologically protected[58, 60] to polarity-driven surface states.[61]

One of the requirement for a TI state is an inversion of electronic bands of opposite parity which form the respective insulating gap. In SmB_6, a gap opens at the Fermi level due to hybridization between $4f$ and $5d$ electronic bands below 70 K (below 150 K according to Reference 62). Optical measurements suggest a gap of 16-19 meV with an impurity band at 3-5 meV,[63–66] photoemission at 18 meV,[62] point-contact spectroscopy at 21 meV with an in-gap band at 4.5 meV below the conduction band,[67, 68] and DC resistivity estimates the activation energy at 3.5 meV.[58] Band structure calculations predict a gap opening due to hybridization with band inversion necessary for topological nontriviality at the X-point in the Brillouin zone (BZ).[69, 70] A neutron scattering study[71] gives evidence of band inversion at X and R points of the BZ.

CHAPTER 5. BREAKDOWN OF THE KONDO INSULATING STATE IN SAMARIUM HEXABORIDE BY INTRODUCING SAMARIUM VACANCIES

Though a number of these studies present results suggestive of TKI behavior some inconsistencies exist. Both 2D quantum oscillations in Al flux grown SmB_6 samples[72] and 3D in floating zone SmB_6 samples[73] have been observed raising the question of how signatures of a Fermi surface can occur in an insulating bulk. Additionally, discrepancies can be found in the degree of resistivity plateauing found in across a range of samples with a greater tendency for plateauing in Al flux grown than floating zone grown samples.[74] While to some degree the plateauing and ratio of room temperature resistivity to low temperature resistivity can be tuned by sample geometry, this trend still generally holds true. Our aim is to understand the source of the discrepancy in these behaviors.

Here we use Raman spectroscopy to look at floating zone samples known to have vacancies at Sm sites in relation to an Al flux sample found to be stoichometrically pure. Sm vacancies are known to increase along the length of a floating zone crystal which provides a gradient for looking at their effect on the opening of the hybridization gap. Raman spectroscopy probes bulk electronic structure through measuring intra- and inter-band excitations.[41,75] Low frequency Raman scattering measurements already proved useful in studies of the hybridization gap and in-gap states for Al-flux grown SmB_6 samples.[76,77] We present a wide energy range Raman study of SmB_6 samples with a variation in number of Sm vacancies which allows us to get detailed information on the phonon and electronic Raman spectrum of these samples.

5.2 Experiment

5.2.1 Crystal growth

In this study we used single crystals of SmB_6 grown by both Al flux and floating zone (FZ) techniques. FZ single crystals of SmB_6 were grown using the optical floating zone technique[59,74] by Seyed Koohpayeh, W. Adam Phelan, and Tyrel McQueen and are representative of "typical" SmB_6 crystals described in these papers. An increasing presence of Sm vacancies along the length of a single FZ crystal occurs due to vaporization of the stoichiometric rod materials into a Sm rich mixture and can be characterized by a systematic decrease in lattice parameters. For our study we used two samples cut from the most stoichiometric (FZ SmB_6-Pure) and most Sm deficient (FZ SmB_6-Def) end of the rod. Based on powder diffraction measurements of the lattice parameters in comparison to previous results for non-stoichiometric SmB_6, we estimate the highest concentration of vacancies as 1% in FZ SmB_6-Def.[74] Magnetization measurements for the two FZ-grown samples did not show a significant difference in average magnetic moment which could arise from larger differences in the number of Sm-vacancies.[78]

The Al flux crystals were grown by Priscila F. S. Rosa and Zachary Fisk at University of California, Davis. We selected an Al flux grown crystal, referred to as Al Flux-SmB_6, which was found from Raman measurements to have the fewest crystallographic imperfections and comparable linewidths of boron Raman active phonons for FZ samples. A value of the linewidth of boron phonons as a parameter to characterize the quality of SmB_6 samples and the degree of structural variation within Al flux grown samples is discussed in Appendix C.

Phonon Raman scattering is known to be one of the primary methods to characterize structure and structural imperfections of solids.

5.2.2 Raman measurements

Raman measurements were performed using both the micro- and macro-Raman setups of the Horiba Jobin-Yvon T64000 triple monochromator spectrometer. Penetration depth of the light at 514 nm in these metallic samples is estimated to be of the order of 100 nm. The measurements were performed on cleaved surfaces that were exposed to atmosphere. No Raman evidence of samarium oxide which typically appears on the surface of the samples exposed to air was detected in the measured Raman spectra.

Measurements were performed over a temperature range of 10 to 300 K using a Janis ST-500 cold finger cryostat with samples affixed to the cold finger using silver paint. Laser heating was estimated to be 10 K at 10 mW, and the power was reduced to reach the lowest temperatures. Temperatures listed reflect this heating and all spectra were corrected by the Bose-Einstein thermal factor. To compare the results for different samples the spectra were normalized on the intensity of the 158 meV A_{1g} phonon to compensate for the small differences in intensity due to the variation in

Table 5.1: Polarizations of the measured Raman scattering spectra of SmB_6, the geometry of the measurements, and the probed irreducible representations for each polarization.

Polarization	e_i, e_s geometry	Symmetry (O_h)
(x,x)	$c(aa)\bar{c}$	$A_{1g}+E_g$
(x,y)	$c(ab)\bar{c}$	T_{2g}
(x',x')	$c(a+b,a+b)\bar{c}$	$A_{1g}+\frac{1}{4}E_g+T_{2g}$
(x',y')	$c(a+b,a-b)\bar{c}$	$\frac{3}{4}E_g$

the quality of the cleaved surfaces.

SmB_6 has $Pm\bar{3}m$ cubic symmetry corresponding to O_h point group symmetry, details of the O_h point group in Appendix A.2. The crystals were oriented using X-ray diffraction and polarization-dependent Raman scattering measurements. The temperature dependent measurements were performed in the (100) plane with the orientations of the electrical field of the incident light e_i and electrical vector of the scattered light e_s listed in Table 5.1. The large acceptance angle of the analyzing optics results in some additional signal from other polarizations. In the table we also present the irreducible representations of the O_h point group probed in these polarizations.

5.3 Results

The Raman spectra of SmB_6 consist of relatively narrow phonon peaks superimposed on the electronic background. In Section 5.3.1, we discuss how previously unidentified defect-induced phonon scattering can be used to extract the information on Sm vacancies in the studied samples of SmB_6. In Section 5.3.2, the electronic Raman response for samples with different amounts of Sm vacancies is discussed.

5.3.1 Phonons

Frequencies of vibrations are proportional to $\frac{1}{\sqrt{m}}$ of the atoms involved, thus the phonon response of vibrations involving exclusively the B_6 will occur at higher frequencies than those that also involve Sm motion.

In the SmB_6 Raman spectra the three symmetry allowed Γ-point phonons seen as the intense, relatively narrow features (Figure 5.1) are the T_{2g} phonon at 89.6 meV (723 cm^{-1}), E_g at 141.7 meV (1143 cm^{-1}), and A_{1g} at 158.3 meV (1277 cm^{-1}) only involve motion of the atoms within the B_6 octahedra.[4] They are observed in polarizations corresponding to their symmetries and are well-known from previous vibrational Raman studies of SmB_6 crystals.[4,76,77,79,80] The relatively large widths of the phonons of 2-4 meV emphasizes the role of valence fluctuations and disorder.[81] While some variations existed in the B_6 phonons of the Al flux compounds, Al Flux-SmB_6which was chosen for this study matched the FZ samples in width and frequency of these phonons suggesting that any differences in crystal structure arise from the Sm atom.

At 10 and 21 meV (see Figure 5.1), which is far below the vibrational response of B_6 octahedra, we observe two features with largest intensity in (x, x) polarization. In the unit cell of SmB_6 $Pm\bar{3}m$ symmetry, the Sm ion is located at a center of inversion symmetry, and thus there are no Raman-allowed Γ-point phonons associated with Sm

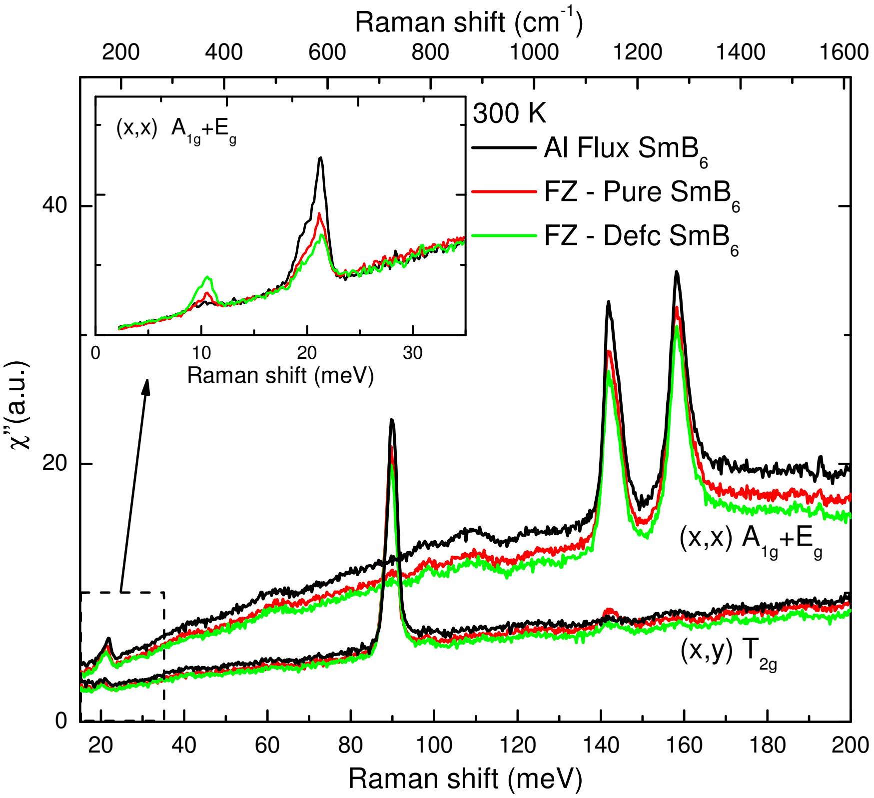

Figure 5.1: Room temperature Raman spectra of the three studied SmB_6 samples with increasing number of Sm vacancies (Al Flux-SmB_6, FZ SmB_6-Pure, FZ SmB_6-Def) in (x, x) and (x, y) polarizations. The 3 first-order Raman active phonons appear at 89.6 meV (T_{2g}), 141.7 meV (E_g), and 158.3 meV (A_{1g}) are superimposed on a broad continuum of electronic scattering. Inset shows low-frequency (x, x) spectra of the samples. Two symmetry forbidden peaks appear at 10 meV and 21 meV correspond to defect-induced and two-phonon scattering, respectively.

movement, and only one optically active phonon.

We attribute the 10 meV feature to acoustic phonons associated with collective unit cell movement, which become Raman active due to local symmetry breaking induced by the presence of Sm defects. The loss of translational invariance allows light scattering from all points within the BZ,[81] leading to the Raman intensity with a weighted proportionality to the phonon density of states (DOS). The basis for our assignment are the data from neutron scattering experiments,[5] which show the relevant acoustic phonons with energies around 10 meV and a flat dispersion over the latter half of the BZ. The flat dispersion of this phonon is responsible for the relatively small line width of the Raman feature. The only other phonon which would be affected by disorder on Sm sites is an optical T_{1u} phonon which involves motion of Sm atoms and B_6 octahedra against each other has a steep dispersion[5,82] with a broad, flat DOS over the large energy range, and thus would appear as a very weak undistinguishable feature in Raman spectra.

We base the correspondence between the number of Sm vacancies and intensity of the 10 meV phonon on the estimation of the number of vacancies from the crystal lattice constants performed in Reference 74. The Sm defect-induced phonon at 10 meV shows an extra 50% increase in spectral weight (Figure 5.1) with increasing Sm deficiency by less than 1 % between the two FZ-grown samples. This demonstrates that Raman scattering can be effectively used to characterize the number of Sm vacancies in SmB_6 samples. Moreover, in contrast to the estimation of the number of Sm-vacancies by measurements of a lattice parameter,[74] inelastic light scattering probes the presence of defects on Sm sites directly. In our case care was taken to exclude other origin of defects on Sm cites by checking the elemental content of the samples by EDS measurements. The intensity of 10 meV phonon has almost no spectral weight for the best Al Flux-SmB_6 sample, demonstrating that the sample is the most stoichiometric has the lowest number of Sm vacancies. It is important to emphasize here that the presence of vacancies as was shown in[74] is individual for each sample and does not directly depend on FZ vs Al-Flux method of growth. As an example the sample used for studies in Reference 71 was also measured and shows a similarly small number of Sm vacancies in Raman scattering measurements.

The 21 meV feature has a different origin, and thus shows a reverse dependence on the number of Sm defects at room temperature (see inset in Figure 5.1). A comparison to neutron scattering spectra[82] suggest that it can originate from two overlapping effects: two-phonon scattering from acoustic phonons and valence fluctuations coupled to the lattice deformation (exciton-polaron). For two-phonon scattering from the acoustic (A+A) phonons, in agreement with the expectations[77,83,84] we observe the maximum intensity in A_{1g} polarization and a decrease in intensity on cooling as $(\frac{1}{1-e^{-\frac{\hbar\omega}{kT}}})^2$. An analysis of the symmetry selection rules for two-phonon scattering in O_h crystals is given in Appendix B and is in agreement with the Raman polarization dependence. The origin of the atypically large strength of two-phonon scattering are phonon anomalies due to phonon coupling of d-electrons.[77,85,86] In an imperfect crystal the matrix element which gives rise to the large two-phonon scattering is expected to decrease,[85,86] explaining the decrease of the two-phonon feature on the increase of vacancies. In fact, both an increase of acoustic-phonon Raman-forbidden scattering and the decrease of two-phonon scattering on increase of disorder in the crystals was observed also for substoichiometric transition metal carbides.[86,87]

At 15 K we can well distinguish two components of the discussed feature, the sharper peak at 21.9 meV that has maximum intensity in (x, x) polarization, and a wider polarization-independent component with a maximum at 20.3 meV. The wide component of this feature shows intensity nearly the same for all the samples, suggesting that is has an input from exciton-polaron excitations.

The above analysis of phonon scattering associated with Sm atoms allows us to order the three studied samples by increasing number of Sm vacancies from Al Flux-$SmB_6$to FZ SmB_6-Pure, and further to FZ SmB_6-Def. As the next step we follow the temperature dependence of electronic Raman scattering within this range of samples.

5.3.2 Electronic Raman scattering

In the Raman spectra of all three samples at 300 K, we observe electronic backgrounds which linearly increase in intensity with energy up to about 150 meV (1200 cm^{-1}) and stays constant at higher energies (see Figure 5.1). The background is observed in all four measured polarizations, though it is considerably weaker in (x, y). This background is present in the spectra excited with 488 nm line as well, which suggest

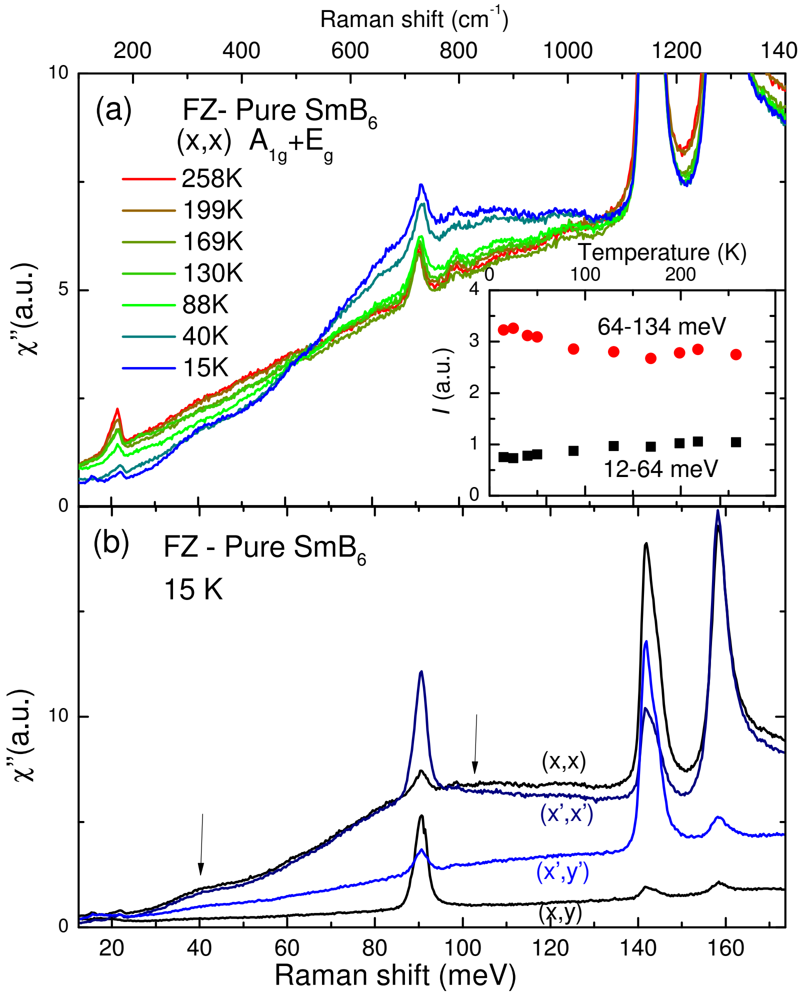

Figure 5.2: (a)Temperature dependence of Raman spectra of the FZ SmB$_6$-Pure sample cooled from 300 K to 15 K in (x, x) polarization. Note redistribution of the spectral weight which occurs below 130 K to the frequencies above 100 meV, and below 50 K to the frequency range above 34 meV. The inset shows a temperature dependence of spectral weight $I(T) = \int_{\omega_1}^{\omega_0} \chi''(T, \omega) d\omega$ below ($\omega_0 = 12$ meV, $\omega_1 =$ 64 meV) and above ($\omega_0 = 64$ meV and $\omega_1 = 134$ meV) the isosbestic point. (b) Raman spectra of FZ SmB$_6$-Pure sample at 15 K in $(x', y'), (x', x'), (x, y)$ and (x, x) polarizations, see Table 5.1. The temperature dependent response is most intense in (x', x') and (x, x) polarizations, suggesting that it belongs to A$_{1g}$ symmetry.

that it originates from electronic Raman scattering.[75]

The changes observed in the Raman spectra of all the samples on cooling from 300 to 15 K are illustrated by the temperature dependence the response of the FZ $\mathrm{SmB_6}$-Pure sample in (x, x) polarization presented in Figure 5.2(a). On decreasing temperatures below 130 K, we detect a spectral weight shift to frequencies above an isosbestic point of 64 meV. The resulting feature with a maximum at about 100 meV continues to develop down to 20 K. We can follow the temperature dependence of the high-frequency feature by following the spectral weight $I(T) = \int_{\omega_1}^{\omega_0} \chi''(T, \omega) d\omega$ below ($\omega_0 = 12$ meV, $\omega_1 = 64$ meV) and above ($\omega_0 = 64$ meV and $\omega_1 = 134$ meV) the isosbestic point. $\chi''(T, \omega)$ is Raman intensity in arbitrary units. Another redistribution of the spectral weight occurs at temperatures below 50 K, resulting in a band at 41 meV with further suppression of the spectral weight below 34 meV. This lower-frequency effects are in general agreement with References 76 and 77, while the feature at about 100 meV was not yet discussed. The total spectral weight of the spectra below 134 meV (the sum of the two parts) is conserved, as expected for a system where a metal-insulator transition is driven by electronic correlations.[88]

As seen from polarization dependence of the spectra at 15 K (Figure 5.2 (b)), both features have the highest intensity in (x, x) and (x', x'), with somewhat lower intensity at the same frequencies observed in (x', y'). This shows that both features appear in $\mathrm{A_{1g}}$ and $\mathrm{E_g}$ symmetries at the same energies. In (x, y) polarization ($\mathrm{T_{2g}}$ symmetry, see Section 5.2.2) the Raman response in this frequency range is low and basically temperature independent, and neither of these two features are observed at 15 K.

Similar changes of the spectra on cooling are observed in the other samples. We compare the (x,x) spectra at 15 K for the samples with different concentrations of Sm vacancies in Figure 5.3. The position and intensity of the feature at 100 meV is the same for all measured samples. The feature at 41 meV gets smeared with an increase of the number of vacancies leaving some spectral weight at low frequencies. We follow this as a decrease of the spectral weight on cooling $I(T) = \int_{\omega_1}^{\omega_0} \chi''(T,\omega) d\omega$ between $\omega_0 = 11$ meV, ω_1 =31.5 meV for FZ SmB$_6$-Pure (red squares) and FZ SmB$_6$-Def (green squares) in the inset (a) in Figure 5.3. The spectral weight shows identical dependence on temperature in both samples down to approximately 50 K. Below this temperature no major changes occur in the low frequencies range for the FZ SmB$_6$-Def sample, while the further decrease of the low frequency spectral weight is observed in FZ SmB$_6$-Pure sample. The resulting correlation between the number of vacancies estimated as the intensity of the 10 meV phonon I(10 meV phonon) and the low frequency spectral weight I(11-31 meV) is shown in the inset (b) of Figure 5.3. With a decrease in the number of vacancies the low frequency spectral weight decreases.

While the low frequency spectral weight has similar values in FZ SmB$_6$-Pure and Al Flux-SmB$_6$ in the spectra of the Al Flux-SmB$_6$ sample at temperatures below 30 K the intensity is concentrated in the narrow features of in-gap excitations (see Figure 5.4 and Figure 5.5) observed both in (x,x) and (x,y) polarizations. Table 5.2

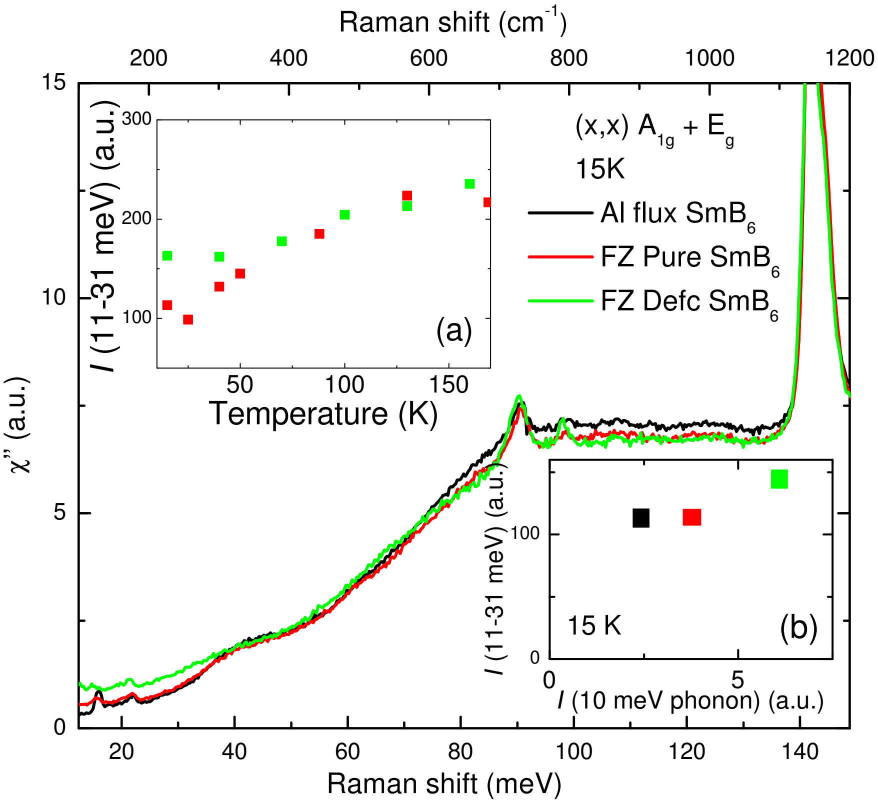

Figure 5.3: Low-temperature Raman spectra of Al Flux-SmB$_6$, FZ SmB$_6$-Pure, and FZ SmB$_6$-Def samples at 15 K in (x, x) polarization. Note an increase of in-gap intensity and smearing of 41 meV feature with the increase in Sm vacancies. (a) Temperature dependence of the spectral weight $I(T) = \int_{\omega_1}^{\omega_0} \chi''(T, \omega) d\omega$ below 31.5 meV in FZ SmB$_6$-Pure sample (red dots) vs FZ SmB$_6$-Def sample (green dots). The difference becomes apparent below 50 K, where the 41 meV feature starts to develop in the spectra. (c) Spectral weight below 31.5 meV plotted against the intensity of the defect phonon. Note the increase of the low frequency spectral weight with the increase of the number of Sm vacancies.

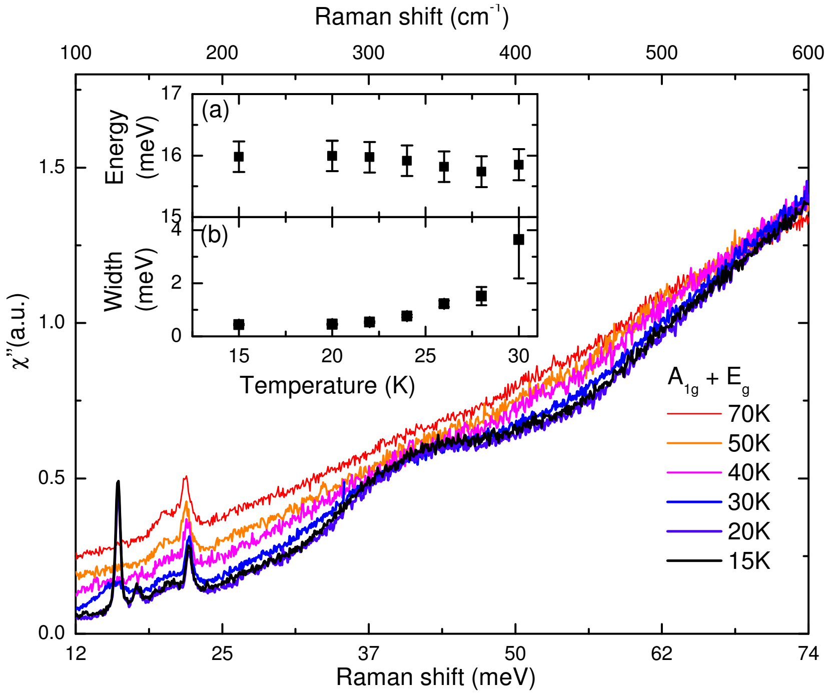

Figure 5.4: Temperature dependence of the low frequency Raman response of Al Flux-SmB$_6$ sample in (x, x) polarization. The exciton feature appears below 30 K at 16 meV. The inset shows a change of the position and width of the exciton on cooling.

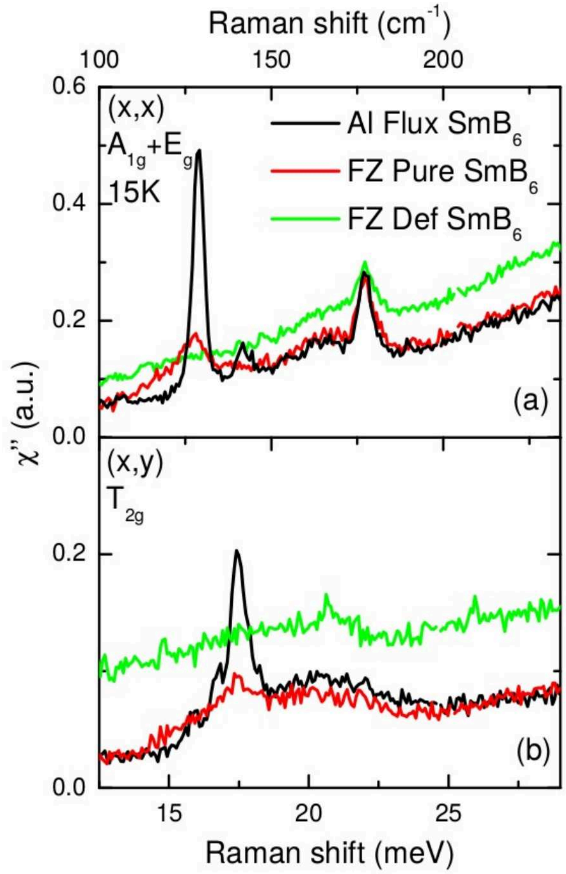

Figure 5.5: Raman spectra in the frequency range of the exciton feature at 15 K for the measured samples, Al Flux-SmB$_6$, FZ SmB$_6$-Pure, and FZ SmB$_6$-Def in (x, x) polarization (a) and (x, y) polarization (b).

Table 5.2: Polarization dependence, symmetry, frequency and width of the excitonic features observed in the samples with the smaller numbers of Sm vacancies (Al Flux-SmB_6 and FZ SmB_6-Pure) at 15 K.

		Al Flux		FZ Pure	
Polarization	Symmetry	ω (meV)	γ (meV)	ω (meV)	γ (meV)
(x,y)	T_{2g}	15.9	0.7		
(x,x)	E_g	16.0	0.5	15.6	1.7
(x,y)	T_{2g}	16.7	0.7		
(x,y)	T_{2g}	17.5	0.7	17.4	1.5

lists all of the in-gap features, including those in (x,y) polarization, and their symmetry assignment following Reference 77. The temperature behaviour followed in (x,x) polarization shows that the sharp peak forms when the spectral weight at low frequencies becomes sufficiently low, the frequency of the feature stays the same 16.0 meV, while the width decreases with temperature till it reaches the value of about 0.5 meV (see Figure 5.4 (b)).

In the FZ SmB_6-Pure sample a lower intensity and wider (1.7 meV) in-gap feature at 15.6 meV is superimposed on an even wider (4.7 meV) background. The in-gap excitations are not observed in the spectra of the FZ SmB_6-Def, where higher electronic scattering intensity is present at frequencies within the hybridization gap (Figure 5.5).

5.4 Discussion

The excitations revealed in the low temperature Raman spectra are of electronic origin and appear due to hybridization of $5d$ and $4f$ orbitals, as suggested by their temperature dependence and energy scale. The low temperature electronic Raman spectra can be compared to the band structure calculations, which take into account electronic correlations and hybridization of 5d and 4f bands and reproduce the hybridization gap and band inversion in $\mathrm{SmB_6}$.[55,69,70] On the other hand, the change of the low-frequency electronic Raman spectra of $\mathrm{SmB_6}$ on cooling, the formation of hybridization gap, and polarization dependence of the spectra can be compared to the calculations of electronic Raman spectra for a system with localization effects originating from electronic correlations.[88]

The shift of the spectral weight to the higher frequencies on cooling indicates the formation of an insulating gap due to correlation effects, as was already discussed in connection with $\mathrm{SmB_6}$ low frequency Raman spectra.[88] In our measurements, for all the samples the spectral weight is conserved above 105 meV (850 $\mathrm{cm^{-1}}$), this cutoff indicating the energy scales associated with the formation of the hybridization gap.

Of the band structure calculations, in particular those performed by the LDA+Gutzwiller method presented in Reference 70 provides bands energies which correspond well to the electronic excitations observed in our data at low temperatures. The calculations show the hybridized 5d and 4f bands, where 4f $j = 5/2$ band splits into two Γ_7^f and one Γ_6^f bands resulting in band inversion in the vicinity of the X point of the BZ and a formation of a semiconductor-like gap. The possible interband excitations would have energies close to the 41 and 100 meV observed in our experiment (Figure 3 in Reference 70). Interestingly, optical conductivity also shows a broad peak at around

100 meV.[65] In inversion symmetric crystals Raman measurements should only probe electronic transitions from bands of the same parity while infrared is limited to bands of different parity. Here the mixed parity of the hybridized $5d-4f$ orbitals in SmB_6 apparently allows this transition to appear in both measurements.

Depending on the measured polarization, Raman scattering probes electronic excitations at different parts of the BZ.[41] The response in A_{1g} probes the excitations over the whole BZ The 100 meV and 41 meV features appear with the highest intensity in A_{1g} symmetry. According to the calculations,[70] the dispersions of the relevant bands along the Γ-X direction are relatively flat, and thus would result in peaks in the Raman response. E_g symmetry which corresponds to B_{1g} for D_{4h} point group probes the transitions around the X point and is expected to show Raman response due to correlation effects.[89] We do observe both features in E_g response at similar frequencies as in A_{1g} within the precision of the measurements, which is in agreement with the flat band dispersion.

Following the interpretation of the low temperature spectra within the band structure calculations,[70] we would expect to observe a predicted much larger gap in T_{2g} symmetry, which probes the M point of the BZ. However, in this symmetry the Raman electronic background has low intensity which does not change with temperature (see Figure 2 (b)). On the other hand, the Raman response due to correlation effects in T_{2g} which can be projected on B_{2g} for D_{4h} symmetry is predicted to be zero[89] in approximations of cosine bands. This absence of temperature-dependent response in

T_{2g} can be taken as an evidence of the defining importance of the electronic correlations for the effects observed in SmB_6 spectra and a limitation of the band-structure approach.

The two features in the Raman spectrum at 100 and 41 meV associated with hybridization of the $5d$ and $4f$ orbitals start to develop at 130 and 50 K, respectively. At low temperatures, the 100 meV feature has equal intensity in all three samples, as seen from Figure 5.3. The differences in the low-frequency spectral weight between FZ SmB_6-Pure and FZ SmB_6-Def samples appear only below 50 K (Figure 5.3, inset (a)). The depressed Raman intensity below roughly 30 meV in A_{1g} and E_g symmetries in Al Flux-SmB_6 and FZ SmB_6-Pure samples is a result of the opening of the hybridization gap. By evaluating in-gap spectral weight in the gap (Figure 5.3(b)) we cannot distinguish the two samples with the least number of vacancies, Al Flux-SmB_6 and FZ SmB_6-Pure while we observe a somewhat higher intensity in the spectra of FZ SmB_6-Pure sample at low frequencies. With the increase of the number of Sm vacancies for the FZ SmB_6-Def sample, an increase of the in-gap spectral weight and the respective decrease of the 41 meV band are detected. This increase of the amount of the in-gap spectral weight suggests that the hybridization gap is not opened completely in FZ SmB_6-Def sample.

At 15 K we observe the sharp in-gap excitations at about 16 meV in Al Flux-SmB_6 while in FZ SmB_6-Pure spectra the same spectral weight is spread over wide frequency range in the gap, with a wide peak in the same range (Figure 5.5). The excitation at 16 meV can be interpreted in terms of an in-gap exciton. The respective excitonic level is proposed to be formed by electrons of hybridized bands in the gap as a result of strong electron-electron correlations and is protected from decay by the hybridization gap.[90] The excitonic feature was observed in neutron scattering measurements at finite momentum transfers with scattering intensity at the X and R high symmetry points of the BZ.[71] The most intense feature observed in Raman spectra belongs to E_g symmetry, which probes the excitation at the X point of the BZ.[71] Raman probes zero momentum transfer direct transitions, and thus the energies of these excitation of 16 meV is expected to be higher than that observed in neutron scattering at 14 meV at X point.

The multiple features of T_{2g} symmetry (Figure 5.5, Table 5.2) cannot be assigned to pure electronic response. The previous work[76,77] proposes an alternative model for the multiple excitonic features which appear as a result of a splitting of crystal field levels by coupling with phonons.[91] According to the model, the feature at 16 meV in E_g symmetry has dominant electronic contribution, while multiple exciton-related features in T_{2g} symmetry have dominant phonon contribution.[77]

The low line width of the excitonic features observed in the Al Flux-SmB_6 sample (0.5 meV) is evidence of a long life time protected by the hybridization gap. The widening of the feature on the increase of the number of vacancies in FZ SmB_6-Pure shows that some electronic states are present within the gap energies and lead to the exciton decay. Respectively, no exciton features are detected in the spectra of FZ

SmB_6-Def since the gap is not fully opened in this material.

Our Raman results for FZ-grown samples are mirrored by transport measurements which show a decrease of the metallic-like plateau in resistivity at low temperatures and more insulating behavior for the FZ SmB_6-Pure samples compared to FZ SmB_6-Def.[74] Such results emphasize the dramatic effect the presence of Sm vacancies has on the bulk hybridization gap necessary for the existence of TKI. While in the most stoichiometric samples (Al Flux-SmB_6 in this study) we find the hybridization gap fully opened and detect the presence of the in-gap exciton, which serves as evidence of the TKI state, even as little as 1% Sm vacancies due to the growth condition suppresses the development of hybridization gap and can eliminate the TKI state. Moreover, the significant broadening of the excitons with the introduction of very few vacancies suggests the collective nature of these modes and possibly evidences the sensitivity of the Kondo insulating state to disorder.

In this study along with a comparison to previously published transport measurements, we see that a decrease in the low temperature resistivity can result in both stoichiometrically pure samples as well as samples with increasing numbers of vacancies. However, based on Raman measurements of the bulk, the most stoichiometric samples show a clear opening of the hybridization gap indicating the additional conduction must be restricted to the surface while the vacancies seen in some of the FZ samples suppress the complete opening of the gap which provides channels for bulk conduction. We find that given the relatively small number of vacancies present in the more pure end of a “typical” FZ sample can suppress though not necessarily eliminate resistivity plateauing as well as the excitons, there is evidence that the coherence of the Kondo insulating state is easily disrupted and may destroy the topologically protected surface states in off stoichiometric samples.

5.5 Conclusions

We present a Raman scattering study of $\mathrm{SmB_6}$ samples with different numbers of Sm vacancies. We show that Raman scattering is an extremely sensitive method to characterise the number of Sm vacancies by the estimation of the intensity of the Raman-forbidden phonon of Sm at 10 meV which appears in the spectra due to the local symmetry breaking by Sm vacancies.

In the Raman spectra below 130 K for all the samples we observe a development of the electronic features at 100 and 41 meV in A_{1g} and E_g symmetries. Based on the recent band structure calculations we assign the features to the excitations between the bands in the electronic structure which appear due to hybridization between $5d$ and $4f$ orbitals. In turn, our Raman study provides experimental data on electronic structure of $\mathrm{SmB_6}$ to support the calculations. In this interpretation, the band at about 41 meV is the excitation across the hybridization gap. While the feature at 100 meV develops equally in all the samples, with an increasing of the number of Sm vacancies up to approximately 1% the hybridization gap stays filled with states without a detectable shift in the positions of the bands.

For the samples with the low number of Sm vacancies in E_g symmetry, which probes the X point of BZ we observe a feature of excitonic excitation at 16 meV. The extremely low width of 0.5 meV of the exciton feature in Al Flux-SmB$_6$ spectra suggests the extremely long life time of the level. The presence of Sm vacancies lead to a decrease of the exciton life time with eventual decay of the exciton through the electronic states present in the hybridization gap at of 1% of vacancies.

Our results indicate that an introduction of 1% of Sm vacancies affects the formation of the hybridization gap and the lifetime of the in-gap excitons, resulting in bulk conduction through impurity channels. These effects appear to be correlated with a loss of low temperature resistivity plateauing which would suggest topological surface states may only be present in the most pure SmB$_6$ samples where no filling of the hybridization gap is observed. Therefore, the importance of characterizing sample quality, and in particular the value of symmetry sensitive techniques, cannot be overstated in the effort to understand the possible TKI state in SmB$_6$.

Chapter 6

Summary

In this work, we characterize the sensitivity of two classes of strongly-correlated electron systems, triangular lattice frustrated magnets and topological Kondo insulator SmB_6, to structural disorder and distortions. Inelastic light scattering was used as a probe electronic and magnetic properties and a means for identifying weak disorder through vibrational excitations.

The frustrated magnet systems studied included the anisotropic triangular lattice system α-$SrCr_2O_4$ and the triangular lattice system with competing ferromagnetic and antiferromagnetic interactions $NiGa_2S_4$. For α-$SrCr_2O_4$, which is known to develop incommensurate helical magnetic order below 43 K, studied the Raman response from 300 K down to 15 K across the transition from the paramagnetic state to the magnetically ordered state. The spectra show both vibrational and magnetic excitations that were compared with DFT calculations. Scattering from phonons demonstrated a coupling of the lattice with the magnetically ordered state through a redistribution of phonon intensities around the ordering temperature in the 467 and 474 cm^{-1} phonons which primarily involve vibrations of the oxygen octahedra as well as an enhancement of the 81 cm^{-1} phonon involving strontium motion. Additionally, we detected magnetic peaks at 20 and 40 meV which qualitatively correspond to the Raman response calculated for a 120° ordered antiferromagnet. This result in conjunction with the DFT calculations of magnetic exchange interactions gives positions of the peaks as $4.0J_{av}$ and $8.0J_{av}$. These features are distinguishable up to 80 K which evidences the short range correlations that persist above the ordering temperature.

The triangular lattice compound NiGa_2S_4 with competing nearest-neighbor ferromagnetic and third nearest neighbor antiferromagnetic interactions shows spin freezing at temperatures below 10 K rather than magnetic ordering contrary to theoretical predictions. The nature of the interactions with a stronger third nearest neighbor interaction of 2.8 meV and a nearest neighbor interaction of 1.0 meV suggests the primary mechanism for the exchange interaction is superexchange through the sulfur sites rather than Ni-Ni direct exchange. We presented evidence for disorder and symmetry breaking that would alter how this system is modeled. At 300 K, we compare experimental Raman phonon widths to DFT calculations of the lattice mode eigenvectors. The phonon widths are found to be roughly proportional to the energy associated with the superexchange sulfur atoms which indicates that the sulfur vacancies known to occur within this compound are primarily confined to these sites.

Due to sulfur vacancies, the Ni-Ni exchange interactions will vary and likely provide the necessary disorder to suppress magnetic ordering. Upon cooling below 300 K, symmetry forbidden IR active phonon modes appear in the Raman spectrum. This can only occur when the inversion symmetry of the crystal is broken and leads to the possibility that a DM interaction term is also contributing to the spin dynamics of the system.

The final component of this thesis was devoted to investigating variations among SmB_6 samples with different growth techniques and identifying their impact on the topological nontriviality of the bulk band structure. We demonstrate Raman spectroscopy as an effective method for verifying sample quality by the appearance of defect-induced zone-edge acoustic phonon scattering in the spectrum for known to have Sm vacancies. The intensity of this 10 meV defect-induced phonon provides an estimate of the number of imperfections within a sample and is used to develop a gradient of samples with Sm vacancies to determine their effect on the bulk band structure. In the electronic spectrum of the most stoichiometrically pure samples, we see an opening of the hybridization gap of about 20 meV at temperatures below 50 K with the formation of broad peaks at 41 and 100 meV that correspond to excitations of the split $4f$ levels across the gap. With the formation of the hybridization gap at low temperatures, narrow exciton features appear at energies between 16 and 18 meV. The introduction of less than 1% Sm vacancies leads to impurities states within the gap that suppress the long lifetime of the exciton features. In the sample with only about 1% Sm vacancies the electronic gap is closed which provides evidence for bulk conduction.

Appendix A

Symmetry analysis

A.1 D_{2h} point group

The effect each of symmetry operations has on Cartesian coordinates x, y, and z is given below. As an example we can see how the function $f(x, y, z) = x$ is mapped onto itself for operators E, C_2^x, σ^{xy}, and σ^{xz}, and is mapped onto $-x$ for C_2^y, C_2^z, i, and σ^{yz} which matches the characters of the B_{3u} irreducible representation, from Table A.1. This means the function x forms a basis for the B_{3u} irreducible representation, and it is listed in the linear column of functions on the right side of the character table. Similarly, we can see that y and z are bases for the B_{2u} and B_{1u} representations, respectively.

Table A.1: Character table for the D_{2h} point group which has orthorhombic symmetry

D_{2h} point group

Irr.	Symmetry operations								Functions		
Reps.	E	C_2^z	C_2^y	C_2^x	i	σ^{xy}	σ^{xz}	σ^{yz}	Lin.	Quad.	Cubic
A_g	1	1	1	1	1	1	1	1		x^2, y^2, z^2	
B_{1g}	1	1	-1	-1	1	1	-1	-1	R^z	xy	
B_{2g}	1	-1	1	-1	1	-1	1	-1	R^y	xz	
B_{3g}	1	-1	-1	1	1	-1	-1	1	R^x	yz	
A_u	1	1	1	1	-1	-1	-1	1			xyz
B_{1u}	1	1	-1	-1	-1	-1	1	1	z		z^3, $z(x^2-y^2)$
B_{2u}	1	-1	1	-1	-1	1	-1	1	y		yz^2, $y(3x^2-y^2)$
B_{3u}	1	-1	-1	1	-1	1	1	-1	x		xz^2, $x(x^2-3y^2)$

$$E(x,y,z) = (x,y,z)$$

$$C_2^z(x,y,z) = (-x,-y,z)$$

$$C_2^y(x,y,z) = (-x,y,-z)$$

$$C_2^x(x,y,z) = (x,-y,-z)$$

$$i(x,y,z) = (-x,-y,-z)$$

$$\sigma^{xy}(x,y,z) = (x,y,-z)$$

$$\sigma^{xz}(x,y,z) = (x,-y,z)$$

$$\sigma^{yz}(x,y,z) = (-x,y,z)$$

We can also consider higher-order functions and the effect that the coordinate changes will have on them. As an example some symmetry operations on the second-order function xy are,

$$C_2^z(xy) = (-x)(-y) = 1 \cdot xy$$

$$C_2^y(xy) = (-z)(y) = -1 \cdot xy.$$

Carrying this through we find that xy is even for E, C_2^z, i, and σ^{xy}, and odd for C_2^x, C_2^y, σ^{xz}, and σ^{yz}, which makes it a basis for the B_{1g} representation. The first, second, and third order functions for D_{2h} are given in Table A.1.

The significance of these basis functions lies in the fact that an electric dipole interaction $\epsilon \cdot e\mathbf{r}$ has the spatial dependence of one of the linear Cartesian components x, y, or z. Therefore, a single photon absorption or emission process will have a matrix element of

$$\langle f| \hat{H}_{ED} |i\rangle . \tag{A.1}$$

The electric-dipole operator portion of this transition will be a basis for the representations of the linear functions, B_{1u}, B_{2u}, and B_{3u}. The wavefunction $|i\rangle$ in the case of most Stokes scattering at room temperature will be in the ground state which has the symmetry of crystal represented by the A_g representation. Finally, the $|f\rangle$ excited state wavefunction will have a symmetry of one of the irreducible representations that depends on the type of mode that is excited. As stated previously, the integration of Eqn. A.1 will only be nonzero when the product of the three symmetries contains the fully symmetric representation, A_g for D_{2h}. Considering the symmetries of these elements for an excitation of final state symmetry A_u gives,

$$A_u \begin{pmatrix} B_{1u} \\ B_{2u} \\ B_{3u} \end{pmatrix} A_g = \begin{pmatrix} B_{1u} \\ B_{2u} \\ B_{3u} \end{pmatrix} . \tag{A.2}$$

Here the middle terms are the three possible symmetries the electric-dipole operator can take since they correspond to the three linear functions on the right side of Table A.1. None of the three possible symmetries on the right side of the equation contains the fully symmetric A_g so a final state of A_u is forbidden in single photon processes. However, for a final state symmetry of B_{1u} we get the product,

$$B_{1u}\begin{pmatrix} B_{1u} \\ B_{2u} \\ B_{3u} \end{pmatrix} A_g = \begin{pmatrix} A_g \\ B_{3g} \\ B_{2g} \end{pmatrix}. \tag{A.3}$$

Irreducible representation multiplication tables can were used here to get the product on the right side of the equation. An overall A_g symmetry is found for the B_{1u} channel of the dipole operator so the excitation will be observable by absorption of photons polarized in the z direction but not photons polarized in the y or x directions which correspond to $B_{2u}$and B_{3u}symmetries.

The inelastic light scattering process involves both the absorption and creation of a photon through two electric-dipole interactions so two spatial directions will be relevant. The $\hat{H}_{Raman}$ term has both incident and scattered electric fields which each select out a spatial coordinate of $\partial\chi^{ij}/\partial U$, and thus the second-rank tensor of Raman scattering has the symmetries of the quadratic functions. For example, we can see that scattering to final electron states of B_{1g} is an allowed process when observing scattered light of x polarization from incident light of y polarization.

$$B_{1g} \begin{pmatrix} A_g \\ B_{1g} \\ B_{2g} \\ B_{3g} \end{pmatrix} A_g = \begin{pmatrix} B_{1g} \\ A_g \\ B_{3g} \\ B_{2g} \end{pmatrix}. \tag{A.4}$$

As may be noted, the fully symmetric representation will only be present on the right side of the equation when the symmetry of the excitation matches the symmetry of the Raman or electric-dipole operator so determining whether scattering is allowed for a given excitation becomes fairly trivial. The this process of determining allowed symmetries can be continued to the cubic functions in Table— which would correspond to three photon process and so on. These higher order terms have increasingly smaller cross sections and thus become much more difficult to measure.

A.2 O_h point group

In the orthorhombic symmetry of D_{2h} each of the three lattice parameters are distinct meaning none of the crystallographic axes can be interchanged and all of the irreducible representations will be one dimensional. However, for higher crystal symmetries we can find that some of the symmetry operations map one of the crystallographic axes onto another leading to two and three dimensional representations. The character table for the cubic O_h point group is given in Table A.2.

The here we have doubly degenerate E and triply degenerate T representations.

Table A.2: Character table for the O_h point group which has orthorhombic symmetry

O_h point group

Irr.	Symmetry operations										Functions	
Reps.	E	C_3	C_2	C_4	$(C_4)^2$	i	S_4	S_6	σ_h	σ_d	Linear	Quadratic
A_{1g}	1	1	1	1	1	1	1	1	1	1		$x^2 + y^2 + z^2$
A_{2g}	1	1	-1	-1	1	1	-1	1	1	-1		
E_g	2	-1	0	0	2	2	0	-1	2	0		$(2z^2 - x^2 - y^2, x^2 - y^2)$
T_{1g}	3	0	-1	1	-1	3	1	0	-1	-1	(R^x, R^y, R^z)	
T_{2g}	3	0	1	-1	-1	3	-1	0	-1	1		(xy, yz, zx)
A_{1u}	1	1	1	1	1	-1	-1	-1	-1	-1		
A_{2u}	1	1	-1	-1	1	-1	1	-1	-1	1		
E_u	2	-1	0	0	2	-2	0	1	-2	0		
T_{1u}	3	0	-1	1	-1	-3	-1	0	1	1	(x, y, z)	
T_{2u}	3	0	1	-1	-1	-3	1	0	1	-1		

The mappings of the coordinates with each of the symmetry operations are below.

$$
\begin{aligned}
E(x,y,z) &= (x,y,z) \\
C_3^{(111)}(x,y,z) &= (z,x,y) \\
C_2^{(110)}(x,y,z) &= (y,x,-z) \\
C_4^{(100)}(x,y,z) &= (-y,x,z) \\
C_2^{(100)}(x,y,z) &= (-x,-y,z) \\
i(x,y,z) &= (-x,-y,-z) \\
S_4^{(100)}(x,y,z) &= (-y,x,-z) \\
S_6^{(111)}(x,y,z) &= (-y,-z,-x) \\
\sigma_h(x,y,z) &= (-y,x,-z) \\
\sigma_d(x,y,z) &= (y,x,z)
\end{aligned}
$$

We see that if as before we consider how the function $f(x,y,z) = x$ is affected by each of the symmetry operations, it is no longer mapped onto just $\pm x$ but also involves y and z for certain operators. As a result we must consider the linear functions together as a single vector function in equation in Eqn 2.10.

$$C_3^{(111)}\begin{pmatrix} z \\ x \\ y \end{pmatrix} = \begin{pmatrix} (x) \\ (y) \\ (z) \end{pmatrix} = \begin{pmatrix} 0 & 0 & 1 \\ 1 & 0 & 0 \\ 0 & 1 & 0 \end{pmatrix}\begin{pmatrix} x \\ y \\ z \end{pmatrix} \tag{A.5}$$

Where the trace of the matrix M gives the character found in the O_h table which is 0 for the $C_3^{(111)}$ operation of the T_{1u}representation that functions (x, y, z) form a basis form. The more complicated process showing the mappings of the (xy, yz, zx) functions is given below where again we can take the trace of the 3×3 matrix on the right to get the characters of the triply degenerate T_{2g}.

$$E\begin{pmatrix} xy \\ yz \\ zx \end{pmatrix} = \begin{pmatrix} (x)(y) \\ (y)(z) \\ (z)(x) \end{pmatrix} = \begin{pmatrix} 1 & 0 & 0 \\ 0 & 1 & 0 \\ 0 & 0 & 1 \end{pmatrix}\begin{pmatrix} xy \\ yz \\ zx \end{pmatrix}$$

$$C_3^{(111)}\begin{pmatrix} xy \\ yz \\ zx \end{pmatrix} = \begin{pmatrix} (z)(x) \\ (x)(y) \\ (y)(z) \end{pmatrix} = \begin{pmatrix} 0 & 0 & 1 \\ 1 & 0 & 0 \\ 0 & 1 & 0 \end{pmatrix}\begin{pmatrix} xy \\ yz \\ zx \end{pmatrix}$$

$$C_2^{(110)} \begin{pmatrix} xy \\ yz \\ zx \end{pmatrix} = \begin{pmatrix} (y)(x) \\ (x)(-z) \\ (-z)(x) \end{pmatrix} = \begin{pmatrix} 1 & 0 & 0 \\ 0 & 0 & -1 \\ 0 & -1 & 0 \end{pmatrix} \begin{pmatrix} xy \\ yz \\ zx \end{pmatrix}$$

$$C_4^{(100)} \begin{pmatrix} xy \\ yz \\ zx \end{pmatrix} = \begin{pmatrix} (-y)(x) \\ (x)(z) \\ (z)(-y) \end{pmatrix} = \begin{pmatrix} -1 & 0 & 0 \\ 0 & 0 & 1 \\ 0 & -1 & 0 \end{pmatrix} \begin{pmatrix} xy \\ yz \\ zx \end{pmatrix}$$

$$C_2^{(100)} \begin{pmatrix} xy \\ yz \\ zx \end{pmatrix} = \begin{pmatrix} (-x)(-y) \\ (-y)(z) \\ (z)(-x) \end{pmatrix} = \begin{pmatrix} 1 & 0 & 0 \\ 0 & -1 & 0 \\ 0 & 0 & -1 \end{pmatrix} \begin{pmatrix} xy \\ yz \\ zx \end{pmatrix}$$

$$i \begin{pmatrix} xy \\ yz \\ zx \end{pmatrix} = \begin{pmatrix} (-x)(-y) \\ (-y)(-z) \\ (-z)(-x) \end{pmatrix} = \begin{pmatrix} 1 & 0 & 0 \\ 0 & 1 & 0 \\ 0 & 0 & 1 \end{pmatrix} \begin{pmatrix} xy \\ yz \\ zx \end{pmatrix}$$

$$S_4^{(100)} \begin{pmatrix} xy \\ yz \\ zx \end{pmatrix} = \begin{pmatrix} (-y)(x) \\ (x)(-z) \\ (-z)(-y) \end{pmatrix} = \begin{pmatrix} -1 & 0 & 0 \\ 0 & 0 & -1 \\ 0 & 1 & 0 \end{pmatrix} \begin{pmatrix} xy \\ yz \\ zx \end{pmatrix}$$

$$S_6^{(111)}\begin{pmatrix} xy \\ yz \\ zx \end{pmatrix} = \begin{pmatrix} (-y)(-z) \\ (-z)(-x) \\ (-x)(-y) \end{pmatrix} = \begin{pmatrix} 0 & 1 & 0 \\ 0 & 0 & 1 \\ 1 & 0 & 0 \end{pmatrix}\begin{pmatrix} xy \\ yz \\ zx \end{pmatrix}$$

$$\sigma_h\begin{pmatrix} xy \\ yz \\ zx \end{pmatrix} = \begin{pmatrix} (x)(y) \\ (y)(-z) \\ (-z)(x) \end{pmatrix} = \begin{pmatrix} 1 & 0 & 0 \\ 0 & -1 & 0 \\ 0 & 0 & -1 \end{pmatrix}\begin{pmatrix} xy \\ yz \\ zx \end{pmatrix}$$

$$\sigma_d\begin{pmatrix} xy \\ yz \\ zx \end{pmatrix} = \begin{pmatrix} (y)(x) \\ (x)(z) \\ (z)(y) \end{pmatrix} = \begin{pmatrix} 1 & 0 & 0 \\ 0 & 0 & 1 \\ 0 & 1 & 0 \end{pmatrix}\begin{pmatrix} xy \\ yz \\ zx \end{pmatrix}$$

For the two dimensional representation the basis functions used for Raman spectroscopy look a bit more complicated, but are still defined in the same way.

$$E\begin{pmatrix} 2z^2-x^2-y^2 \\ x^2-y^2 \end{pmatrix} = \begin{pmatrix} 2(z)^2-(x)^2-(y)^2 \\ (x)^2-(y)^2 \end{pmatrix} = \begin{pmatrix} 1 & 0 \\ 0 & 1 \end{pmatrix}\begin{pmatrix} 2z^2-x^2-y^2 \\ x^2-y^2 \end{pmatrix}$$

$$C_3^{(111)}\begin{pmatrix} 2z^2-x^2-y^2 \\ x^2-y^2 \end{pmatrix} = \begin{pmatrix} 2(y)^2-(z)^2-(x)^2 \\ (z)^2-(x)^2 \end{pmatrix} = \begin{pmatrix} -\frac{1}{2} & -\frac{3}{2} \\ \frac{1}{2} & -\frac{1}{2} \end{pmatrix}\begin{pmatrix} 2z^2-x^2-y^2 \\ x^2-y^2 \end{pmatrix}$$

It is common to write these functions as Raman tensors which show the elements of the susceptibility tensor that contribute to inelastic scattering. For the O_h point group we will have 6 Raman tensors.

$$A_{1g} = \begin{pmatrix} a & 0 & 0 \\ 0 & a & 0 \\ 0 & 0 & a \end{pmatrix}$$

$$E_g = \begin{pmatrix} b & 0 & 0 \\ 0 & b & 0 \\ 0 & 0 & -2b \end{pmatrix}, \begin{pmatrix} -\sqrt{3}b & 0 & 0 \\ 0 & -\sqrt{3}b & 0 \\ 0 & 0 & 0 \end{pmatrix}$$

$$T_{2g} = \begin{pmatrix} 0 & c & 0 \\ c & 0 & 0 \\ 0 & 0 & 0 \end{pmatrix}, \begin{pmatrix} 0 & 0 & c \\ 0 & 0 & 0 \\ c & 0 & 0 \end{pmatrix}, \begin{pmatrix} 0 & 0 & 0 \\ 0 & 0 & c \\ 0 & c & 0 \end{pmatrix}$$

The functions in the character table tell us the symmetries of excitations that will contribute to different elements of the susceptibility tensor, but it is still necessary to connect this to scattering geometries through Eqn 2.9 by projecting out different vectors of incidnet and scattered polarizations.

In order to extract complete information about independent symmetry channel in a crystal with O_h symmetry, four scattery geometries must be measured: $(\mathbf{x},\mathbf{x}),(\mathbf{x},\mathbf{y}),(\mathbf{x}+\mathbf{y},\mathbf{x}+\mathbf{y})$, and $(\mathbf{x}+\mathbf{y},\mathbf{x}-\mathbf{y})$. Primed variables will be used to denote the polarization vectors at 45° from the crystalographic axes. The cubic symmetry of the crystal holds that no additional information will be gained by measuring the equivalent polarizations on the other (100) planes of the crystal. The components of χ^{ij} that are probed for each of these orientations is as follows.

$$I_{xx} \sim \left| \begin{pmatrix} 1 & 0 & 0 \end{pmatrix} \begin{pmatrix} \chi^{xx} & \chi^{xy} & \chi^{xz} \\ \chi^{yx} & \chi^{yy} & \chi^{yz} \\ \chi^{zx} & \chi^{zy} & \chi^{zz} \end{pmatrix} \begin{pmatrix} 1 \\ 0 \\ 0 \end{pmatrix} \right|^2 = |\chi^{xx}|^2 \tag{A.6}$$

$$I_{xy} \sim \left| \begin{pmatrix} 1 & 0 & 0 \end{pmatrix} \begin{pmatrix} \chi^{xx} & \chi^{xy} & \chi^{xz} \\ \chi^{yx} & \chi^{yy} & \chi^{yz} \\ \chi^{zx} & \chi^{zy} & \chi^{zz} \end{pmatrix} \begin{pmatrix} 0 \\ 1 \\ 0 \end{pmatrix} \right|^2 = |\chi^{xy}|^2 \tag{A.7}$$

$$I_{x'x'} \sim \left| \begin{pmatrix} 1 & 1 & 0 \end{pmatrix} \begin{pmatrix} \chi^{xx} & \chi^{xy} & \chi^{xz} \\ \chi^{yx} & \chi^{yy} & \chi^{yz} \\ \chi^{zx} & \chi^{zy} & \chi^{zz} \end{pmatrix} \begin{pmatrix} 1 \\ 1 \\ 0 \end{pmatrix} \right|^2 = |\chi^{xx} + \chi^{xy} + \chi^{yx} + \chi^{yy}|^2 \tag{A.8}$$

$$I_{x'y'} \sim \left| \begin{pmatrix} 1 & 1 & 0 \end{pmatrix} \begin{pmatrix} \chi^{xx} & \chi^{xy} & \chi^{xz} \\ \chi^{yx} & \chi^{yy} & \chi^{yz} \\ \chi^{zx} & \chi^{zy} & \chi^{zz} \end{pmatrix} \begin{pmatrix} 1 \\ -1 \\ 0 \end{pmatrix} \right|^2 = |\chi^{xx} - \chi^{xy} + \chi^{yx} - \chi^{yy}|^2 \tag{A.9}$$

Also, for certain systems, circularly polarized light given by $R = 1/\sqrt{2}(x - iy)$ and $L = 1/\sqrt{2}(x + iy)$ will provide additional information.

$$I_{RR} \sim \left| \begin{pmatrix} 1 & -i & 0 \end{pmatrix} \begin{pmatrix} \chi^{xx} & \chi^{xy} & \chi^{xz} \\ \chi^{yx} & \chi^{yy} & \chi^{yz} \\ \chi^{zx} & \chi^{zy} & \chi^{zz} \end{pmatrix} \begin{pmatrix} 1 \\ -i \\ 0 \end{pmatrix} \right|^2 = |\chi^{xx} - \chi^{yy} - i(\chi^{yx} + \chi^{xy})|^2 \tag{A.10}$$

$$I_{RL} \sim \left| \begin{pmatrix} 1 & i & 0 \end{pmatrix} \begin{pmatrix} \chi^{xx} & \chi^{xy} & \chi^{xz} \\ \chi^{yx} & \chi^{yy} & \chi^{yz} \\ \chi^{zx} & \chi^{zy} & \chi^{zz} \end{pmatrix} \begin{pmatrix} 1 \\ -i \\ 0 \end{pmatrix} \right|^2 = |\chi^{xx} + \chi^{yy} + i(\chi^{yx} - \chi^{xy})|^2 \tag{A.11}$$

Appendix B

Selection rules for second-order scattering from O_h crystals

In order to extract complete information about independent symmetry channel in a crystal with O_h symmetry, four scattery geometries must be measured: $(\mathbf{x},\mathbf{x}), (\mathbf{x},\mathbf{y}), (\mathbf{x}+\mathbf{y},\mathbf{x}+\mathbf{y}),$ and $(\mathbf{x}+\mathbf{y},\mathbf{x}-\mathbf{y})$. Primed variables will be used to denote the polarization vectors at 45° from the crystalographic axes. The cubic symmetry of the crystal holds that no additional information will be gained by measuring the equivalent polarizations on the other (100) planes of the crystal. The components of χ^{ij} that are probed for each of these orientations are given in Equations A.6 to A.9.

At a general point in the BZ that does not lie along one of the high symmetry directions, there will be no symmetry operations for the crystal, which will be represented by the trivial C_1 point group. For trivial symmetry, no absolute selection rules emerge for light scattering measurements, and thus one might expect that little additional information for these excitations can be extracted by varying the polarizations of the incident and scattered photons. However, the second-order scattering spectrum, which represents a weighted two-phonon density of states, will tend to have sharp features resulting from Van-Hove singularities which occur at the high symmetry points in the BZ. Because these high symmetry points do have symmetry requirements based on the orientations of the incident and scattered light, observing various polarizations can be expected to eliminate some of these features. It is based on this idea that the analysis in this paper is performed.

B.1 Selection rules

Γ: O_h

Excitations at the Γ-point are the only ones observable in first-order inelastic light scattering. For crystal point groups, like O_h, which have inversion symmetry, the acoustic phonons will all be Raman inactive for first order scattering. In addition, even when the crystal does not have inversion symmetry, these excitations will have nearly zero energy compared to the usual energies measured in light scattering experiments and thus cannot be typically be measured without the use of interferometers.

APPENDIX B. SELECTION RULES FOR SECOND-ORDER SCATTERING FROM O_H CRYSTALS

For O_h, the acoustic phonons have T_{1u} symmetry at Γ. Around this point, the acousitc phonons are linearly dispersive and thus no singularity, so no sharp features in the two-phonon DOS would be expected. Nonetheless we can still analyze the selection rules for second-order scattering as follows.

Raman tensors

$$A_{1g} = \begin{pmatrix} a & 0 & 0 \\ 0 & a & 0 \\ 0 & 0 & a \end{pmatrix} \tag{B.1}$$

$$E_g = \begin{pmatrix} b & 0 & 0 \\ 0 & b & 0 \\ 0 & 0 & -2b \end{pmatrix}, \begin{pmatrix} -\sqrt{3}b & 0 & 0 \\ 0 & \sqrt{3}b & 0 \\ 0 & 0 & 0 \end{pmatrix} \tag{B.2}$$

$$T_{2g} = \begin{pmatrix} 0 & d & 0 \\ d & 0 & 0 \\ 0 & 0 & 0 \end{pmatrix}, \begin{pmatrix} 0 & 0 & d \\ 0 & 0 & 0 \\ d & 0 & 0 \end{pmatrix}, \begin{pmatrix} 0 & 0 & 0 \\ 0 & 0 & d \\ 0 & d & 0 \end{pmatrix} \tag{B.3}$$

Intensities

$$I_{xx} = |a|^2 + |b|^2 + |\sqrt{3}b|^2 = |a|^2 + 4|b|^2 \tag{B.4}$$

$$I_{xy} = |d|^2 \tag{B.5}$$

$$I_{x'x'} = \frac{1}{4}|a+a|^2 + \frac{1}{4}|b+b|^2 + \frac{1}{4}|d+d|^2 = |a|^2 + |b|^2 + |d|^2 \tag{B.6}$$

$$I_{x'y'} = \frac{1}{4}| - \sqrt{3}b - \sqrt{3}b|^2 = 3|b|^2 \tag{B.7}$$

Two-phonon excitations will only involve the product of T_{1u} symmetries.

$$T_{1u} \times T_{1u} = A_{1g} + E_g + T_{1g} + T_{2g} \tag{B.8}$$

As a result, there are no restrictions on the Raman channels in which two-phonon scattering of the acoustic modes will appear, and thus scattering intensity is possible in all geometries of the experiment. This result remains effectively moot though given the large dispersion of the modes around Γ.

Γ-X: C_{4v}

There are 6 X-points within the BZ, and because only the intensity and not the phase of light is measured in scattering experiments, excitations at **q** and -**q** can be treated equivalently. This gives three independent momentum vectors to consider for excitations along the Γ-X direction: $\hat{\mathbf{q}} = (0,0,1), (0,1,0)$, and $(1,0,0)$. The acoustic phonons along this direction break into a singly degenerate A_1 longitudinal acoustic (LA) branch with atomic displacements along the $\hat{\mathbf{q}}$ direction and doubly degenerate E transverse acoustic (TA) branch with displacements perpendicular to $\hat{\mathbf{q}}$.

$\hat{\mathbf{q}} = (0,0,1)$

Raman tensors

$$A_1 = \begin{pmatrix} a & 0 & 0 \\ 0 & a & 0 \\ 0 & 0 & b \end{pmatrix} \tag{B.9}$$

$$B_1 = \begin{pmatrix} c & 0 & 0 \\ 0 & -c & 0 \\ 0 & 0 & 0 \end{pmatrix} \tag{B.10}$$

$$B_2 = \begin{pmatrix} 0 & d & 0 \\ d & 0 & 0 \\ 0 & 0 & 0 \end{pmatrix} \tag{B.11}$$

$$E = \begin{pmatrix} 0 & 0 & e \\ 0 & 0 & 0 \\ e & 0 & 0 \end{pmatrix}, \begin{pmatrix} 0 & 0 & 0 \\ 0 & 0 & e \\ 0 & e & 0 \end{pmatrix} \tag{B.12}$$

Intensities

$$I_{xx} = |a|^2 + |c|^2 \tag{B.13}$$

$$I_{xy} = |c|^2 \tag{B.14}$$

$$I_{x'x'} = \frac{1}{4}|a+a|^2 + \frac{1}{4}|d+d|^2 = |a|^2 + |d|^2 \tag{B.15}$$

$$I_{x'y'} = \frac{1}{4}|-c-c|^2 = |c|^2 \tag{B.16}$$

$\hat{\mathbf{q}} = (0, 1, 0)$

Raman tensors

$$A_1 = \begin{pmatrix} a & 0 & 0 \\ 0 & b & 0 \\ 0 & 0 & a \end{pmatrix} \tag{B.17}$$

$$B_1 = \begin{pmatrix} -c & 0 & 0 \\ 0 & 0 & 0 \\ 0 & 0 & c \end{pmatrix} \tag{B.18}$$

$$B_2 = \begin{pmatrix} 0 & 0 & d \\ 0 & 0 & 0 \\ d & 0 & 0 \end{pmatrix} \tag{B.19}$$

$$E = \begin{pmatrix} 0 & e & 0 \\ e & 0 & 0 \\ 0 & 0 & 0 \end{pmatrix}, \begin{pmatrix} 0 & 0 & 0 \\ 0 & 0 & e \\ 0 & e & 0 \end{pmatrix} \tag{B.20}$$

Intensities

$$I_{xx} = |a|^2 + |-c|^2 \tag{B.21}$$

$$I_{xy} = |e|^2 \tag{B.22}$$

$$I_{x'x'} = \frac{1}{4}|a+b|^2 + \frac{1}{4}|-c|^2 + \frac{1}{4}|e+e|^2 = \frac{|a+b|^2 + |c|^2}{4} + |e|^2 \tag{B.23}$$

$$I_{x'y'} = \frac{1}{4}|a-b|^2 + \frac{1}{4}|-c|^2 = \frac{|a-b| + |c|^2}{4} \tag{B.24}$$

$\hat{\mathbf{q}} = (1, 0, 0)$

Raman tensors

$$A_1 = \begin{pmatrix} b & 0 & 0 \\ 0 & a & 0 \\ 0 & 0 & a \end{pmatrix} \tag{B.25}$$

$$B_1 = \begin{pmatrix} 0 & 0 & 0 \\ 0 & c & 0 \\ 0 & 0 & -c \end{pmatrix} \tag{B.26}$$

$$B_2 = \begin{pmatrix} 0 & 0 & 0 \\ 0 & 0 & d \\ 0 & d & 0 \end{pmatrix} \tag{B.27}$$

$$E = \begin{pmatrix} 0 & e & 0 \\ e & 0 & 0 \\ 0 & 0 & 0 \end{pmatrix}, \begin{pmatrix} 0 & 0 & e \\ 0 & 0 & 0 \\ e & 0 & 0 \end{pmatrix} \tag{B.28}$$

Intensities

$$I_{xx} = |b|^2 \tag{B.29}$$

$$I_{xy} = |e|^2 \tag{B.30}$$

$$I_{x'x'} = \frac{1}{4}|a+b|^2 + \frac{1}{4}|c|^2 + \frac{1}{4}|e+e|^2 = \frac{|a+b|^2 + |c|^2}{4} + |e|^2 \tag{B.31}$$

$$I_{x'y'} = \frac{1}{4}|a-b|^2 + \frac{1}{4}|-c|^2 = \frac{|a-b|^2 + |c|^2}{4} \tag{B.32}$$

Summary

Scattering from the different branches of the acoustic modes can come in three varieties and would appear in the following channels.

$$\text{LA + LA: } A_1 \times A_1 = A_1 \tag{B.33}$$

$$\text{TA + TA: } E \times E = A_1 + A_2 + B_1 + B_2 \tag{B.34}$$

$$\text{LA + TA: } A_1 \times E = E \tag{B.35}$$

Thus, the contributions of each of the different types of scattering to each of the four measured polarizations can be summarized as follows.

$$\begin{aligned} I_{xx} \sim\ & (LA + LA)_{001} + (TA + TA)_{001} \\ & + (LA + LA)_{010} + (TA + TA)_{010} \\ & + (LA + LA)_{100} + (TA + TA)_{100} \end{aligned} \tag{B.36}$$

$$\begin{aligned} I_{xy} \sim\ & (TA + TA)_{001} \\ & + (LA + TA)_{010} \\ & + (LA + TA)_{100} \end{aligned} \tag{B.37}$$

$$\begin{aligned} I_{x'x'} \sim\ & (LA+LA)_{001} + (TA+TA)_{001} \\ & + (LA+LA)_{010} + (TA+TA)_{010} + (LA+TA)_{010} \\ & + (LA+LA)_{100} + (TA+TA)_{100} + (LA+TA)_{100} \end{aligned} \tag{B.38}$$

$$\begin{aligned} I_{x'y'} \sim\ & (TA+TA)_{001} \\ & + (LA+LA)_{010} + (TA+TA)_{010} \\ & + (LA+LA)_{100} + (TA+TA)_{100} \end{aligned} \tag{B.39}$$

where $(LA+LA)$ refers to scattering of a phonon from the LA branch and another one from the same branch, but at opposite $\mathbf{q}$, and the subscript ijk refers to the direction of the $\mathbf{q}$ vector.

X: D_{4h}

The addition of inversion symmetry at the X-point has the effect that only modes even under inversion will be Raman active. The polarization selection rules of these excitations are otherwise identical to the results in with the substitution $A_{1g} \to A_1,\ B_{1g} \to B_1,\ B_{2g} \to B_2$, and $E_{1g} \to E$.

M: D_{4h}

There are 12 M-points within the BZ. As with previous results, **q** and -**q** can be treated equivalently. This gives six independent momentum vectors to consider for excitations along the Γ-X direction: $\hat{\mathbf{q}} = \frac{1}{\sqrt{2}}(0,1,1)$, $\frac{1}{\sqrt{2}}(0,1,-1)$, $\frac{1}{\sqrt{2}}(1,0,1)$, $\frac{1}{\sqrt{2}}(-1,0,1)$, $\frac{1}{\sqrt{2}}(1,1,0)$, and $\frac{1}{\sqrt{2}}(1,-1,0)$. The acoustic phonons have symmetries $A_{1u} + E_u$. Here the degenerate E_u mode is comprised of a longitudinal LA and a transverse TA2 mode whereas the TA1 mode is singly degenerate A_{1u}.

$\hat{\mathbf{q}} = \frac{1}{\sqrt{2}}(0,1,1)$

Raman tensors

$$A_{1g} = \begin{pmatrix} a & 0 & 0 \\ 0 & \frac{a+b}{2} & \frac{a-b}{2} \\ 0 & \frac{a-b}{2} & \frac{a+b}{2} \end{pmatrix} \tag{B.40}$$

$$B_{1g} = \begin{pmatrix} c & 0 & 0 \\ 0 & -\frac{c}{2} & \frac{c}{2} \\ 0 & \frac{c}{2} & -\frac{c}{2} \end{pmatrix} \tag{B.41}$$

$$B_{2g} = \begin{pmatrix} 0 & \frac{d}{\sqrt{2}} & -\frac{d}{\sqrt{2}} \\ \frac{d}{\sqrt{2}} & 0 & 0 \\ -\frac{d}{\sqrt{2}} & 0 & 0 \end{pmatrix} \tag{B.42}$$

$$E_g = \begin{pmatrix} 0 & 0 & 0 \\ 0 & e & 0 \\ 0 & 0 & -e \end{pmatrix}, \begin{pmatrix} 0 & -\frac{e}{\sqrt{2}} & -\frac{e}{\sqrt{2}} \\ -\frac{e}{\sqrt{2}} & 0 & 0 \\ -\frac{e}{\sqrt{2}} & 0 & 0 \end{pmatrix} \tag{B.43}$$

Intensities

$$I_{xx} = |a|^2 + |c|^2 \tag{B.44}$$

$$I_{xy} = \frac{|d|^2 + |e|^2}{2} \tag{B.45}$$

$$\begin{aligned} I_{x'x'} &= \frac{1}{4}\left|a + \frac{a+b}{2}\right|^2 + \frac{1}{4}\left|c - \frac{c}{2}\right|^2 + \frac{1}{4}\left|\frac{2d}{\sqrt{2}}\right|^2 + \frac{1}{4}\left|\frac{2e}{\sqrt{2}}\right|^2 + \frac{1}{4}|e|^2 \\ &= \frac{|3a+b|^2 + |c|^2}{16} + \frac{|d|^2}{2} + \frac{3|e|^2}{4} \end{aligned} \tag{B.46}$$

$$I_{x'y'} = \frac{1}{4}|a-b|^2 + \frac{1}{4}|-c|^2 = \frac{|a-b|^2 + |c|^2}{4} \tag{B.47}$$

$\hat{\mathbf{q}} = \frac{1}{\sqrt{2}}(0, 1, -1)$

Intensities equivalent to $\hat{\mathbf{q}} = \frac{1}{\sqrt{2}}(0, 1, 1)$.

$\hat{\mathbf{q}} = \frac{1}{\sqrt{2}}(1, 0, 1)$

Raman tensors

$$A_{1g} = \begin{pmatrix} \frac{a+b}{2} & 0 & \frac{a-b}{2} \\ 0 & a & 0 \\ \frac{a-b}{2} & 0 & \frac{a+b}{2} \end{pmatrix} \tag{B.48}$$

$$B_{1g} = \begin{pmatrix} \frac{c}{2} & 0 & -\frac{c}{2} \\ 0 & -c & 0 \\ -\frac{c}{2} & 0 & \frac{c}{2} \end{pmatrix} \tag{B.49}$$

$$B_{2g} = \begin{pmatrix} 0 & \frac{d}{\sqrt{2}} & 0 \\ \frac{d}{\sqrt{2}} & 0 & -\frac{d}{\sqrt{2}} \\ 0 & -\frac{d}{\sqrt{2}} & 0 \end{pmatrix} \tag{B.50}$$

$$E_g = \begin{pmatrix} 0 & \frac{e}{\sqrt{2}} & 0 \\ \frac{e}{\sqrt{2}} & 0 & \frac{e}{\sqrt{2}} \\ 0 & \frac{e}{\sqrt{2}} & 0 \end{pmatrix}, \begin{pmatrix} -e & 0 & 0 \\ 0 & 0 & 0 \\ 0 & 0 & e \end{pmatrix} \tag{B.51}$$

Intensities

$$I_{xx} = \frac{|a+b|^2 + |c|^2}{4} + |e|^2 \tag{B.52}$$

$$I_{xy} = \frac{|d|^2 + |e|^2}{2} \tag{B.53}$$

$$\begin{aligned} I_{x'x'} &= \frac{1}{4}\left|\frac{a+b}{2} + a\right|^2 + \frac{1}{4}\left|\frac{c}{2} - c\right|^2 + \frac{1}{4}\left|\frac{2d}{\sqrt{2}}\right|^2 + \frac{1}{4}\left|\frac{2e}{\sqrt{2}}\right|^2 + \frac{1}{4}|-e|^2 \\ &= \frac{|3a+b|^2 + |c|^2}{16} + \frac{|d|^2}{2} + \frac{3|e|^2}{4} \end{aligned} \tag{B.54}$$

$$I_{x'y'} = \frac{1}{4}|a-b|^2 + \frac{1}{4}|-c|^2 = \frac{|a-b|^2 + |c|^2}{4} \tag{B.55}$$

$\hat{\mathbf{q}} = \frac{1}{\sqrt{2}}(-1, 0, 1)$

Intensities equivalent to $\hat{\mathbf{q}} = \frac{1}{\sqrt{2}}(1, 0, 1)$.

$\hat{\mathbf{q}} = \frac{1}{\sqrt{2}}(1,1,0)$

Raman tensors

$$A_{1g} = \begin{pmatrix} \frac{a+b}{2} & \frac{a-b}{2} & 0 \\ \frac{a-b}{2} & \frac{a+b}{2} & 0 \\ 0 & 0 & a \end{pmatrix} \tag{B.56}$$

$$B_{1g} = \begin{pmatrix} \frac{c}{2} & \frac{c}{2} & 0 \\ \frac{c}{2} & \frac{c}{2} & 0 \\ 0 & 0 & -c \end{pmatrix} \tag{B.57}$$

$$B_{2g} = \begin{pmatrix} 0 & 0 & -\frac{d}{\sqrt{2}} \\ 0 & 0 & -\frac{d}{\sqrt{2}} \\ -\frac{d}{\sqrt{2}} & -\frac{d}{\sqrt{2}} & 0 \end{pmatrix} \tag{B.58}$$

$$E_g = \begin{pmatrix} 0 & 0 & \frac{e}{\sqrt{2}} \\ 0 & 0 & -\frac{e}{\sqrt{2}} \\ \frac{e}{\sqrt{2}} & -\frac{e}{\sqrt{2}} & 0 \end{pmatrix} \begin{pmatrix} e & 0 & 0 \\ 0 & -e & 0 \\ 0 & 0 & 0 \end{pmatrix} \tag{B.59}$$

Intensities

$$I_{xx} = \frac{|a+b|^2 + |c|^2}{4} + |e|^2 \tag{B.60}$$

$$I_{xy} = \frac{|a-b|^2 + |c|^2}{4} \tag{B.61}$$

$$\begin{aligned} I_{x'x'} &= \frac{1}{4}|a+b+a-b|^2 + \frac{1}{4}\left|\frac{4c}{2}\right|^2 + \frac{1}{4}|e-e|^2 \\ &= \frac{|a|^2}{4} + |c|^2 \end{aligned} \tag{B.62}$$

$$I_{x'y'} = |e|^2 \tag{B.63}$$

$\hat{\mathbf{q}} = \frac{1}{\sqrt{2}}(1,-1,0)$

Raman tensors

$$A_{1g} = \begin{pmatrix} \frac{a+b}{2} & \frac{-a+b}{2} & 0 \\ \frac{-a+b}{2} & \frac{a+b}{2} & 0 \\ 0 & 0 & a \end{pmatrix} \tag{B.64}$$

$$B_{1g} = \begin{pmatrix} \frac{c}{2} & -\frac{c}{2} & 0 \\ -\frac{c}{2} & \frac{c}{2} & 0 \\ 0 & 0 & -c \end{pmatrix} \tag{B.65}$$

$$B_{2g} = \begin{pmatrix} 0 & 0 & -\frac{d}{\sqrt{2}} \\ 0 & 0 & \frac{d}{\sqrt{2}} \\ -\frac{d}{\sqrt{2}} & \frac{d}{\sqrt{2}} & 0 \end{pmatrix} \tag{B.66}$$

$$E_g = \begin{pmatrix} 0 & 0 & -\frac{e}{\sqrt{2}} \\ 0 & 0 & -\frac{e}{\sqrt{2}} \\ -\frac{e}{\sqrt{2}} & -\frac{e}{\sqrt{2}} & 0 \end{pmatrix} \begin{pmatrix} -e & 0 & 0 \\ 0 & e & 0 \\ 0 & 0 & 0 \end{pmatrix} \tag{B.67}$$

Intensities

$$I_{xx} = \frac{|a+b|^2 + |c|^2}{4} + |e|^2 \tag{B.68}$$

$$I_{xy} = \frac{|a-b|^2 + |c|^2}{4} \tag{B.69}$$

$$\begin{aligned} I_{x'x'} &= \frac{1}{4}|a+b-a+b|^2 + \frac{1}{4}\left|\frac{2c}{2}-\frac{2c}{2}\right|^2 + \frac{1}{4}|e-e|^2 \\ &= \frac{|b|^2}{4} \end{aligned} \tag{B.70}$$

$$I_{x'y'} = |e|^2 \tag{B.71}$$

Summary

The doubly degenerate mode will be denoted $LA/TA2$ and the singly degenerate $TA1$. Again we have three possible symmetries of second order excitations.

$$\text{TA1 + TA1: } A_{1u} \times A_{1u} = A_{1g} \tag{B.72}$$

$$\text{LA/TA2 + LA/TA2: } E_u \times E_u = A_{1g} + A_{2g} + B_{1g} + B_{2g} \tag{B.73}$$

$$\text{TA1 + LA/TA2: } A_{1u} \times E_u = E_g \tag{B.74}$$

$$\begin{aligned} I_{xx} \sim\ & (TA1+TA1)_{011} + (LA/TA2+LA/TA2)_{011} \\ & + (TA1+TA1)_{101} + (LA/TA2+LA/TA2)_{101} + (TA1+LA/TA2)_{101} \\ & + (TA1+TA1)_{110} + (LA/TA2+LA/TA2)_{110} + (TA1+LA/TA2)_{110} \\ & + (TA1+TA1)_{1\bar{1}0} + (LA/TA2+LA/TA2)_{1\bar{1}0} + (TA1+LA/TA2)_{1\bar{1}0} \end{aligned} \tag{B.75}$$

$$\begin{aligned} I_{xy} \sim & (LA/TA2 + LA/TA2)_{011} + (TA1 + LA/TA2)_{011} \\ & + (LA/TA2 + LA/TA2)_{101} + (TA1 + LA/TA2)_{101} \\ & + (TA1 + TA1)_{110} + (LA/TA2 + LA/TA2)_{110} \\ & + (TA1 + TA1)_{1\bar{1}0} + (LA/TA2 + LA/TA2)_{1\bar{1}0} \end{aligned} \tag{B.76}$$

$$\begin{aligned} I_{x'x'} \sim & (TA1 + TA1)_{011} + (LA/TA2 + LA/TA2)_{011} + (TA1 + LA/TA2)_{011} \\ & + (TA1 + TA1)_{101} + (LA/TA2 + LA/TA2)_{101} + (TA1 + LA/TA2)_{101} \\ & + (TA1 + TA1)_{110} + (LA/TA2 + LA/TA2)_{110} \\ & + (LA/TA2 + LA/TA2)_{1\bar{1}0} \end{aligned} \tag{B.77}$$

$$\begin{aligned} I_{x'y'} \sim & (TA1 + TA1)_{011} + (LA/TA2 + LA/TA2)_{011} \\ & + (TA1 + TA1)_{101} + (LA/TA2 + LA/TA2)_{101} \\ & + (TA1 + LA/TA2)_{110} \\ & + (TA1 + LA/TA2)_{1\bar{1}0} \end{aligned} \tag{B.78}$$

$$\tag{B.79}$$

R: O_h

All R points have no preferred direction, and thus the selection rules follows those for the Γ-point. The acoustic phonons have symmetry T_{1u}, and thus as was shown for the Γ-point scattering intensity will appear in all polarizations.

B.2 Experiment: SmB_6

To illistrate the understanding of experimental results, two-phonon scattering in Raman spectra of SmB_6 can be analyzed.

As shown in the previous section, the strongest polarization selection rules come from the Γ-X direction, and thus gives the most clear picture as to the polarization dependence observed experimentally.

The xx polarization spectrum shows a broad feature at ∼165 cm^{-1} and a narrow feature at ∼185 cm^{-1}. Section B.1 shows that only overtone scattering will be observed from Γ-X phonons in this symmetry. Along this direction the LA branch is not very dispersive meaning the two-phonon DOS would be expected to have a very narrow peak around where it is seen in the Raman spectrum (185 cm^{-1}). Additionally, $TA+TA$ overtone scattering will occur at lower energies, and with a larger dispersion seen over the later half of the BZ which comprises the majority of the weight of the DOS. This can be seen as the broader low energy peak in the Raman spectrum.

The symmetry requirements for xy polarization restrict the appearance of $LA+LA$

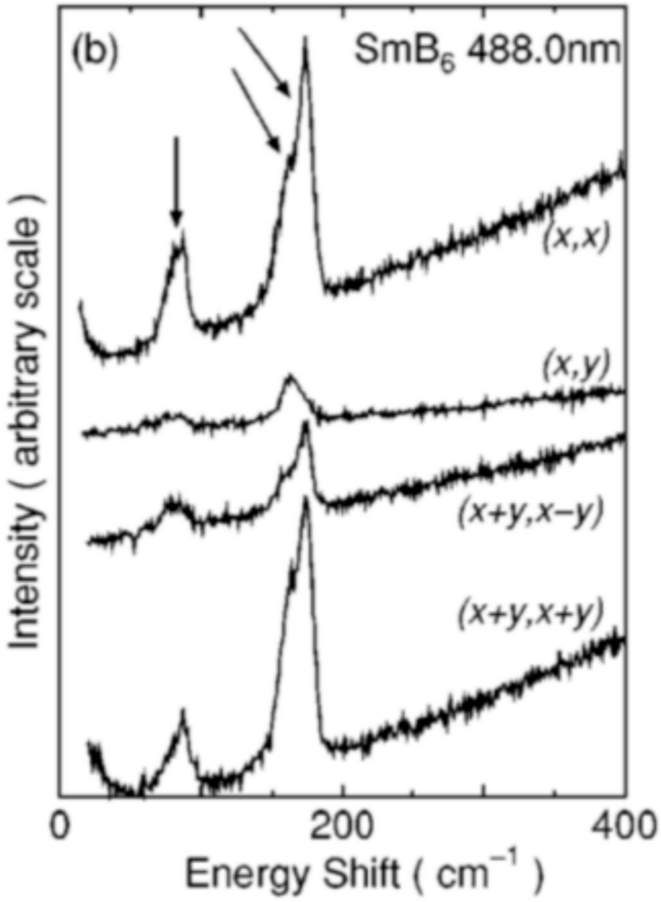

Figure B.1: Raman spectra of $\mathrm{SmB_6}$ for polarizations xx, xy, $x'x'$, and $x'y'$. Figure from Reference 4

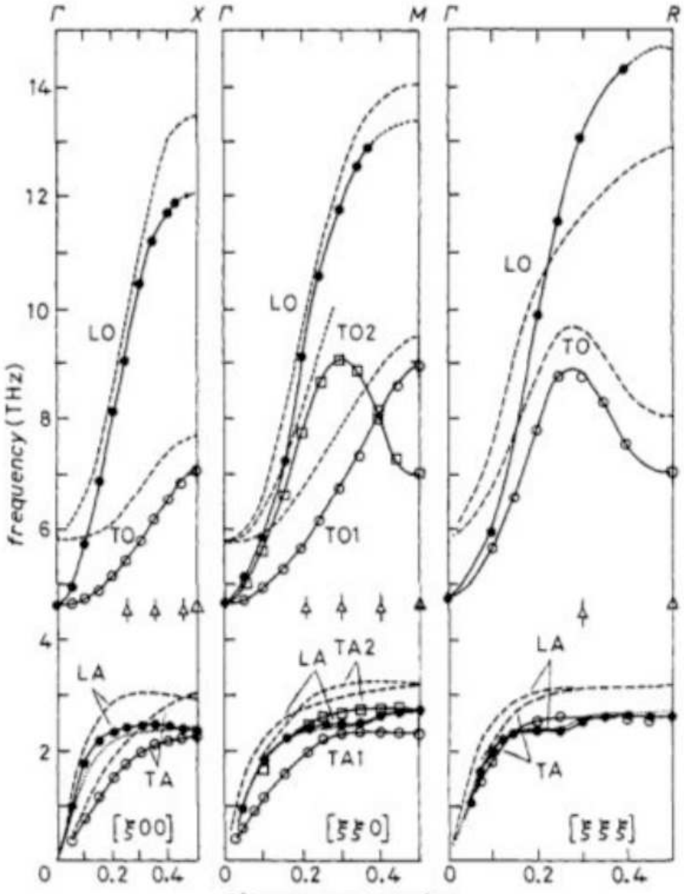

Figure B.2: Phonon dispersion curves for SmB_6. Figure from Reference 5 scattering which was responsible for the higher energy narrow peak seen in xx. This is seen in the spectrum where a weaker broad peak coincides with the broad peak seen in other polarizations. Additionaly, scattering involving both branches $LA+TA$ is allowed in this polarization. No sharp peaks shuold result here again because there are no van Hove singularities as would come from solutions to Eqn. 2.13.

$x'x'$ polarization is very similar to xx polarization except that LA+TA scattering is now allowed. This would results in additional spectral weight at energies between the peaks of the overtone scattering as is seen in Fig. B.1.

Finally, $x'y'$ allows only overtone scattering like xx, and it's relative shape is very nearly in agreement with xx.

Looking instead at the M-point and by extension the Γ-M direction, we see that in all polarizations almost all of the possible combinations of excitations are present, though not necessarily for all different directions of the dispersion. This means that one would expect a less significant effect on the polarization dependence to arise from these symmetry requirements. Nonetheless, it is worth mentioning that the two-phonon spectra do seem to contrast these expectations for certain polarizations. For example, xy polarization should allow overtone scattering from the $LA/TA2$ branch, and yet no high energy peak is observed. This is likely due to the fact that the symmetry of the excitations is lower away from the M-point and this branch is actually split into nondegenerate branches. This may be an explanation for why no clear peak is seen.

Appendix C

Vibrational Raman effects due to surface imperfections and introduced impurities in SmB_6

C.1 Introduction

The two primary methods for synthesizing crystals of SmB_6 are the optical floating zone (FZ) and Al flux techniques. Experimental results from crystals of each of these methods are often compared interchangeably without consideration for structural differences that may be present and the differences in electronic properties that result. We showed in Chapter 5 the sensitivity of the hybridization gap to less than 1% Sm vacancies that are known to be present in FZ samples. In this appendix, we detail the structural differences found between samples of different growth techniques and dopings through Raman spectroscopy along with the effects of surface imperfections on the scattering response.

C.2 Symmetry selection rules

SmB_6 belongs to the $Pm\bar{3}m$ cubic symmetry space group which has O_h symmetry at the Γ-point relevant for Raman scattering. This point group contains the inversion operation which means the phonons will be either IR active (odd under inversion) or Raman active (even under inversion). The full Γ-point representation for single phonon excitations is $\Gamma = A_{1g} + E_g + T_{2g} + 3T_{1u}$, where one T_{1u} mode is acoustic and the rest are optical. Motion of the two inversion centers, the Sm ion and the center of the B_6 octahedra, is forbidden in first order Raman active excitations. The eigenvectors of the Raman active modes are given in Fig. C.1 which involve distortions of the B_6 octahedra.

C.3 First-order Raman phonons

A variety of different samples grown FZ method by Seyed Koohpayeh, Adam Phelan, and Tyrel McQueen and Al flux method by Priscila F. S. Rosa and Zachary Fisk were investigated with several different dopants. The IQM samples observed were all grown using the FZ method described in References 59 and 74. Four of these

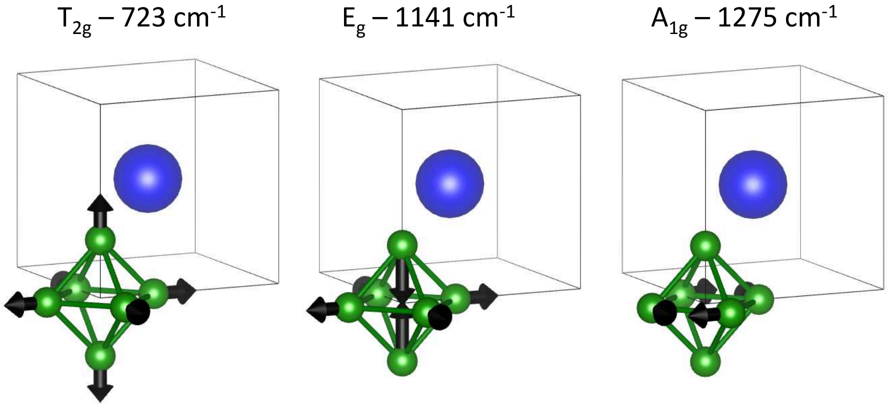

Figure C.1: First order Raman allowed eigenvectors for SmB_6.

samples will be characterized here: Pure, Sm deficient, Al doped and C doped. The FZ grown crystals were found to exhibit some degree of Sm deficiency that varied systematically across the length of the crystal observed both as a change in lattice parameters from x-ray diffraction[74] and an increase in symmetry forbidden Raman defect scattering.[92] The Pure and Sm deficient samples were taken from opposite ends of the same crystal to demonstrate the effect of Sm vacancies on the electronic properties of SmB_6. Estimates based on lattice parameters suggest that there is less than a 1% variation in Sm content between the two, however this is significant enough to observe both an increase in defect scattering and changes in the opening of the hybridization gap.[92] The other two samples were synthesized in order to study the effects of possible impurities in SmB_6 crystals by introducing Al and C during

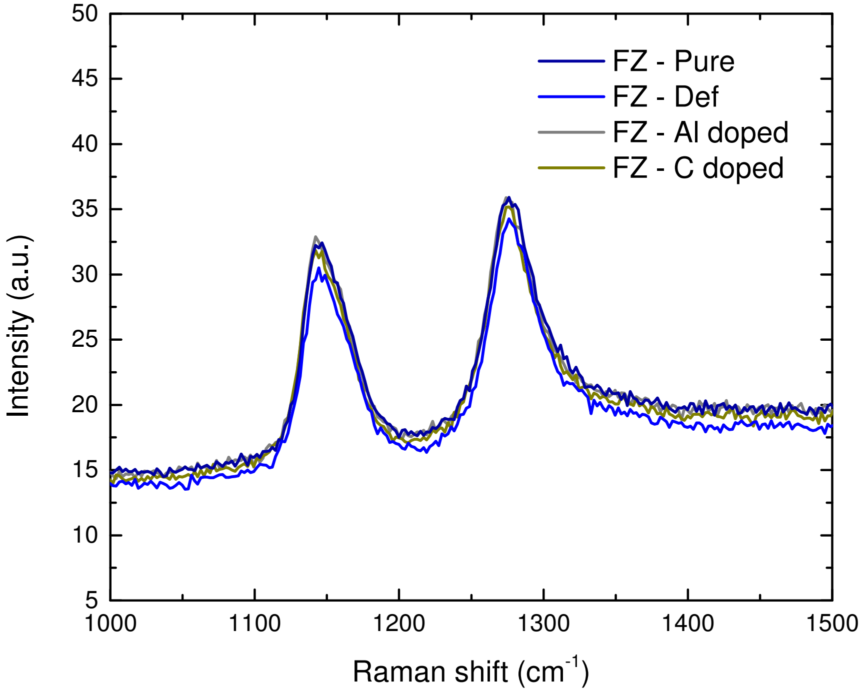

Figure C.2: *xx* polarized Raman spectra for IQM floating zone samples. E_g (1141 cm^{-1}) and A_{1g} (1275 cm^{-1}) phonons are observed in this polarization both with broad and asymmetric shapes that arise from electron-phonon coupling.

the growth phase. The Al doped samples reproduce the effects of Al impurities in found in some Al flux grown crystals,[74] and C doped samples demonstrate the effects of contamination of boron sites with carbon. The degree of doping could not be accurately characterized for these crystals.[59]

Figure C.2 shows the Raman scattering observed from the E_g (1141 cm^{-1}) and A_{1g} (1275 cm^{-1}) modes for the different samples measured. These two modes in particular show very broad and asymmetric lineshapes that results from electron-phonon coupling in SmB_6, which is characteristic to varying degrees of all SmB_6

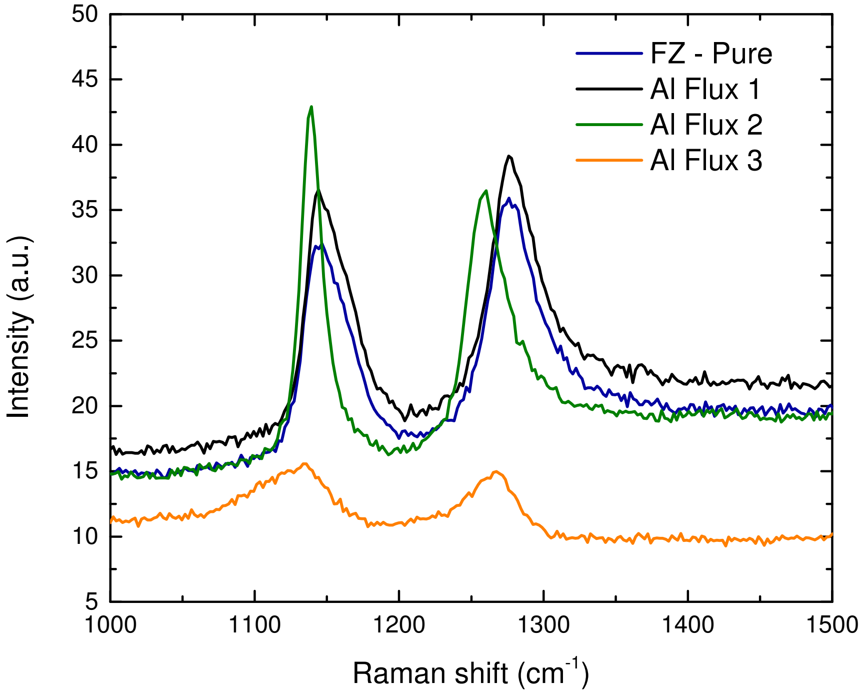

Figure C.3: *xx* polarized Raman phonon spectrum of Al flux grown SmB_6 samples with IQM FZ grown sample included for comparison.

samples observed in this study. The four samples shown as well as all IQM FZ samples with surfaces prepared by cleaving show no variation the frequency, width, or lineshape of the first-order phonons, including the T_{2g} mode (not pictured). These four samples came from three separate crystal growths indicating a very consistent crystal growth technique but also suggests minimal presence of impurities in the doped samples.

Al flux grown samples show a much more significant variation in these first-order phonons from batch to batch and even perhaps within a single sample, though this may in part be attributable to sample surface quality which is discussed later. Three of these samples are shown in Figures C.3 and C.4 along with the pure IQM sample for comparison. The Al Flux 1 sample has phonons that match up very well with the IQM FZ samples and as a result was chosen for comparing low temperature electronic Raman scattering,[92] detailed in Chapter 5. The other two samples showed significantly different behavior among these phonons. The Al Flux 2 sample has phonons shifted to lower energies and reduced damping. The shift in the energy of the T_{2g} (723 $\mathrm{cm^{-1}}$) has been shown to correlate with the cation charge in other hexaborides[4,80] and may here be an indication of a greater average charge of the Sm ion, ie. more $\mathrm{Sm^{3+}}$, for this sample. Additionally, this shift in energies matches the spectrum of isotope enriched $\mathrm{B^{11}}$ samples used for neutron scattering measurements. The Al Flux 3 sample here displays quite a dramatic deviation from the other samples measured. The first order phonons show a drop intensity and broadened phonons which are also shifted to lower energies. Such effects are consistent with other samples measured that have poor crystalline structure such as thin films or coarsely polished surfaces. Because visible light only penetrates $\mathrm{SmB_6}$ on the order of 100 nm and the spot size of the incident laser was about 2 μm in diameter, it is possible that this observed disorder is local to only the region of the sample measured and not indicative of the crystal as a whole. Additionally, the Al flux growth process involves chemical etching of the Al flux from the surface of the sample, and this may affect the surface quality of the sample leading to spatial variations.

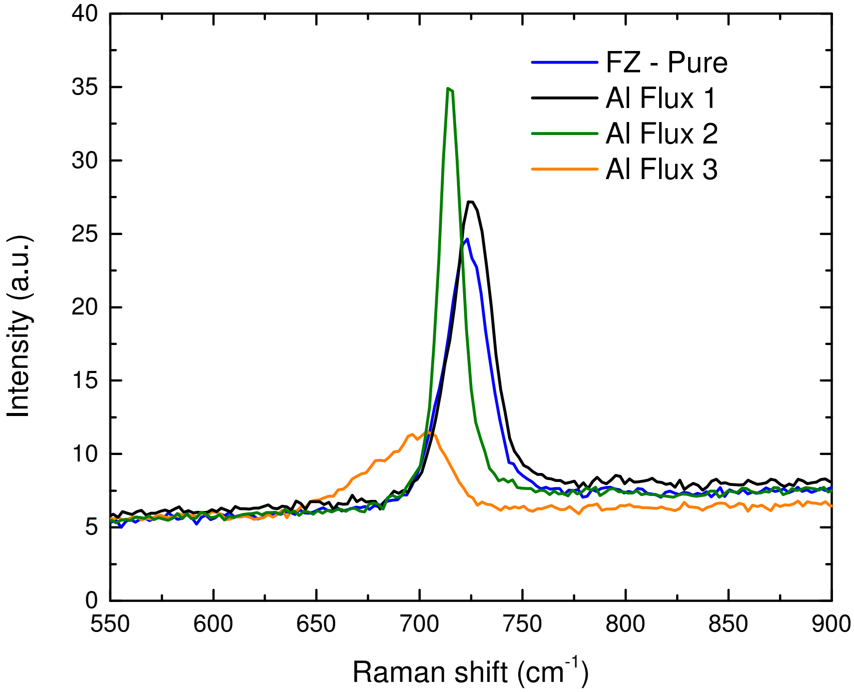

Figure C.4: *xy* polarized Raman phonon spectrum of different Al flux grown SmB_6 samples with IQM FZ grown sample included for comparison.

Fig. C.5 gives a comparison of the first order phonon frequencies and widths for Al flux and floating zone grown crystals. The phonon modes that correspond to certain data points are indicated by phonon symmetries. The samples shown in this figure all had what appeared to be high quality cleaved surfaces, such that these differences are believed to be inherent to the crystal structure. Also note that the poorly crystalline Al flux sample (A11) is not currently included as one of these data points. The FZ crystals show very little variation in phonon frequency, less than 3 cm^{-1}, even in the presence of doping and Sm deficiency. The Al flux crystals on the other hand showed as much as a 15 cm^{-1} frequency shift in the case of the T_{2g} mode. There is also a greater spread in the observed widths of the phonons for the Al flux crystals and a slight tendency for narrower phonons. Disorder will typically have the effect of broadening phonons, however in SmB_6 valence fluctuations and electron-phonon coupling will also affect the phonon width and lineshape which makes decoupling the ultimate cause of these differences in width difficult. The defect phonon discussed in Sec. C.4 provides a more clear picture of the disorder in the samples and shows little correlation with the phonon frequencies shown here.

C.4 Defect phonon

Along with the first-order symmetry-allowed Raman-active modes two additional narrow features can be observed in the Raman spectrum at 85 and 170 cm^{-1}(Figure C.6).

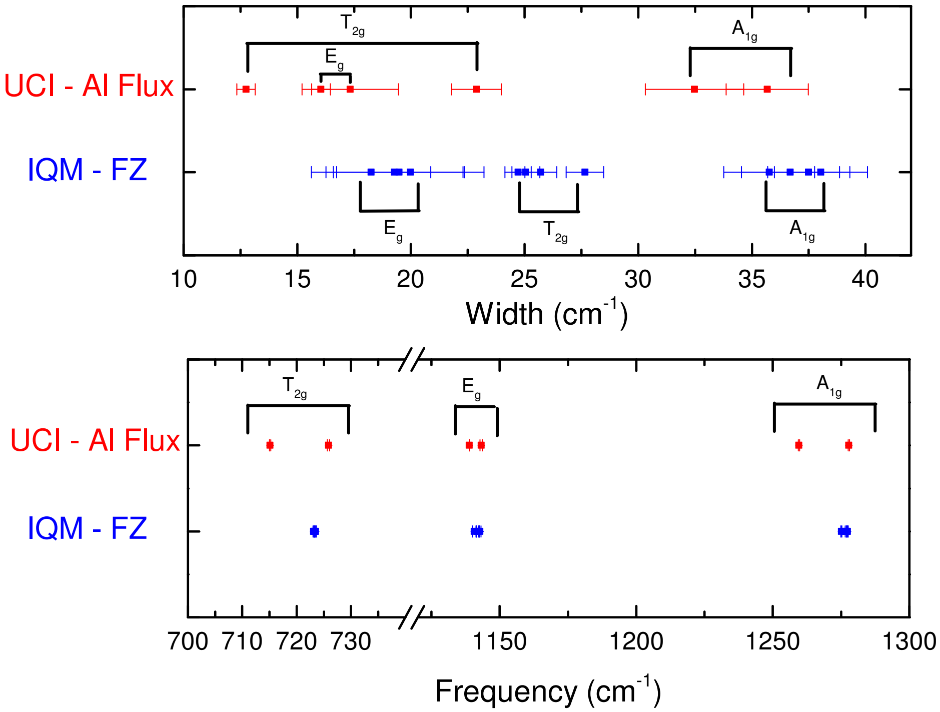

Figure C.5: Variation in first order phonon frequencies and widths seen in Al flux and floating zone grown crystals.

The higher energy peak arises from two-phonon scattering of the acoustic phonon branches. The momentum of a photon in the visible range is negligible in comparison to the crystal Brillouin zone, and thus Raman scattering from single particle excitation is limited to the Γ-point. Momentum conservation for two-particle excitations merely requires that the particles have opposite momentum for visible light scattering. As a result scattering arises from throughout the BZ as a weighted average of the two-phonon density of states, and due to the lowered symmetry of an arbitrary **q**-vector many of the symmetry selection rules for inelastic light scattering are relaxed. Nonetheless, peaks are observed in the spectrum where Van Hove singularities (Equation C.1) occur which often lie at high symmetry points leading to a Raman scattering polarization dependence. This polarization dependence is detailed in Appendix B based on the measured phonon dispersion for SmB_6 and is in good agreement with experimental results.

$$\nabla_{\mathbf{q}}(\omega_{\sigma\mathbf{q}} + \omega_{\sigma'\mathbf{q}}) = 0 \tag{C.1}$$

While two-phonon scattering arises in SmB_6 at twice the energy of the flat acoustic phonon bands at 85 cm^{-1}due to two phonons being excited, the 85 cm^{-1} mode arises from a single phonon excitation where momentum conservation has been broken by the presence of a crystal defect, and thus scattering from throughout the BZ is allowed. Such defect-induced scattering can come about from any change in the crystal lattice and provides an excellent probe of disorder within the crystal.

Figure C.6 shows these two modes for a variety of crystals. A trend of increasing intensity of the defect-induced phonon can be traced along the length of a FZ crystal where increasing numbers of Sm vacancies are known to occur. The Al and C doped samples also show a slight increase in intensity of the defect-induced phonon though this modest increase in comparison to the FZ - Pure crystal is likely indication that little doping is actually present in the crystal. This is further in agreement with low temperature measurements of the electronic spectrum in the samples which show little deviation from the pure FZ sample. The Al Flux 1 sample shows very weak defect scattering at 85 $\mathrm{cm^{-1}}$ and as a result is the most crystallographically pure of the samples measured as any deviation from the $\mathrm{SmB_6}$ structure would lead to intensity here. This sample showed the most intense spin-exciton at low temperatures and the clearest signature of the opening of the hybridization gap.[92]

C.5 Raman surface preparation

Because $\mathrm{SmB_6}$ is metallic, visible light only penetrates into the sample on the order 100 nm which means Raman scattered light only observes this area very near to the surface. As a result sample surface quality was found to be of extreme importance to the measured Raman spectrum. Polishing was done with 1 μm sand paper and introduces surface imperfections on that scale. Thus polished samples will have a significant presence of disorder due to the unsatisfactory surface quality. The

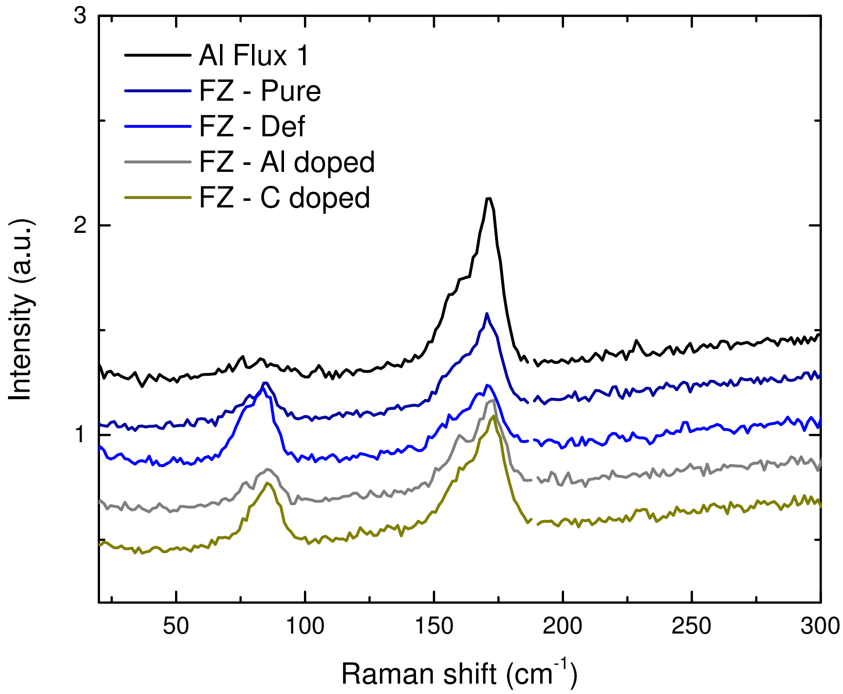

Figure C.6: Low frequency room temperature spectrum of FZ and Al flux SmB_6 samples. Two symmetry forbidden peaks are observed in all spectra at 85 and 170 cm^{-1} corresponding to defect-induced and two-phonon scattering respectively.

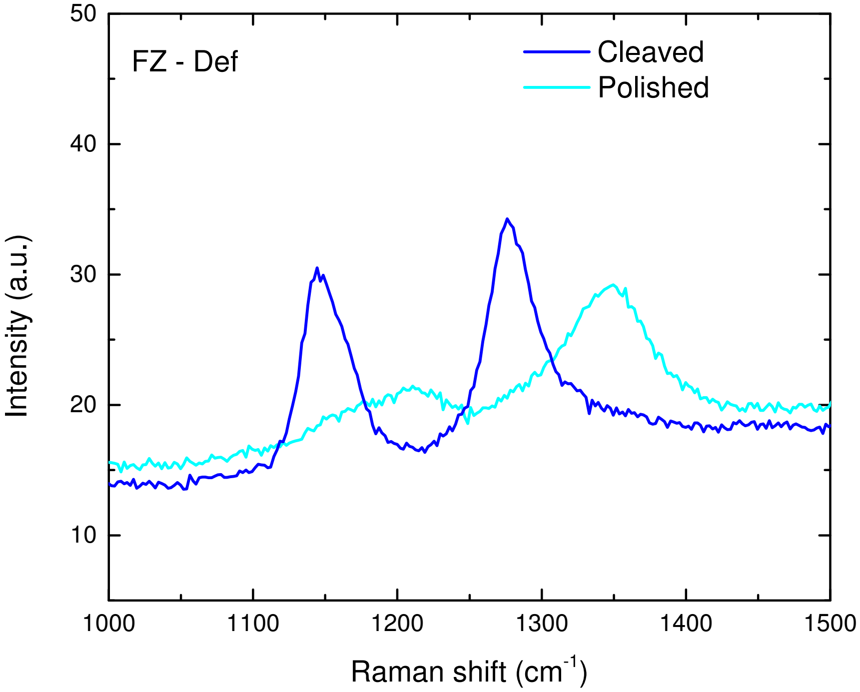

Figure C.7: A_{1g} and E_g phonons for samples from the same crystal growth prepared by both cleaving and polishing. Polishing is seen here to significantly shift the phonons to higher frequencies and broaden them.

100 nm penetration depth means that Raman scattering is only observing the rough and disordered portion of the crystal near the surface. This effect is seen in the Raman spectra of polished versus cleaved samples, Figure C.7, where the A_{1g} and E_g phonon modes have been shifted to higher energies by about 30 cm^{-1} and a significant broadening has occurred which is a clear sign of a disorder crystal. A similar sensitivity to surface quality for Raman scattering measurements has been observed previously in carbides.[86,87]

These effects also appear to be present in polished versus naturally cleaved surfaces

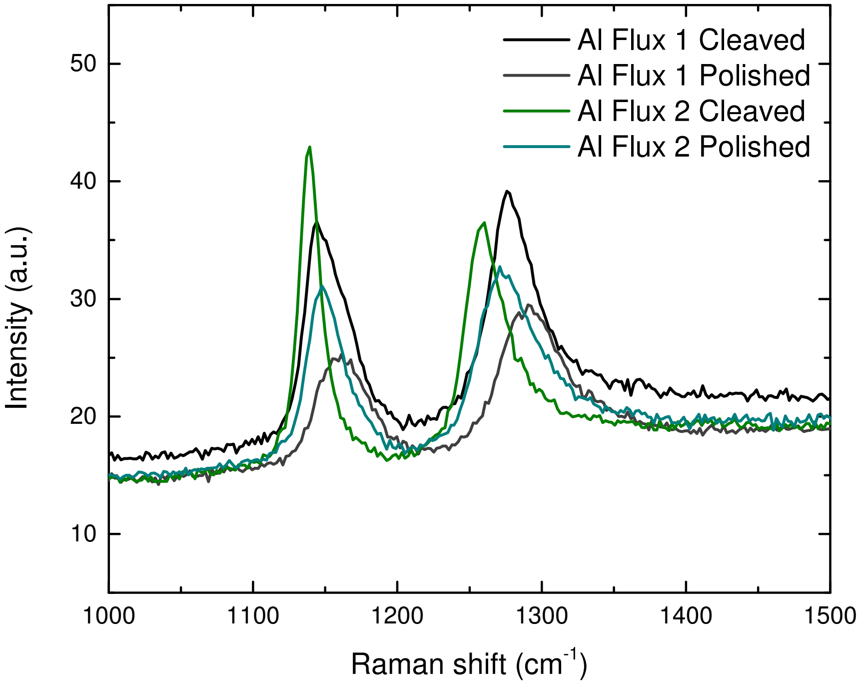

Figure C.8: A_{1g} and E_g phonons for different positions on the Al flux grown crystals that appear to polished or naturally cleaved.

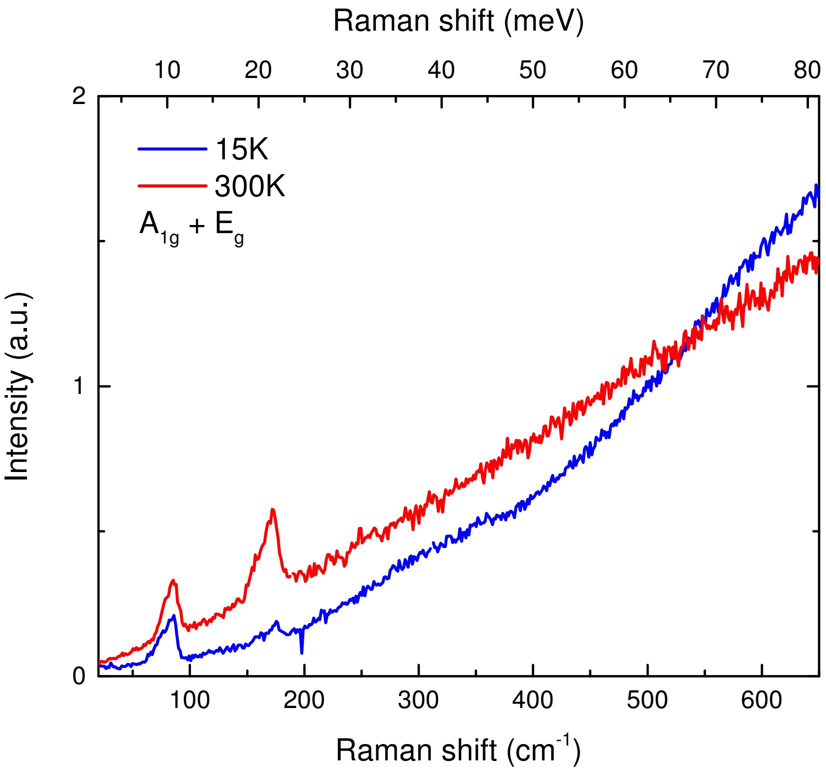

Figure C.9: Cleaved FZ SmB_6 - Sm deficient sample measured both below and above the opening of the hybridization gap. xx polarization T64000 Macro triple monochromator, 514 nm.

of the Al flux samples, Figure C.8. The two spectra for each sample are representative of different positions on the same sample where surfaces appear to either come about from polishing or natural cleaving. Of note is that while the effects are not as drastic as are observed in the FZ sample (likely due to a higher quality polishing), there nonetheless is a tendency for a shift to higher frequencies in polished surfaces and broadened, lower peak intensity phonons.

Low temperature measurements of the cleaved FZ SmB_6 Pure sample shows the opening of the hybridization gap as a suppression of electronic scattering below en-

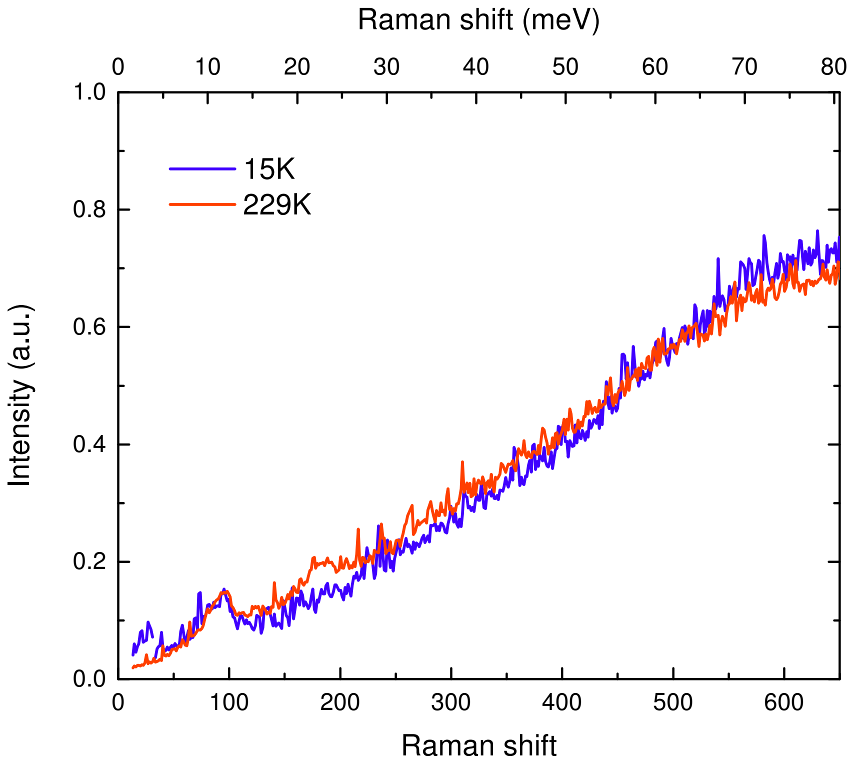

Figure C.10: Polished FZ SmB_6 - Sm deficient sample measured both below and above the opening of the hybridization gap, however polishing has introduced sufficient disorder to suppress its appearance. *xx* polarization T64000 Macro triple monochromator, 514 nm.

ergies of about 120 cm^{-1} and a redistribution of electronic spectral weight to higher energies where peaks arise from singularities in the joint density of states of interband electronic transitions (Figure C.9). Figure C.10 shows how this gap opening is suppressed in a sample from the same growth that was instead prepared by polishing. It is likely that the hybridization gap still opens in the same manner well within the bulk, but the disorder near the surface leads to conduction that appears in the low frequency Raman spectrum.

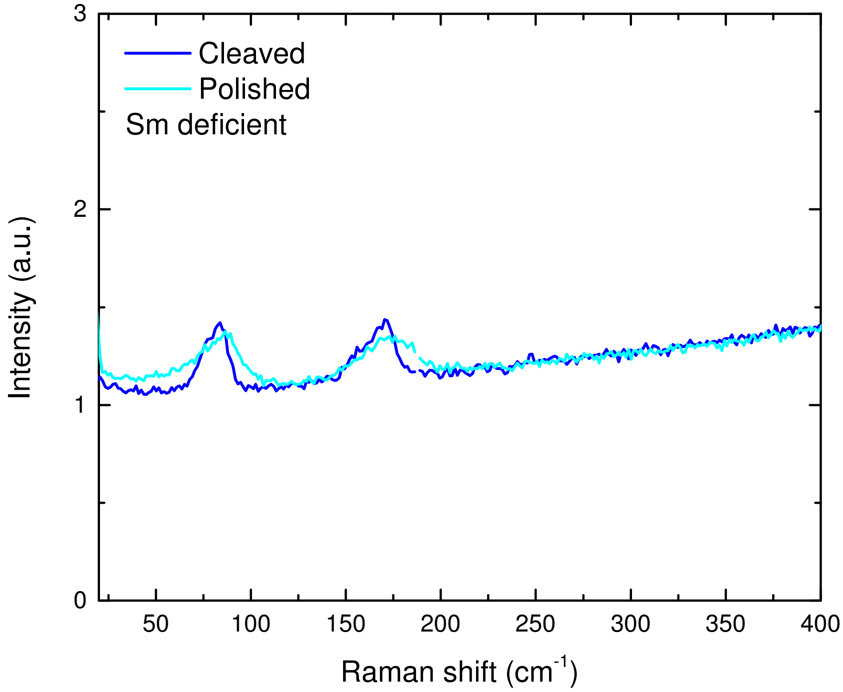

Figure C.11: Comparison of defect phonon of SmB$_6$ - Sm deficient defect phonon for Polished and Cleaved samples. Polishing leads to a broadening and slight shift to higher energies though not as dramatic as B_6 phonons.

Bibliography

[1] M. E. Valentine, S. Koohpayeh, M. Mourigal, T. M. McQueen, C. Broholm, N. Drichko, S. E. Dutton, R. J. Cava, T. Birol, H. Das, and C. J. Fennie, "Raman study of magnetic excitations and magnetoelastic coupling in α-$SrCr_2O_4$," *Phys. Rev. B*, vol. 91, p. 144411, Apr 2015. [Online]. Available: https://link.aps.org/doi/10.1103/PhysRevB.91.144411

[2] S. Toth, B. Lake, S. A. J. Kimber, O. Pieper, M. Reehuis, A. T. M. N. Islam, O. Zaharko, C. Ritter, A. H. Hill, H. Ryll, K. Kiefer, D. N. Argyriou, and A. J. Williams, "120° helical magnetic order in the distorted triangular antiferromagnet α-$CaCr_2O_4$," *Phys. Rev. B*, vol. 84, p. 054452, Aug 2011. [Online]. Available: http://link.aps.org/doi/10.1103/PhysRevB.84.054452

[3] S. E. Dutton, E. Climent-Pascual, P. W. Stephens, J. P. Hodges, A. Huq, C. Broholm, and R. Cava, "Helical magnetism and structural anomalies in triangular lattice α-$SrCr_2O_4$," *Journal of Physics: Condensed Matter*, vol. 23, no. 24, p. 246005, 2011.

[4] N. Ogita, S. Nagai, N. Okamoto, M. Udagawa, F. Iga, M. Sera, J. Akimitsu, and S. Kunii, "Raman scattering investigation of $R\mathrm{B}_6$ (R = Ca, La, Ce, Pr, Sm, Gd, Dy, and Yb)," *Phys. Rev. B*, vol. 68, p. 224305, Dec 2003. [Online]. Available: http://link.aps.org/doi/10.1103/PhysRevB.68.224305

[5] P. A. Alekseev, A. S. Ivanov, B. Dorner, H. Schober, K. A. Kikoin, A. S. Mishchenko, V. N. Lazukov, E. S. Konovalova, Y. B. Paderno, A. Y. Rumyantsev, and I. P. Sadikov, "Lattice dynamics of intermediate valence semiconductor SmB_6," *Europhysics Letters*, vol. 10, no. 5, p. 457, 1989. [Online]. Available: http://stacks.iop.org/0295-$\mathrm{SmB}_6$5075/10/i=5/a=012

[6] L. C. Chapon, P. Manuel, F. Damay, P. Toledano, V. Hardy, and C. Martin, "Helical magnetic state in the distorted triangular lattice of α-$\mathrm{CaCr_2O_4}$," *Phys. Rev. B*, vol. 83, p. 024409, Jan 2011. [Online]. Available: http://link.aps.org/doi/10.1103/PhysRevB.83.024409

[7] S. Toth, B. Lake, K. Hradil, T. Guidi, K. C. Rule, M. B. Stone, and A. T. M. N. Islam, "Magnetic soft modes in the distorted triangular antiferromagnet α-$\mathrm{CaCr_2O_4}$," *Phys. Rev. Lett.*, vol. 109, p. 127203, Sep 2012. [Online]. Available: http://link.aps.org/doi/10.1103/PhysRevLett.109.127203

[8] D. A. Huse and V. Elser, "Simple variational wave functions for two-dimensional Heisenberg spin-$\frac{1}{2}$ antiferromagnets," *Phys. Rev. Lett.*, vol. 60, pp. 2531–2534,

Jun 1988. [Online]. Available: http://link.aps.org/doi/10.1103/PhysRevLett.60.2531

[9] L. Capriotti, A. E. Trumper, and S. Sorella, “Long-range Néel order in the triangular Heisenberg model,” *Phys. Rev. Lett.*, vol. 82, pp. 3899–3902, May 1999. [Online]. Available: http://link.aps.org/doi/10.1103/PhysRevLett.82.3899

[10] S. Nakatsuji, Y. Nambu, H. Tonomura, O. Sakai, S. Jonas, C. Broholm, H. Tsunetsugu, Y. Qiu, and Y. Maeno, “Spin disorder on a triangular lattice,” *Science*, vol. 309, no. 5741, pp. 1697–1700, 2005. [Online]. Available: http://science.sciencemag.org/content/309/5741/1697

[11] R. Coldea, D. A. Tennant, and Z. Tylczynski, “Extended scattering continua characteristic of spin fractionalization in the two-dimensional frustrated quantum magnet Cs_2CuCl_4 observed by neutron scattering,” *Phys. Rev. B*, vol. 68, p. 134424, Oct 2003. [Online]. Available: http://link.aps.org/doi/10.1103/PhysRevB.68.134424

[12] J. P. Sheckelton, J. R. Neilson, D. G. Soltan, and T. M. McQueen, “Possible valence-bond condensation in the frustrated cluster magnet $LiZn_2Mo_3O_8$,” *Nature Materials*, vol. 11, no. 6, pp. 493–496, 2012. [Online]. Available: http://dx.doi.org/10.1038/nmat3329

[13] L. Zhao, T.-W. Lan, K.-J. Wang, C.-H. Chien, T.-L. Hung, J.-Y. Luo, W.-H. Chao, C.-C. Chang, Y.-Y. Chen, M.-K. Wu, and C. Martin,

"Multiferroicity in geometrically frustrated α-$M\mathrm{Cr}_2\mathrm{O}_4$ systems (M = Ca, Sr, Ba)," *Phys. Rev. B*, vol. 86, p. 064408, Aug 2012. [Online]. Available: http://link.aps.org/doi/10.1103/PhysRevB.86.064408

[14] C. Stock, S. Jonas, C. Broholm, S. Nakatsuji, Y. Nambu, K. Onuma, Y. Maeno, and J.-H. Chung, "Neutron-scattering measurement of incommensurate short-range order in single crystals of the $S = 1$ triangular antiferromagnet $\mathrm{NiGa}_2\mathrm{S}_4$," *Phys. Rev. Lett.*, vol. 105, p. 037402, Jul 2010. [Online]. Available: http://link.aps.org/doi/10.1103/PhysRevLett.105.037402

[15] M. König, S. Wiedmann, C. Brüne, A. Roth, H. Buhmann, L. W. Molenkamp, X.-L. Qi, and S.-C. Zhang, "Quantum spin Hall insulator state in HgTe quantum wells," *Science*, vol. 318, no. 5851, pp. 766–770, 2007. [Online]. Available: http://science.sciencemag.org/content/318/5851/766

[16] D. Hsieh, D. Qian, L. Wray, Y. Xia, Y. S. Hor, R. J. Cava, and M. Z. Hasan, "A topological Dirac insulator in a quantum spin Hall phase," *Nature*, vol. 452, pp. 970–974, 2008. [Online]. Available: http://www.nature.com/nature/journal/v452/n7190/suppinfo/nature06843_S1.html

[17] M. Dzero, K. Sun, V. Galitski, and P. Coleman, "Topological Kondo insulators," *Phys. Rev. Lett.*, vol. 104, p. 106408, Mar 2010. [Online]. Available: http://link.aps.org/doi/10.1103/PhysRevLett.104.106408

[18] R. Loudon, *The Quantum Theory of Light.* Oxford University Press, 1973.

[19] P. Fleury and R. Loudon, “Scattering of light by one-and two-magnon excitations,” *Physical Review*, vol. 166, no. 2, p. 514, 1968.

[20] T. Jolicoeur and J. C. Le Guillou, “Spin-wave results for the triangular Heisenberg antiferromagnet,” *Phys. Rev. B*, vol. 40, pp. 2727–2729, Aug 1989. [Online]. Available: http://link.aps.org/doi/10.1103/PhysRevB.40.2727

[21] A. L. Chernyshev and M. E. Zhitomirsky, “Magnon decay in noncollinear quantum antiferromagnets,” *Phys. Rev. Lett.*, vol. 97, p. 207202, Nov 2006. [Online]. Available: http://link.aps.org/doi/10.1103/PhysRevLett.97.207202

[22] O. A. Starykh, A. V. Chubukov, and A. G. Abanov, “Flat spin-wave dispersion in a triangular antiferromagnet,” *Phys. Rev. B*, vol. 74, p. 180403, Nov 2006. [Online]. Available: http://link.aps.org/doi/10.1103/PhysRevB.74.180403

[23] A. L. Chernyshev and M. E. Zhitomirsky, “Spin waves in a triangular lattice antiferromagnet: Decays, spectrum renormalization, and singularities,” *Phys. Rev. B*, vol. 79, p. 144416, Apr 2009. [Online]. Available: http://link.aps.org/doi/10.1103/PhysRevB.79.144416

[24] M. Mourigal, W. T. Fuhrman, A. L. Chernyshev, and M. E. Zhitomirsky, “Dynamical structure factor of the triangular-lattice antiferromagnet,” *Phys. Rev. B*, vol. 88, p. 094407, Sep 2013. [Online]. Available: http://link.aps.org/doi/10.1103/PhysRevB.88.094407

[25] Y. Shirata, H. Tanaka, A. Matsuo, and K. Kindo, "Experimental realization of a spin-1/2 triangular-lattice Heisenberg antiferromagnet," *Phys. Rev. Lett.*, vol. 108, p. 057205, Jan 2012. [Online]. Available: http://link.aps.org/doi/10.1103/PhysRevLett.108.057205

[26] H. D. Zhou, C. Xu, A. M. Hallas, H. J. Silverstein, C. R. Wiebe, I. Umegaki, J. Q. Yan, T. P. Murphy, J.-H. Park, Y. Qiu, J. R. D. Copley, J. S. Gardner, and Y. Takano, "Successive phase transitions and extended spin-excitation continuum in the $S = \frac{1}{2}$ triangular-lattice antiferromagnet $Ba_3CoSb_2O_9$," *Phys. Rev. Lett.*, vol. 109, p. 267206, Dec 2012. [Online]. Available: http://link.aps.org/doi/10.1103/PhysRevLett.109.267206

[27] M. Poienar, F. Damay, C. Martin, J. Robert, and S. Petit, "Spin dynamics in the geometrically frustrated multiferroic $CuCrO_2$," *Phys. Rev. B*, vol. 81, p. 104411, Mar 2010. [Online]. Available: http://link.aps.org/doi/10.1103/PhysRevB.81.104411

[28] H. J. Lewtas, A. T. Boothroyd, M. Rotter, D. Prabhakaran, H. Müller, M. D. Le, B. Roessli, J. Gavilano, and P. Bourges, "Magnetic excitations in multiferroic $LuMnO_3$ studied by inelastic neutron scattering," *Phys. Rev. B*, vol. 82, p. 184420, Nov 2010. [Online]. Available: http://link.aps.org/doi/10.1103/PhysRevB.82.184420

[29] J. Oh, M. D. Le, J. Jeong, J.-h. Lee, H. Woo, W.-Y. Song, T. G. Perring,

W. J. L. Buyers, S.-W. Cheong, and J.-G. Park, “Magnon breakdown in a two dimensional triangular lattice Heisenberg antiferromagnet of multiferroic $LuMnO_3$,” *Phys. Rev. Lett.*, vol. 111, p. 257202, Dec 2013. [Online]. Available: http://link.aps.org/doi/10.1103/PhysRevLett.111.257202

[30] S. Yamashita, T. Yamamoto, Y. Nakazawa, M. Tamura, and R. Kato, “Gapless spin liquid of an organic triangular compound evidenced by thermodynamic measurements,” *Nature Communications*, vol. 2, p. 275, 2011.

[31] M. Mourigal, W. T. Fuhrman, J. P. Sheckelton, A. Wartelle, J. A. Rodriguez-Rivera, D. L. Abernathy, T. M. McQueen, and C. L. Broholm, “Molecular quantum magnetism in $LiZn_2Mn_3O_8$,” *Phys. Rev. Lett.*, vol. 112, p. 027202, Jan 2014. [Online]. Available: http://link.aps.org/doi/10.1103/PhysRevLett.112.027202

[32] K. Singh, C. Simon, and P. Toledano, “Multiferroicity and magnetoelectric coupling in α-$CaCr_2O_4$,” *Phys. Rev. B*, vol. 84, p. 064129, Aug 2011. [Online]. Available: http://link.aps.org/doi/10.1103/PhysRevB.84.064129

[33] D. Wulferding, K.-Y. Choi, P. Lemmens, A. N. Ponomaryov, J. van Tol, A. N. Islam, S. Toth, and B. Lake, “Softened magnetic excitations in the $S = 3/2$ distorted triangular antiferromagnet α-$CaCr_2O_4$,” *Journal of Physics: Condensed Matter*, vol. 24, no. 43, p. 435604, 2012.

[34] M. Schmidt, Z. Wang, C. Kant, F. Mayr, S. Toth, A. T. M. N. Islam, B. Lake,

V. Tsurkan, A. Loidl, and J. Deisenhofer, “Exciton-magnon transitions in the frustrated chromium antiferromagnets $CuCrO_2$, α-$CaCr_2O_4$, $CdCr_2O_4$, and $ZnCr_2O_4$,” *Phys. Rev. B*, vol. 87, p. 224424, Jun 2013. [Online]. Available: http://link.aps.org/doi/10.1103/PhysRevB.87.224424

[35] V. Hardy, C. Martin, F. Damay, and G. Andr, “Magnetic couplings in the quasi-2D triangular Heisenberg antiferromagnets α-ACr_2O_4 (A = Ca, Sr, Ba),” *Journal of Magnetism and Magnetic Materials*, vol. 330, no. 0, pp. 111 – 118, 2013. [Online]. Available: http://www.sciencedirect.com/science/article/pii/S0304885312008694

[36] C. Kant, J. Deisenhofer, T. Rudolf, F. Mayr, F. Schrettle, A. Loidl, V. Gnezdilov, D. Wulferding, P. Lemmens, and V. Tsurkan, “Optical phonons, spin correlations, and spin-phonon coupling in the frustrated pyrochlore magnets $CdCr_2O_4$ and $ZnCr_2O_4$,” *Phys. Rev. B*, vol. 80, no. 21, p. 214417, Dec 2009.

[37] N. Perkins and W. Brenig, “Raman scattering in a Heisenberg $S = \frac{1}{2}$ antiferromagnet on the triangular lattice,” *Phys. Rev. B*, vol. 77, p. 174412, May 2008. [Online]. Available: http://link.aps.org/doi/10.1103/PhysRevB.77.174412

[38] F. Vernay, T. Devereaux, and M. Gingras, “Raman scattering for triangular lattices spin-1/2 Heisenberg antiferromagnets,” *Journal of Physics: Condensed Matter*, vol. 19, no. 14, p. 145243, 2007.

[39] N. B. Perkins, G.-W. Chern, and W. Brenig, “Raman scattering in a

Heisenberg $S = \frac{1}{2}$ antiferromagnet on the anisotropic triangular lattice," *Phys. Rev. B*, vol. 87, p. 174423, May 2013. [Online]. Available: http://link.aps.org/doi/10.1103/PhysRevB.87.174423

[40] M. G. Cottam and D. J. Lockwood, *Light scattering in magnetic solids.* Wiley New York, 1986.

[41] T. P. Devereaux and R. Hackl, "Inelastic light scattering from correlated electrons," *Rev. Mod. Phys.*, vol. 79, no. 1, p. 175, Jan 2007.

[42] C. Yasuda, S. Todo, K. Hukushima, F. Alet, M. Keller, M. Troyer, and H. Takayama, "Néel temperature of quasi-low-dimensional Heisenberg antiferromagnets," *Phys. Rev. Lett.*, vol. 94, p. 217201, Jun 2005. [Online]. Available: http://link.aps.org/doi/10.1103/PhysRevLett.94.217201

[43] M. Wintel, H. U. Everts, and W. Apel, "Monte Carlo simulation of the Heisenberg antiferromagnet on a triangular lattice: Topological excitations," *Phys. Rev. B*, vol. 52, pp. 13 480–13 486, Nov 1995. [Online]. Available: http://link.aps.org/doi/10.1103/PhysRevB.52.13480

[44] A. Ignatenko, V. Y. Irkhin, and A. Katanin, "The Néel temperature and sublattice magnetization for the stacked triangular-lattice antiferromagnet with a weak interlayer coupling," in *Magnetism and Magnetic Materials*, ser. Solid State Phenomena, vol. 152. Trans Tech Publications, 10 2009, pp. 257–260.

[45] K.-Y. Choi, P. Lemmens, D. Heydhausen, G. Güntherodt, C. Baumann, R. Klingeler, P. Reutler, and B. Büchner, "Anomalous orbital dynamics in $LaSrMnO_4$ observed by Raman spectroscopy," *Phys. Rev. B*, vol. 77, p. 064415, Feb 2008. [Online]. Available: http://link.aps.org/doi/10.1103/PhysRevB.77.064415

[46] E. M. Stoudenmire, S. Trebst, and L. Balents, "Quadrupolar correlations and spin freezing in $S = 1$ triangular lattice antiferromagnets," *Phys. Rev. B*, vol. 79, p. 214436, Jun 2009. [Online]. Available: https://link.aps.org/doi/10.1103/PhysRevB.79.214436

[47] J. Takano and H. Tsunetsugu, "Theory of impurity effects on the spin nematic state," *Journal of the Physical Society of Japan*, vol. 80, no. 9, p. 094707, 2011. [Online]. Available: http://dx.doi.org/10.1143/JPSJ.80.094707

[48] Y. Nambu, R. T. Macaluso, T. Higo, K. Ishida, and S. Nakatsuji, "Structural properties of the two-dimensional triangular antiferromagnet $NiGa_2S_4$," *Phys. Rev. B*, vol. 79, p. 214108, Jun 2009. [Online]. Available: http://link.aps.org/doi/10.1103/PhysRevB.79.214108

[49] P. Giannozzi, S. Baroni, N. Bonini, M. Calandra, R. Car, C. Cavazzoni, D. Ceresoli, G. L. Chiarotti, M. Cococcioni, I. Dabo, A. Dal Corso, S. de Gironcoli, S. Fabris, G. Fratesi, R. Gebauer, U. Gerstmann, C. Gougoussis, A. Kokalj, M. Lazzeri, L. Martin-Samos, N. Marzari,

F. Mauri, R. Mazzarello, S. Paolini, A. Pasquarello, L. Paulatto, C. Sbraccia, S. Scandolo, G. Sclauzero, A. P. Seitsonen, A. Smogunov, P. Umari, and R. M. Wentzcovitch, "QUANTUM ESPRESSO: a modular and open-source software project for quantum simulations of materials," *Journal of Physics: Condensed Matter*, vol. 21, no. 39, p. 395502 (19pp), 2009. [Online]. Available: http://www.quantum-SmB$_6$espresso.org

[50] H. D. Lutz, W. Buchmeier, and H. Siwert, "Phasendiagramm des quasibinren systems NiCr$_2$S$_4$NiGa$_2$S$_4$, kristallstruktur des NiGa$_2$S$_4$," *Zeitschrift fr anorganische und allgemeine Chemie*, vol. 533, no. 2, pp. 118–124, 1986. [Online]. Available: http://dx.doi.org/10.1002/zaac.19865330215

[51] H. Takeya, K. Ishida, K. Kitagawa, Y. Ihara, K. Onuma, Y. Maeno, Y. Nambu, S. Nakatsuji, D. E. MacLaughlin, A. Koda, and R. Kadono, "Spin dynamics and spin freezing behavior in the two-dimensional antiferromagnet NiGa$_2$S$_4$ revealed by Ga-NMR, NQR and μSR measurements," *Phys. Rev. B*, vol. 77, p. 054429, Feb 2008. [Online]. Available: http://link.aps.org/doi/10.1103/PhysRevB.77.054429

[52] Y. Nambu, S. Nakatsuji, Y. Maeno, E. K. Okudzeto, and J. Y. Chan, "Spin dependent impurity effects on the 2D frustrated magnetism of NiGa$_2$S$_4$," *Phys. Rev. Lett.*, vol. 101, p. 207204, Nov 2008. [Online]. Available: https://link.aps.org/doi/10.1103/PhysRevLett.101.207204

[53] K. Watanabe, H. Kawamura, H. Nakano, and T. Sakai, "Quantum spin-liquid

behavior in the spin-1/2 random Heisenberg antiferromagnet on the triangular lattice," *Journal of the Physical Society of Japan*, vol. 83, no. 3, p. 034714, 2014. [Online]. Available: http://dx.doi.org/10.7566/JPSJ.83.034714

[54] M. Dzero, K. Sun, P. Coleman, and V. Galitski, "Theory of topological Kondo insulators," *Phys. Rev. B*, vol. 85, p. 045130, Jan 2012. [Online]. Available: http://link.aps.org/doi/10.1103/PhysRevB.85.045130

[55] V. Alexandrov, M. Dzero, and P. Coleman, "Cubic topological Kondo insulators," *Phys. Rev. Lett.*, vol. 111, p. 226403, Nov 2013. [Online]. Available: http://link.aps.org/doi/10.1103/PhysRevLett.111.226403

[56] R. L. Cohen, M. Eibschütz, and K. W. West, "Electronic and magnetic structure of SmB_6," *Phys. Rev. Lett.*, vol. 24, pp. 383–386, Feb 1970. [Online]. Available: http://link.aps.org/doi/10.1103/PhysRevLett.24.383

[57] Z. Fisk, J. Sarrao, S. Cooper, P. Nyhus, G. Boebinger, A. Passner, and P. Canfield, "Kondo insulators," *Physica B: Condensed Matter*, vol. 223224, pp. 409 – 412, 1996, proceedings of the International Conference on Strongly Correlated Electron Systems. [Online]. Available: http://www.sciencedirect.com/science/article/pii/0921452696001366

[58] S. Wolgast, Ç. Kurdak, K. Sun, J. W. Allen, D.-J. Kim, and Z. Fisk, "Low-temperature surface conduction in the Kondo insulator SmB_6," *Phys.*

Rev. B, vol. 88, p. 180405, Nov 2013. [Online]. Available: http://link.aps.org/doi/10.1103/PhysRevB.88.180405

[59] W. A. Phelan, S. M. Koohpayeh, P. Cottingham, J. W. Freeland, J. C. Leiner, C. L. Broholm, and T. M. McQueen, "Correlation between bulk thermodynamic measurements and the low-temperature-resistance plateau in SmB_6," *Phys. Rev. X*, vol. 4, p. 031012, Jul 2014. [Online]. Available: http://link.aps.org/doi/10.1103/PhysRevX.4.031012

[60] P. Syers, D. Kim, M. S. Fuhrer, and J. Paglione, "Tuning bulk and surface conduction in the proposed topological Kondo insulator SmB_6," *Phys. Rev. Lett.*, vol. 114, p. 096601, Mar 2015. [Online]. Available: http://link.aps.org/doi/10.1103/PhysRevLett.114.096601

[61] Z.-H. Zhu, A. Nicolaou, G. Levy, N. P. Butch, P. Syers, X. F. Wang, J. Paglione, G. A. Sawatzky, I. S. Elfimov, and A. Damascelli, "Polarity-driven surface metallicity in SmB_6," *Phys. Rev. Lett.*, vol. 111, p. 216402, Nov 2013. [Online]. Available: http://link.aps.org/doi/10.1103/PhysRevLett.111.216402

[62] J. Jiang, S. Li, T. Zhang, Z. Sun, F. Chen, Z. Ye, M. Xu, Q. Ge, S. Tan, X. Niu, M. Xia, B. Xie, Y. Li, X. Chen, H. Wen, and D. Feng, "Observation of possible topological in-gap surface states in the Kondo insulator SmB_6 by photoemission," *Nature Communications*, vol. 4, Dec. 2013. [Online]. Available: http://dx.doi.org/10.1038/ncomms4010

[63] G. Travaglini and P. Wachter, “Intermediate-valent $\mathrm{SmB_6}$ and the hybridization model: An optical study,” *Phys. Rev. B*, vol. 29, pp. 893–898, Jan 1984. [Online]. Available: http://link.aps.org/doi/10.1103/PhysRevB.29.893

[64] H. Ohta, R. Tanaka, M. Motokawa, S. Kunii, and T. Kasuya, “Far-infrared transmission spectra of $\mathrm{SmB_6}$,” *Journal of the Physical Society of Japan*, vol. 60, no. 4, pp. 1361–1364, 1991.

[65] T. Nanba, H. Ohta, M. Motokawa, S. Kimura, S. Kunii, and T. Kasuya, “Gap state of $\mathrm{SmB_6}$,” *Physica B: Condensed Matter*, vol. 186188, no. 0, pp. 440 – 443, 1993. [Online]. Available: http://www.sciencedirect.com/science/article/pii/092145269390598Z

[66] B. Gorshunov, N. Sluchanko, A. Volkov, M. Dressel, G. Knebel, A. Loidl, and S. Kunii, “Low-energy electrodynamics of $\mathrm{SmB_6}$,” *Phys. Rev. B*, vol. 59, pp. 1808–1814, Jan 1999. [Online]. Available: http://link.aps.org/doi/10.1103/PhysRevB.59.1808

[67] K. Flachbart, K. Gloos, E. Konovalova, Y. Paderno, M. Reiffers, P. Samuely, and P. Švec, “Energy gap of intermediate-valent $\mathrm{SmB_6}$ studied by point-contact spectroscopy,” *Phys. Rev. B*, vol. 64, p. 085104, Aug 2001. [Online]. Available: http://link.aps.org/doi/10.1103/PhysRevB.64.085104

[68] I. Frankowski and P. Wachter, “Point-contact spectroscopy on $\mathrm{SmB_6}$, TmSe, $\mathrm{LaB_6}$ and LaSe,” *Solid State Communications*, vol. 41, no. 8, pp. 577 –

580, 1982. [Online]. Available: http://www.sciencedirect.com/science/article/pii/0038109882909449

[69] V. N. Antonov, B. N. Harmon, and A. N. Yaresko, "Electronic structure of mixed-valence semiconductors in the $\mathrm{LSDA}+U$ approximation. II. SmB_6 and YbB_{12}," *Phys. Rev. B*, vol. 66, p. 165209, Oct 2002. [Online]. Available: http://link.aps.org/doi/10.1103/PhysRevB.66.165209

[70] F. Lu, J. Zhao, H. Weng, Z. Fang, and X. Dai, "Correlated topological insulators with mixed valence," *Phys. Rev. Lett.*, vol. 110, p. 096401, Feb 2013. [Online]. Available: http://link.aps.org/doi/10.1103/PhysRevLett.110.096401

[71] W. T. Fuhrman, J. Leiner, P. Nikolić, G. E. Granroth, M. B. Stone, M. D. Lumsden, L. DeBeer-Schmitt, P. A. Alekseev, J.-M. Mignot, S. M. Koohpayeh, P. Cottingham, W. A. Phelan, L. Schoop, T. M. McQueen, and C. Broholm, "Interaction driven subgap spin exciton in the Kondo insulator SmB_6," *Phys. Rev. Lett.*, vol. 114, p. 036401, Jan 2015. [Online]. Available: http://link.aps.org/doi/10.1103/PhysRevLett.114.036401

[72] G. Li, Z. Xiang, F. Yu, T. Asaba, B. Lawson, P. Cai, C. Tinsman, A. Berkley, S. Wolgast, Y. S. Eo, D.-J. Kim, C. Kurdak, J. W. Allen, K. Sun, X. H. Chen, Y. Y. Wang, Z. Fisk, and L. Li, "Two-dimensional Fermi surfaces in Kondo insulator SmB_6," *Science*, vol. 346, no. 6214, pp. 1208–1212, 2014. [Online]. Available: http://science.sciencemag.org/content/346/6214/1208

[73] B. S. Tan, Y.-T. Hsu, B. Zeng, M. C. Hatnean, N. Harrison, Z. Zhu, M. Hartstein, M. Kiourlappou, A. Srivastava, M. D. Johannes, T. P. Murphy, J.-H. Park, L. Balicas, G. G. Lonzarich, G. Balakrishnan, and S. E. Sebastian, “Unconventional Fermi surface in an insulating state,” *Science*, vol. 349, no. 6245, pp. 287–290, 2015. [Online]. Available: http://science.sciencemag.org/content/349/6245/287

[74] W. A. Phelan, S. M. Koohpayeh, P. Cottingham, J. C. Leiner, M. D. Lumsden, X. P. Wang, C. Hoffmann, M. A. Siegler, and T. M. McQueen, “On the chemistry and physical properties of flux and floating zone grown SmB_6,” *Scientific Reports*, vol. 6, p. 20860, 2016. [Online]. Available: http://dx.doi.org/10.1038/srep20860

[75] E. Burstein, D. Mills, and R. Wallis, “Interband electronic Raman scattering in semimetals and semiconductors,” *Physical Review B*, vol. 4, no. 8, p. 2429, 1971.

[76] P. Nyhus, S. L. Cooper, Z. Fisk, and J. Sarrao, “Light scattering from gap excitations and bound states in SmB_6,” *Phys. Rev. B*, vol. 52, pp. R14 308–R14 311, Nov 1995. [Online]. Available: http://link.aps.org/doi/10.1103/PhysRevB.52.R14308

[77] ——, “Low-energy excitations of the correlation-gap insulator SmB_6: A light-scattering study,” *Phys. Rev. B*, vol. 55, pp. 12 488–12 496, May 1997. [Online]. Available: http://link.aps.org/doi/10.1103/PhysRevB.55.12488

[78] T. Kasuya, K. Kojima, and M. Kasaya, "Theory and experiment on SmB_6," in *Valence Instabilities and Related Narrow-Band Phenomena.* Springer, 1977, pp. 137–152.

[79] I. Morke, V. Dvorak, and P. Wachter, "Raman scattering in intermediate valent SmB_6," *Solid State Communications*, vol. 40, no. 4, pp. 331 – 334, 1981. [Online]. Available: http://www.sciencedirect.com/science/article/pii/0038109881908310

[80] N. Ogita, S. Nagai, M. Udagawa, F. Iga, M. Sera, T. Oguchi, J. Akimitsu, and S. Kunii, "Raman scattering study of rare-earth hexaboride," *Physica B: Condensed Matter*, vol. 359361, no. 0, pp. 941 – 943, 2005. [Online]. Available: http://www.sciencedirect.com/science/article/pii/S0921452605002978

[81] R. Shuker and R. W. Gammon, "Raman-scattering selection-rule breaking and the density of states in amorphous materials," *Phys. Rev. Lett.*, vol. 25, pp. 222–225, Jul 1970. [Online]. Available: http://link.aps.org/doi/10.1103/PhysRevLett.25.222

[82] P. A. Alekseev, "High borides: determining the features and details of lattice dynamics from neutron spectroscopy," *Physics-Uspekhi*, vol. 58, no. 4, 2015.

[83] M. Cardona and G. Guntherodt, *Light Scattering in Solids II: Basic Concepts and Instrumentation.* Springer-Verlag, 1982.

[84] P. Lemmens, A. Hoffmann, A. Mishchenko, M. Talantov, and G. Gntherodt,

"Raman scattering of extra vibrational modes in mixed-valence compounds," *Physica B: Condensed Matter*, vol. 206207, no. 0, pp. 371 – 373, 1995. [Online]. Available: http://www.sciencedirect.com/science/article/pii/0921452694004625

[85] M. V. Klein, "Theory of two-phonon Raman scattering in transition metals and compounds," *Phys. Rev. B*, vol. 24, pp. 4208–4223, Oct 1981. [Online]. Available: https://link.aps.org/doi/10.1103/PhysRevB.24.4208

[86] H. Wipf, M. V. Klein, and W. S. Williams, "Vacancy-induced and two-phonon Raman scattering in ZrC_x, NbC_x, HfC_x, and TaC_x," *physica status solidi (b)*, vol. 108, no. 2, pp. 489–500, 1981. [Online]. Available: http://dx.doi.org/10.1002/pssb.2221080225

[87] M. V. Klein, J. A. Holy, and W. S. Williams, "Raman scattering induced by carbon vacancies in TiC_x," *Phys. Rev. B*, vol. 17, pp. 1546–1556, Feb 1978. [Online]. Available: https://link.aps.org/doi/10.1103/PhysRevB.17.1546

[88] J. K. Freericks, T. P. Devereaux, M. Moraghebi, and S. L. Cooper, "Optical sum rules that relate to the potential energy of strongly correlated systems," *Phys. Rev. Lett.*, vol. 94, p. 216401, Jun 2005. [Online]. Available: http://link.aps.org/doi/10.1103/PhysRevLett.94.216401

[89] J. Freericks and T. Devereaux, "Raman scattering through a metal-insulator transition," *Physical Review B*, vol. 64, no. 12, p. 125110, 2001.

[90] W. T. Fuhrman and P. Nikolić, “In-gap collective mode spectrum of the topological Kondo insulator SmB_6,” *Phys. Rev. B*, vol. 90, p. 195144, Nov 2014. [Online]. Available: http://link.aps.org/doi/10.1103/PhysRevB.90.195144

[91] P. Thalmeier and P. Fulde, “Bound state between a crystal-field excitation and a phonon in $CeAl_2$,” *Phys. Rev. Lett.*, vol. 49, pp. 1588–1591, Nov 1982. [Online]. Available: http://link.aps.org/doi/10.1103/PhysRevLett.49.1588

[92] M. E. Valentine, S. Koohpayeh, W. A. Phelan, T. M. McQueen, P. F. S. Rosa, Z. Fisk, and N. Drichko, “Breakdown of the Kondo insulating state in SmB_6 by introducing Sm vacancies,” *Phys. Rev. B*, vol. 94, p. 075102, Aug 2016. [Online]. Available: https://link.aps.org/doi/10.1103/PhysRevB.94.075102

Vita

Michael Valentine was born in Baltimore, MD on April 23, 1989. He graduated from Fallston High School in 2007. He attended University of Maryland, College Park from 2007 to 2011 where he received a B.S. degrees in Mechanical Engineering and Physics, graduating cum laude. He enrolled in the Ph.D. program as a part of the Department of Physics and Astronomy at Johns Hopkins University in 2011. His thesis work focused on exploring sensitive states that arise in strongly-correlated electron systems through the use of inelastic light scattering.